POLITECNICO DI MILANO
DEPARTMENT of PHYSICS
DOCTORAL PROGRAMME IN CYCLE XXIV

Elucidating the Role of Interfaces and Interfacial Layers in Mixed Halide Perovskite Devices

Doctoral Dissertation of:
Vijay Venugopalan

Supervisor:
Dr. Annamaria Petrozza

Tutor:
Prof. Guglielmo Lanzani

The Chair of the Doctoral Program:
Prof. Paola Taroni

Year : 2013 – Cycle : XXIX

To my Father

My Mother

My Brother

DECLARATION

I hereby declare that except where specific reference is made to the work of others, the contents of this dissertation are original and have not been submitted in whole or in part for consideration for any other degree or qualification in this, or any other university. This dissertation is my own work and contains nothing which is the outcome of work done in collaboration with others, except as specified in the text and Acknowledgements.

Vijay Venugopalan

February 2017

Abstract

OHPs have shown great promise of providing a pronounced impact for energy harvesting and opto-electronic device applications. Since device operation causes ion migration within the Perovskite semiconductor, interfacial defect states may play a more significant role in these semiconductors than their counterparts. The migrating ions are anticipated to accumulate at the semi-conductor interfaces which may then increase the density of interface states.. Many strategies can be applied to mitigate these effects. Here the possibility of applying an interfacial layer that interacts with the accumulated ions to mitigate the effects is shown as a promising approach. This approach is also used to make highly efficient Photodetectors. Interfaces are also modified with other techniques so as to enhance the performance.

Acknowledgements

First of all, I present my extreme gratitude to my supervisor, Dr. Annamaria Petrozza for giving me a rare and exceptional opportunity to work under her supervision. Her support was what kept me going at the hardest of times and helped me settle in a new lab and a new land. Her guidance and encouragement towards identifying the goals for my doctoral project inspired to me think clearly and critically to achieve tangible goals. Anna directed me to truly interesting research projects while simultaneously giving me space to attempt and discover new avenues and insights in scientific research. In her guidance research was always dynamic and filled with many interesting and varied possibilities.

I extend my heartfelt thanks and love to my tutor Prof. Guglielmo Lanzani who was the 'Godfather' and solved all issues, scientific and non-scientific. A jolly-man always smiling and excited, the fun he brings is contagious. His support and mentoring during my stay at IIT-CNST is absolutely amazing.

I am very grateful to my funding body, the EU Marie-Curie Network DESTINY, for making all of this possible. A special mention to Prof. Alison Walker who did a marvellous job of personal mentoring each one of us and practically made all the documentation a cake-walk for the fellows. My heartfelt thanks to all the Members of DESTINY - Marie Curie Initial Training Network for the wonderful time and friendships that I will cherish beyond my PhD. Many will be in science and it will be great to keep the fire of DESTINY going.

I would also like to thank Dr. Mario Caironi for insightful suggestions and a thorough scientific discussion on the Photo-Detector work which are presented here. I would like to thank Prof. Giorgio Ferarri from Politecnico who introduced me to the world of Noise.! His personal touch and the time he spent in training and discussing the problems with me is heart-warming and a pleasant surprise.

All the members of the Petrozza group, both past and present have been of a great deal of help academically. Helpful critical discussions and insights of Post-Docs saved a lot of my time in not venturing into impossible projects. In particular, thanks to Dr. Francesco Lamberti, Peter Topolovsek and Jeroen who were valuable as collaborators and great friends, the first of international scientific colleagues. Francesco of course helped with learning and training me with Impedance. Peter was the Brother-in-Arms during optimization of recipes to get champion solar cells. The discussions we had has bore fruit into into the two projects done here in this

thesis. Jeroen, a DESTINY mate had a great time in scientific discussions and the passivation project. Dr. Chen Tao provided great devices for my Impedance studies which form the core of this thesis and I am highly obliged and thank him for his great contribution. Dr. James Ball was a great doubt-solver and was of great help during my period there. Roberto also for collaborating in the Photodetector project. I would like to thank Dr.AKS Kandada for helping me settle in a new lab, a new country and showing me the various sides of research. Would like to thank the other lab-mates present and past for their invaluable support.

I wish to thank Prof Prof. Juan Bisquert Of Universitat Jaume I de Castellón and Prof Henry Snaith , University of Oxford for making me feel so welcome in their group during my secondments and for their invaluable contribution to the my PhD project. Their guidance and support in performing the marathon experiments during the secondment. Dr. Antonio and Dr.Eva in Spain and Alba at Oxford made this possible and were the perfect hosts.

I would also like to acknowledge Stefano, Luca and Enrico who made all the technical stuff run smoothly so that our work never got stuck. So much so for Tessa, Silvia and Alessandra without whom getting the documentation done at Italy would require me undergo a separate Masters degree.! The technical and Admin staff are clearly the backbone of my stay in Italy and easily of most CNST professionals.

I certainly would not be at this point in my education without many teachers and mentors who helped me along the way. Some of the most influential were Hari Sir, who created the initial spark in me to pursue physics. Other teachers in Masters and Bachelors were also of great pushers who pushed me to pursue a doctoral degree. Dr. Talwar, Dr. Muthurajan, Dr. AV Limaye, Dr. Banpurkar, all of them have been the support both technically and personally, without whom I wouldn't be where I am.

During the course of my PhD I have received support from a host of friends outside of CNST. In particular, Ranbir Singh, Mong, Prashant, Amol, Vibhav, Lohith, Sanathana, Aditya, Shahab, Nikhil, Uzma, Abhay, whose presence certainly made my time in graduate school more entertaining and provided help and support in and beyond the scope of my research. I would also like to thank Manoj Kumar uncle and Anita aunty for making festivals away from home so joyous and for giving me space in their heart and home.

Another important step in my PhD has been the foundation of VIGYANshaala – Communicate and Inspire, which introduced me to a whole new dimension of science communication and teaching. I am very thankful to the MRS foundation for their grassroots grant award. I also

thank whole of team VIGYANshaala – Aditya, Shruti, Darshana, Shivani, Himadri, Anuj, Nimisha and Shilpi for their wonderful friendship and pulling through a fabulous series of "It's a MATERIALS World" workshops in 10 different cities in India.

Finally, it is with great appreciation that I thank my family for considering my endeavors to be worthwhile. Thank you to my brother and sister-in law, Vivek Venugopalan and Mamatha Narayanan, for providing much needed breaks and being interested in my research and bringing my bundle of joy Aashvi into my life. Thanks to Vivek for sharing my love for Arsenal. My mother Chitra and father, Sethu Venugopalan, made science a normal thing to play with as a child and gave us all the opportunities to go out in the open and explore. Even though my mother is not with me today – I recall her at aevery ste in my journey. The love she gave in the firt few years of my life is enough t last a lifetime. My father strongly influenced my decision to apply to and ultimately pursue graduate studies in Physics. He has shared big dreams with me, helped me understand my work and myself, advised me on professional and scientific questions, and been an inspiration, mentor and friend throughout. He maintained confidence that I would complete my research even when I had my doubts. Throughout my academic journey, support from my father has helped me relax and have fun outside of lab. I fall short of words to present my gratitude to my father and dedicate this thesis to his perseverance and confidence in me. Although I've thanked many people here, and there are many more I would like to thank for contributions to my personal and scientific growth, the person with whom I communicated the most during the period of my PhD is my new-wife, Darshana. I thank her for always being there and for her unconditional support at each step. It can be easily said after my father if there was anyone who had the confidence in me, the love for my thesis like I have then It was her. Her unconditional support cannot be put in words and I am forever grateful to have stepped into her life. Her joy and enthusiasm which trickles into my life is what I am looking forward to.

Table of Contents

1 Introduction

We live in an era of uncertainty. 2016 was the warmest year since book keeping started in 1880[1]. The effects of global warming on earth are unmissable: Polar ice sheets are shrinking at unprecedented rates, glaciers and snow cover are retreating globally and oceans are much more acidic and warmer with sea levels rising at alarming rates.

Insurmountable evidence points to the causes for global warming to the human intervention[1]. It has increasingly become clear that greenhouse gases, especially CO_2 is the major cause for this increase. To give perspective, the CO_2 levels for half a million years is shown below. The sharp increase in CO_2 coincides with the start of the industrial revolution and fossil fuel consumption.

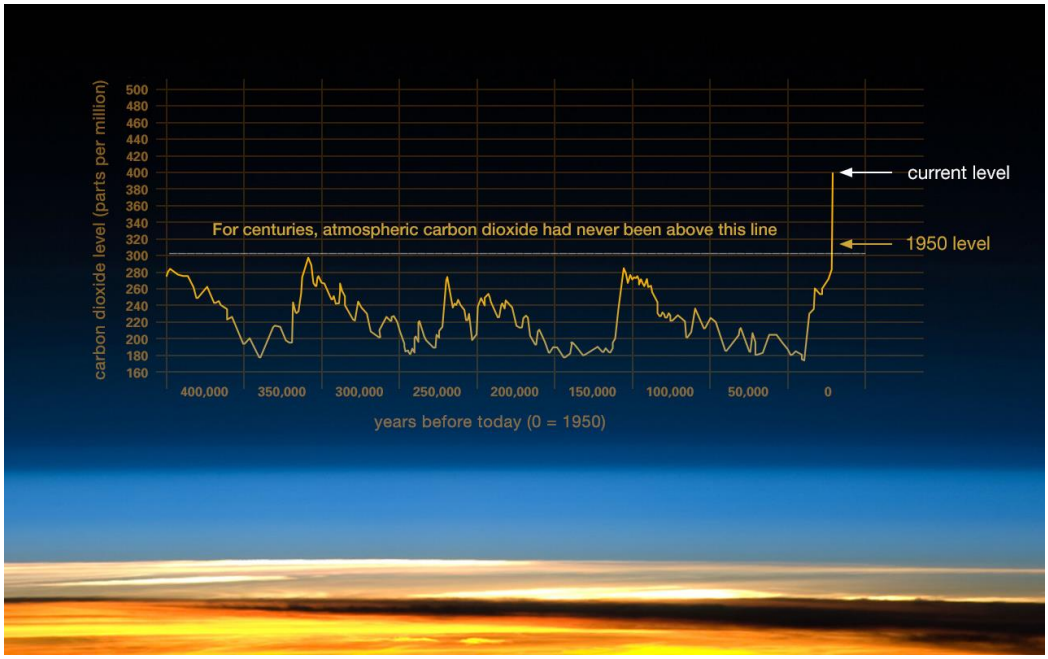

Figure 1-1 Global Climate Change: Evidence. (2008, June 15) from http://climate.nasa.gov/evidence/

Sources of today's energy needs come mostly from fossilized fuels such as natural gas or coal which emit CO_2. Hence most mechanized, electrical and electronic machinery on the planet add to CO_2 emission. A sustainable alternative to fossilized fuels are from renewable and green sources of energy. Solar Energy is one of the most promising 'Green Tech' that can act as a replacement, provide a sustainable source and have a 0% working emission of CO_2.

In retrospect, Nature's ways reveal solar energy to be an ideal source of energy for sustenance of life.

Semiconductor Photovoltaics (PV) are the most efficient solar energy harnessing devices on the planet. Record efficiency solar cells (Multi-junction Solar Cells with Concentrators: η~ 30%-45%) however face critical challenges (for example high costs) to make them viable. On the other hand the PV market is dominated by Single Crystalline Silicon (Best Cell η~26% with Best Module η~24%) and Poly-Crystalline Silicon (Best Cell η~22% with Best Module η~19.5%) based photovoltaics which have a lion's share of more than 90% of the total market[2]. This is primarily due to the falling prices of these solar modules over time Figure 1-2. The drop in the prices has led Silicon PV to be cheaper than grid-based electricity in many countries[2] thereby stirring large interest in this 'Green' technology. Interestingly, there are a few technological avenues that can still be leveraged to make a larger impact on this multi-billion dollar industry. In this thesis, a novel family of semi-conductor Organic Halide Perovskites (OHP) is explored in detail, which has recently shown great promise to boost this industry.

OHPs are direct bandgap crystalline semi-conductors which can be solution processed and are compatible with Roll-to-Roll (R2R) printing[3,4]. Solution processed OHPs have already climbed from 10% to record efficiencies of 21% in a time-scale of 6 years which is an unprecedented growth rate[5–8]. Since their individual components of OHP are commonly available cheap chemicals and they are R2R compatible as well as they do not require high fabrication

temperatures (like with Si), they promise to be an ideal and cheap replacement for Si. Another leverage the OHPs provide technologically are with tandem solar cells. Tandem cells (multi-junction solar cells) produced by fabricating OHP cells on top of commercial Si solar cells are expected to provide a still higher efficiency. This directly taps into and boosts up the present billion dollar industry[5].

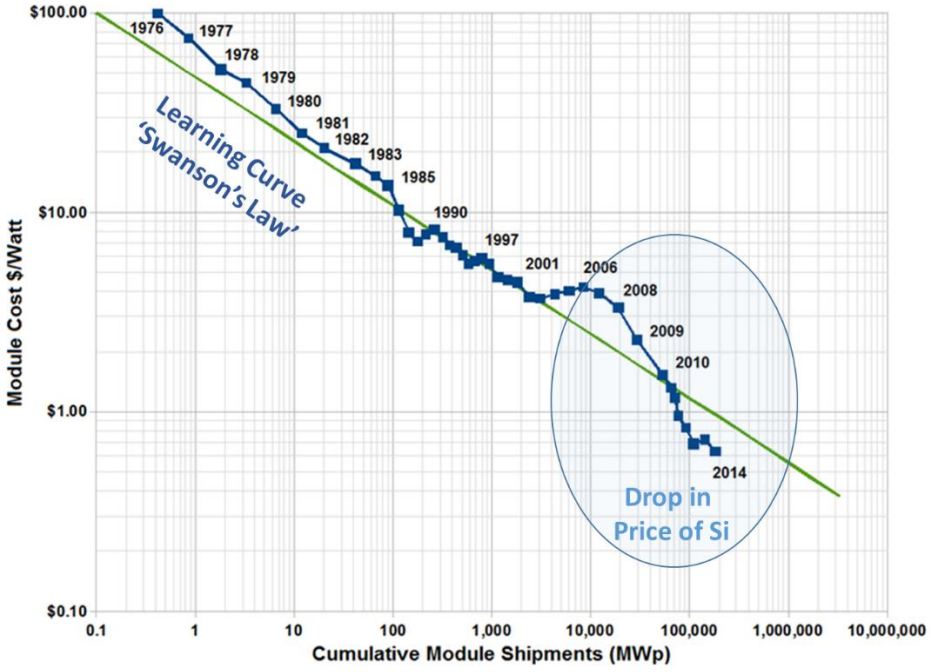

Figure 1-2 : Learning Curve Analysis for Silicon PV. From 2006 a massive drop in prices is observed, not following the law due to a large drop in the prices of raw silicon wafers. From https://en.Wikipedia.org/wiki/Swanson's_law

However as in any new technology, there are a few challenges that need to be addressed with OHPs. The most critical amongst them is the stability of the solar cells themselves[9]. OHPs are notoriously unstable due to a few failure mechanism that are poorly understood as of now. One aspect of stability that is proving to be critical for OHPs are that of interfaces in these solar cells, especially at the surface of the Perovskite semiconductor. Hence most of this thesis is focussed on investigating the role of interfaces on the stability of the OHP devices.

$MAPbI_3$ ($MAPbI_3$: Methyl Ammonium Lead Iodide) is a 'soft' ionic crystal. This leads to motion of the ions of the crystal, within the crystal (both microscopic and macroscopic). This ionic motion is due to an applied electric field or due to the built-in field in the devices. Macroscopic motion of ions (especially that of the loosely bound Iodide ions I^-) occurs over many micrometres which is larger than the total device thickness[10]. Then this macroscopic ionic motion is bound to cause an accumulation of these ions at one of the interfaces. This accumulation is due to the slow drift-diffusion dynamics of ions within the crystal, which may change the working stability of the devices over time. In this thesis, we explore this interfacial stability of OHPs in the light of accumulation of ions and demonstrate possible solutions to overcome them.

In Chapter 2, the materials used for device preparation and device making recipes are presented. The opto-electrical techniques and their introduction are also presented.

In Chapter 3, the stability of two known types of interfaces are probed: $MAPbI_3$-TiO_2 and $MAPbI_3$-PCBM (TiO_2-Titanium Dioxide and PCBM: phenyl-C61-butyric acid methyl ester are electron acceptors and efficient hole blockers). For these identical devices differing only by interfaces are prepared. Evidence of large electronic charge accumulation, accumulation of electronic trap states and slow response times (RC-time constants) are found only in devices with a TiO_2 interface. Trapped electronic charges at the interface from the injected dark current are postulated to lead to the giant dark capacitances in Perovskite solar cells. Small Perturbation Impedance Measurements and Transient Photo-current and Photo-voltage transient measurements are performed for probing the devices.

In Chapter 4, an attempt is made to answer the basic question: How does the presence of a thin layer of PCBM at the interface suppress the formation of interfacial charge accumulation, passivate trap formation and reduce the giant capacitance observed in devices? It is known that

ions migrate within the Perovskite devices, which then would accumulate at the Perovskite interface. Hence the possibility of PCBM reacting with the accumulated ions is investigated. It is found that accumulated I^- ions dope PCBM (n-type) in solid state. This changes the chemical state, work-function and the electrical properties of the e^- extraction layer of PCBM. The formation of defect levels at the Perovskite Semiconductor surface is then discussed due to the accumulated I^-. Devices with accumulated I^- at the interface can create interstitial defect states creating trapped holes that recombine non-radiatively. These defect states decrease the working stability of the solar cells. Applying an interfacial layer like PCBM which actively reacts with the accumulated ions greatly enhances the device stability.

In Chapter 5, Photoconductors (PCs) based on Printed Perovskite Particles (PPP) is presented. Submicron sized perovskite particles are screen printed on Au electrodes to give a simple Metal-Semiconductor-Metal (MSM) configuration. Learning from the previous chapter, PCBM is added to the PPP PCs, significantly enhancing the performance. The PCs show performance comparable to Si-Photodiodes and are comparable to values reported in literature of perovskite Photodetectors (PDs). The PPP have been well characterized. The enhancement from the addition of PCBM is attributed to (1) Passivation of interfacial traps of PPP by PCBM and (2) Draining the PPP of electrons (PCBM accepts the photogenerated electrons leaving behind the photogenerated holes) and selectively circulating the holes in the PPP which provides a large gain in the PCs. A detailed investigation on the working mechanism of Perovskite PCs is presented.

In Chapter 6, two other works related to the interfacial kinetics of perovskite devices is presented. In the First Section: Layered Materials of WS_2 (Tungsten Di Sulphide) is presented as an alternative Hole Transport Layer (HTL) for the commonly used Spiro-OMeTAD (2,2',7,7'-Tetrakis-(N,N-di-4-methoxyphenylamino)-9,9'-spirobifluorene) for Perovskite PDs. Inorganic layered WS_2 HTLs are much cheaper, more stable and can be processed in air in

comparison to very expensive, air-sensitive and unstable organic HTLs. Applying a WS_2 HTL also suppresses the noise within the PDs enhancing the performance of the PDs. In the Second Section: Defect passivation of uncoordinated Pb sites on the Perovskite surface is achieved using organic molecules that bind to these defect sites. These passivants molecules reduce the hysteresis of the solar cells and have also shown promise for increasing the efficiency of the solar cells.

In Chapter 7, the conclusions on the critical role of interfaces are summarized. Interfacial energetics in Perovskites are much more critical in comparison to other semi-conductors due to the added complexity of accumulating ions and vacancies at the perovskite surface. The accumulated ions and vacancy defects may prove to be the Achilles's heel for these devices. Finally, a new technique of measurement (Transient Photocurrent-Open Circuit Voltage) developed in this PhD is presented. This measurement technique is very relevant to semiconductors with migrating ions like in perovskites and has the potential to give deeper insights into the working of these solar cells.

2 Materials and Methods

2.1 Materials and Devices:

For the source of all chemicals : Lead Iodide is sourced from Alfa Aesar (99.99% Pure). Spiro-OMeTAD (2,2',7,7'-Tetrakis-(N,N-di-4-methoxyphenylamino)-9,9'-spirobifluorene), Organic salts are from Dyesol.

Synthesis of Methyl Ammonium Precursors:

100 mL of absolute ethanol was used to dilute 24 mL of methylamine solution (33% in ethanol) in a 250 mL round bottom flask, followed by addition of 10 mL aqueous solution of hydriodic acid (57 wt HI) under constant stirring. After a reaction time of 1 hour with continuous stirring at room temperature, a rotary evaporator was used to remove the solvents from the dissolved reacted mixture. A white solid residual was obtained. This was then washed with dry diethyl ether one time/two times and then recrystallized from ethanol to get methylammonium iodide crystals (CH_3NH_3I). The powder looks whitish crystalline and has some trace amounts of Hypo-Phosphorous Acid (HPA) and HI which results in giving higher device efficiencies

Device Making and Testing:

1. **2 Step Partially Evaporated perovskites :**

   Substrate patterning/cleaning of FTO is undertaken: With Zn powder and 2M HCl for etching. Cleaning by sonicating the substrates with Detergent Alconox, DI Water,

Acetone, IPA in sequence. A hole-blocking & electron conducting compact planar layer of TiO_2 (50nm) is fabricated by spinning the precursor solution at 2000RPM (370µL Titanium Iso-Propoxide in 2.53ml IPA added dropwise to a solution of 35µL in 2.5ml IPA). 10mg/ml 60-PCBM (phenyl-C61-butyric acid methyl ester) is spin coated on TiO_2 for 30s at 4000RM. PbI_2 is evaporated in a standard evaporator chamber at 0.1A/sec upto 120-140nm in thickness. An MAI solution of 44mg/ml is spun on top of the PbI_2 at 2000RPM and is annealed at 100^{o}C for 60minutes for a complete reaction to occur between the PbI_2 and MAI. The resultant $MAPbI_3$ perovskite is spun with a solution of IPA to remove the unreacted MAI on the perovskite film. The HTL Spiro-OMeTAD doped with Li-TFSi and tBP are spun on top at 4000ROM as per (ref). Finally Au electrodes are coated on top.

2. **2-Step Spin Coated perovskites :**

   All the layers but the Perovskite fabrication differ. The PbI_2 is spin coated at 3000RPM (1M in DMSO) with the substrate/soln. both at Room Temperature and subsequently annealed at 120^{0}C. 20mg/ml MAI solution is spun at 2000RPM to obtain a Perovskite conversion. In all cases the spin coated substrates are allowed to dry before annealing.

3. **Lead Acetate Devices (PbAc) :**

   All the layers remain similar but the Perovskite Fabrication. For devices and few samples (Kelvin Probe) the PbAc formulation is used where PbAc:MAI is taken in a 40% by weight in a DMF solution. 2.5% additive of HPA is added. Films are spun at 2000RPM and are dried before annealing at 100^{0}C for 30minutes.

4. **Mixed Cation Mixed Halide Devices : ($Cs_{0.175}FA_{0.825}PbBr_{0.3}I_{0.7}$)**

   All layers remain similar but the Perovskite Layer and the HTL layer described in Chapter 6. PCBM-60 is spun on top of the TiO_2 layer. $Cs_{0.175}FA_{0.825}PbBr_{0.6}I_{2.4}$ solution was prepared by mixing $CsPbI_3$, $FAPbI_3$ and $FAPbBr_2I$ in a 0.175:0.525:0.3 volume

ratio. The perovskite film was formed by orthogonal solvent quenching technique (toluene) and annealed at the temperature 170 °C for 10 min.

Solar Cell Testing and Stability Measurements:

Solar Cells are measured with a standard Keithley 2400 Sourcemeter and an AM1.5 calibrated light source with 1 Sun. The Solar Cell Efficiency (η) is measured by performing an J-V sweep of the solar cell under 1 Sun (*Figure 2-1*). The Maximum efficiency of the cell is obtained at the Maximum Power Point (MPP). The Open circuit voltage and the short circuit current indicate the maximum voltage/current deliverable by the cell and are important parameters. The efficiency of the solar cells is given by :

$$\eta = \frac{J_{SC} \times V_{OC} \times FF}{(Power_{input})}$$

where J_{sc} V_{OC} & FF are the Short Circuit Current, Open Circuit Voltage and Fill Factor respectively (ref).

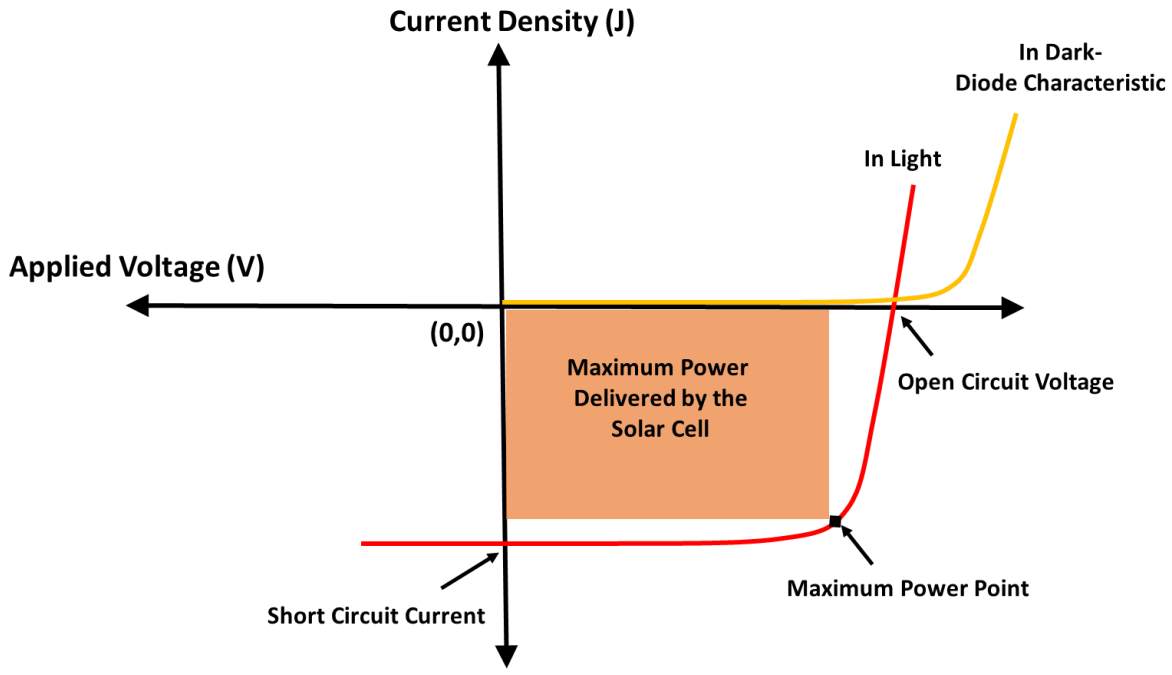

Figure 2-1 : J-V curve of a solar cell photodiode in light and dark. Showing the various parameters extracted from the Solar Cell Curve.

2.2 Transient Opto-electronic Studies:

1. TRANSIENT PHOTOCURRENT (TPI) / PHOTOVOLTAGE (TPV)

Transient Photocurent and Photovoltage measurements have been very useful to obtain charge transport and charge recombination lifetimes in Dye Sensitized Solar Cells and Organic Solar Cells[11–15]. For complete details the reader is referred to the references[11,13,16,17]. In brief a background white light source (7 Luxeon LXML-PWC2- With an AM1.5 Filter - 0.01 Sun to 4 Suns) is incident on the device. Another Perturbation Light Source (Green 532nm LED) is pulsed in the background on top of it. The experimental scheme is shown in Figure 2-2. The response of the solar cells to the perturbation pulse is recorded. The cell is held at Open Circuit (Transient Photo-voltage) or at Short Circuit (Transient Photo-current).

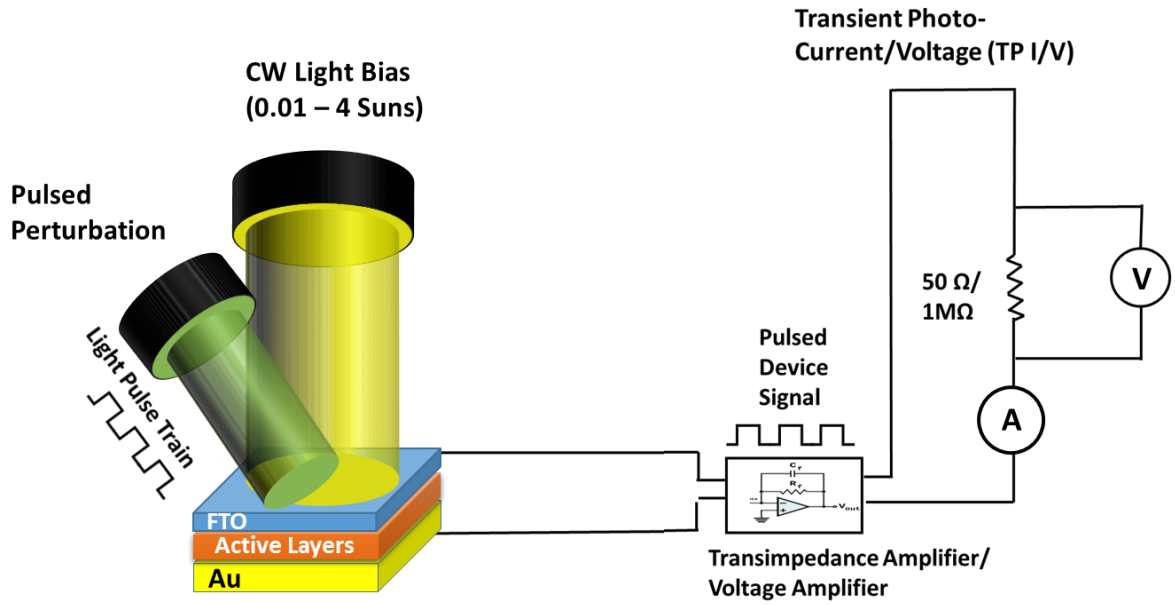

Figure 2-2 Experimental Setup Developed during the PhD for Transient Photocurret / Transient Photovoltage measurements. The same setup is used for Open Circuit Voltage Decays (OCVD) and Smal Signal Impedance Spectroscopy

The transient photocurrents give the transport time of charges at short-circuit (τ_T), while the transient photovoltages give the recombination lifetimes of the charges at Open-Circuit (τ_T). Changing the background light intensity Transport/Recombination lifetimes are expected to

change with the changing intensity of the background light (ref). From this charge density and differential capacitances in the devices are extracted[18,19]. Finally, the transient lifetimes are recorded every 10 seconds through a 2-GHz Oscilloscope with the background white light being always incident. Hence a Lifetime ((τ_T)µsec) Vs Time (**t** sec) plot is obtained where a dynamic change is transport and recombination lifetimes can be seen. This is important in the case to check the stability of the solar cells at different light intensities.

The perturbation pulses produce an increased charge density Δn on top of the background charge density n. From the transport/recombination decays of the Δn, the differential capacitance at a given given background intensity is given by

$$dC(V_{OC}) = \frac{\Delta q}{\Delta(V_O)(V_{OC})}$$

Where Δq is the collected charges from TPI, ΔV_0 is the pea of the TPV and dC is the differential capacitance created by the perturbation pulse – All of these parameters are at a given voltage in the cell created by the intensity of the background light. Integrating the capacitance ($dC(V_{oc})$) over different background intensities (V_{oc}) gives us the total charge density in the devices.

2. OPEN CIRCUIT VOLTAGE DECAYS (OCVD)

The same setup is used also for OCVD measurements. In the OCVD measurements, a background white light source (7 Luxeon LXML-PWC2) is modulated from 0.01 to 2 Suns while the cell is kept at V_{oc}. The light is switched off and the decays in the Voltage within the cell is measured from 100ns – 100secs. The acquisition is automated by the Oscilloscope/Signal Generator delay times.

2.3 Impedance Spectroscopy:

The impedance is the measurement of small perturbation voltage (V) to current (I) Ratio:

$$Z(\omega) = \frac{\hat{V}(\omega)}{\hat{I}(\omega)}$$

ω is the angular frequency and is equal to 2πf where f is the frequency of the applied voltage signal. For Ohmic processes only Z=R, where the Impedance is real and positive. The presence of relaxation processes produces a capacitive/inductive behaviour in the devices which leads to Z(ω) being a complex. The complex capacitance and dielectric constants are given by[20–23]:

$$C(\omega) = \frac{1}{i\omega Z(\omega)}$$

$$\varepsilon(\omega) = \frac{dC(\omega)}{A\varepsilon_0}$$

The relation between the real and complex dielectric values are given by the standard Kronig-Kramer relation (ref). A solar cell consists of multiple interfaces and bulk-active layers which then as one unit give rise to multiple relaxation processes at various frequencies. Hence Impedance Spectroscopy is a powerful technique to separately observe each independent processes in the solar cells.

2.4 Photoconductor-Photodetector Measurements:

The responsivities are measured by a standard spectrophotometer (A Tungsten-Halogen Lamp with a Mono-chromator) coupled to Keithley 2300 Sourcemeter. The reference light is calibrated by a Silicon Photodioide (UV-818) and the Photodetector measurements are performed with an IV-Sweep at every wavelength. The sweep is at steps of 100mV-200mV with a delay time of 1sec.

The noise measurements are done with two Op-Amp configurations with a Cross-Correlation technique that reduces the minimum detectable noise. The setup is an in-house setup details of which can be seen here[24].

The transient response is performed with standard LED's (Blue/Green/Red) using the Transient Photocurent/Voltage setup. The values are normalized to the starting of the transient to obtain comparison of the lifetimes.

The Intensity Vs Photocurrent measurements are performed with a HeNe laser (543nm Spot Diameter ~ 1mm) chopped at 1Khz and the photocurrent measured through a lockin-amplifier. The current is collected through a Current TransImpedance-Amplifier (DLPCA) that is also used to bias the solar cell. The intensity is varied with intensity filters.

2.5 Other Measurements:

1. RAMAN MEASUREMENTS

Raman Measurements are performed with a Renishaw Micro-Raman Microscope from 10X-100X magnifications lenses used for focussing. A 532nm Green laser is used as an excitation source and light is collected in a back-scattering configuration with a notch filter-monochromator- CCD setup. The excitation power source used s from 100µW – 10mW with an averaging of at least 50 samples.

2. KELVIN PROBE MEASUREMENTS

Kelvin Probe Measurements (By commercial KP Technologies) with a vibrating Gold-Tip (2mm diameter). The samples are grounded and surface potential measurements are let to stabilize after which the values are recorded.

3 Interfacial Electronic Charge Accumulation & Trapped Charges in $MAPbI_3$ Solar Cells

3.1 Introduction

The motion of ionic charges is thought to be the underlying cause for the hysteresis and the slow changing opto-electronic properties in mixed halide perovskites[25–27]. However few have recently suggested that an ionic motion by itself cannot explain the large hysteresis observed under working conditions and it also requires the formulation of trapped electronic charges[1528]. Also, the large capacitances observed in these photovoltaic cells which affect the aforementioned slow dynamics cannot be reconciled with purely a build-up of ions at the interface[29–32]. An ionic build-up at the interface causing a Helmholtz (double layer capacitance) capacitance would not lead to values beyond 1-10µF/cm^2 , however we find two or three orders of magnitude higher capacitances (1-10mF/cm^2) indicating this is not due to a Helmholtz capacitance from accumulating ions. Also thickness independence of the observed giant capacitances suggests this not to be due to the Helmholtz capacitance from accumulated ions[32]. Alternatively, it has been recently suggested that large capacitances can be attributed to the polarization of the perovskite interfaces by formation of electronic charge accumulation zones, which may indicate this to be an indirect effect of the ions at the interface[33]. The dependence of the time-dependent slow varying opto-electronic properties such as hysteresis and slow changing PL on the formation of large capacitances remains implicit[9,34–36]. It has been known

for a long time that the surface and interface properties of a crystalline semi-conductors (like Si) can drastically change its performance in devices. Considering our case of a crystalline OHP semi-conductor which also comprises the prospect of migrating ions to its surface, it is reasonable to expect the surface/interface of the semiconductor to dictate many features peculiar to these class of photovoltaic cells.

In this chapter we probe the interfacial transport layers contacting the perovskite solar cells and demonstrate the importance of careful interfacial engineering. We henceforth refer to these interfacial layers which are charge selective buffer layers either for electrons or holes as 'contacts to the perovskite'. We use the widely employed standard structure of FTO/c-TiO_2/perovskite/ SpiroOMeTAD /Au as a starting point for our study where c-TiO_2 is a compact ~50nm layer of Titianium-dioxide electron transport/hole blocking layer and SpiroOMeTAD (2,2',7,7'-Tetrakis-(N,N-di-4-methoxyphenylamino)-9,9'-spirobifluorene) is a hole transport/electron blocking layer. We then modify the c-TiO2 / Perovskite interface by inserting a thin layer of phenyl-C61-butyric acid methyl ester (PCBM) which has shown to be valuable in passivating hysteresis and providing stabilized efficiencies **Figure 3-1(a&c)**. The perovskite is processed by evaporating PbI_2 which ensures that PCBM presence is only at the interface of the perovskite as we are able to discount any contributions of PCBM in the bulk or grain boundaries[37]. Also the morphology of the formed perovskite are quite similar in the two cases **Figure 3-1(b&d)**. We find that 1) the favourable interfacial energetics between the electron extraction layer and the perovskite at the TiO_2-$MAPbI_3$ interface change drastically, presumably caused by the accumulating I^- ions. Giant capacitances and accumulated charges observed in dark in these solar cells are present only at the interface and are caused by electronic charges and are not ionic; 2) PCBM at the interface mitigates the formation of interfacial trap states. With PCBM, no giant dark capacitances, accumulated electronic charges and low hysteresis are observed; 3) Transient measurements show that at the TiO_2-$MAPbI_3$

interface nearly 45% of the recombination occurs at the interface which is expected due to the in the presence of accumulated electronic charges at this interface. While in the PCBM-$MAPbI_3$ interface this recombination is negligible.

3.2 Device Performance

Figure 3-2 (a&b) shows the device performance for the two device structures.

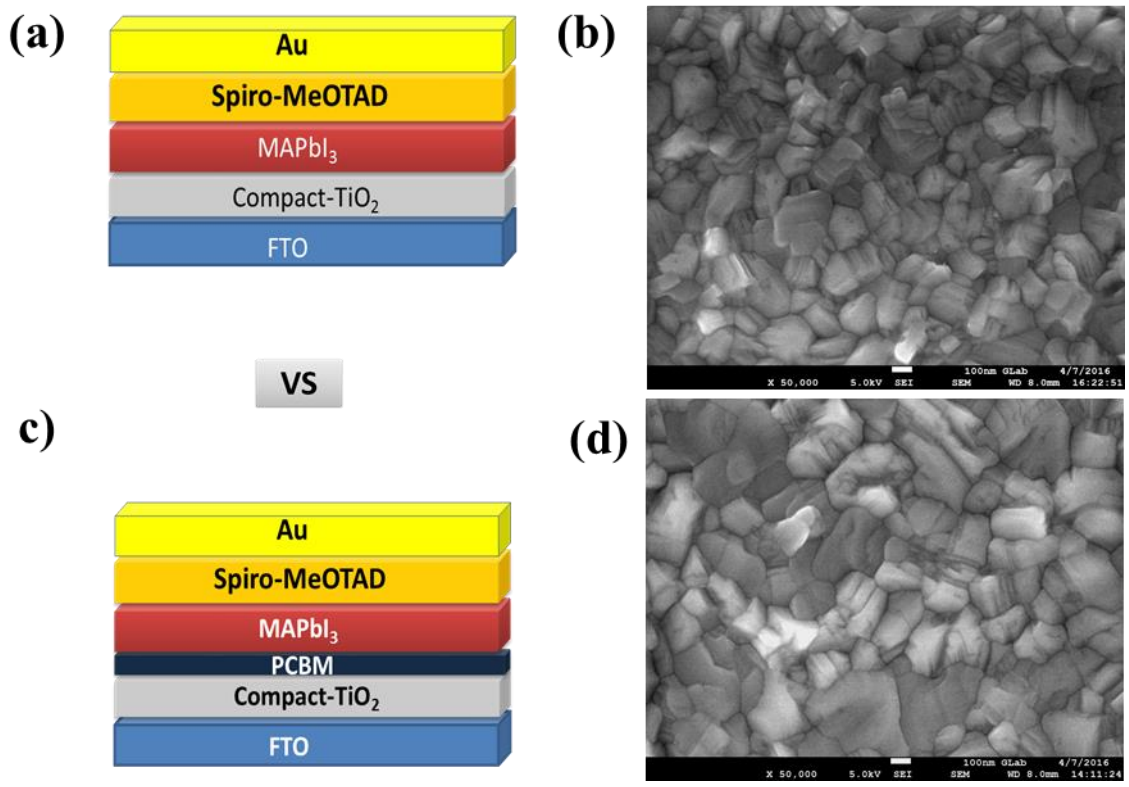

*Figure 3-1 **(a)&(c)** Schematics show the two device structures that are used in Chapter 3 and Chapter 4 with the difference being the EEL contacting the Perovskite. (b)&(d) show the Top View SEM of the Perovskites for the two device structures*

The IV-curves with a PCBM EEL shows lower hysteresis in the two scan directions from J_{sc}-V_{oc} and V_{oc}-J_{sc} at a scan rate of 50mV/s. Compare this with devices with TiO_2 EEL which shows much larger hysteresis. As often reported[26,27,38], the device based on bare TiO_2 as EEL has a J-V characteristic that depends on the polarization record of the device, while when PCBM directly interfaces the perovskite, the devices are electrically stable. Also the currents

and efficiencies of devices with the PCBM EEL are much higher.

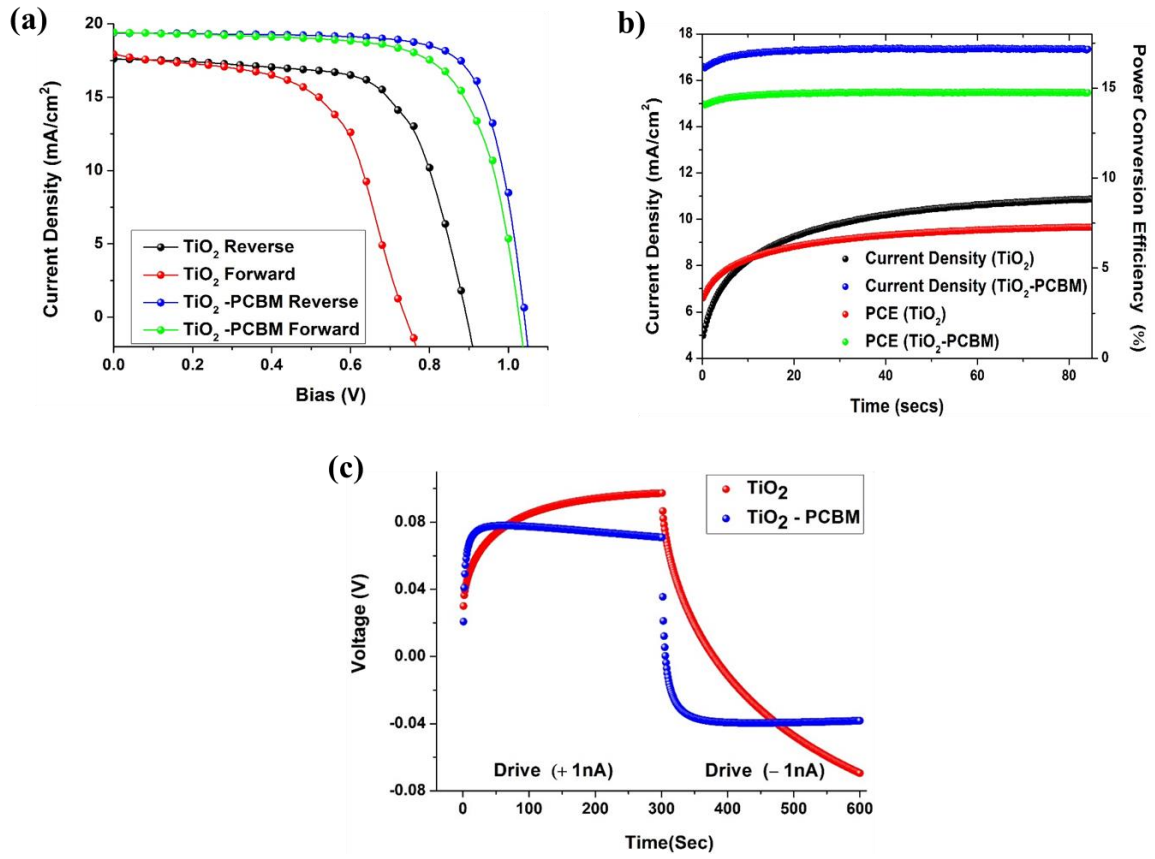

Figure 3-2 ***(a)*** *J-V Curves for the two perovskite devices* ***(b)*** *Stabilized power conversion efficiencies and current densities for the two solar cells* ***(c)*** *Chrono-Potentiometry curves for the two types of devices in dark with a drive of 1nA.*

In order to understand the basics differences standard Chrono-Potentiometry studies is performed where a constant current (±1 nA) is driven at forward bias the changes in voltages are monitored in **Figure 3.2c**. The response between the two samples is very different. While in presence of PCBM a plateau is reached quite fast, in presence of a simple TiO_2-Perovskite interface the voltage transient is much slower. Significant differences are observed when the polarity of the current is reversed. In presence of TiO_2, a slow repolarization of the voltage is observed when the driving current is switched sign, reminiscent of capacitive discharging of electronic charges. In the presence of PCBM the response is much faster (few secs) wherein the sign of the voltage follows that of the applied current. Maier and co-workers show an exponential dynamic of the voltage stabilization (i.e. $V \approx e^{xt}$) assigning it to an ion diffusion process within the perovskite bulk[39]. Even here, a similar exponential dependency for cells

with the TiO_2 EEL but an exponential behaviour is not found for devices with a PCBM EEL at the perovskite surface. Since both devices are identical and vary only in the interfacial EEL, this seems to suggest that the slow exponential change arises from an interface phenomenon and not the bulk diffusion of ions.

3.3 Dark Capacitance is Interfacial

To gain a better insight into the observed differences, impedance spectroscopy (IS) measurements are performed. In **Figure 3-3a**, frequency dependence of the real part of the complex capacitance in dark is plotted for these two types of devices. Large capacitances in the low frequency region is observed for devices with a TiO_2 as EEL. This is also what has been observed before[20,29–31,40–42]. An enormous increase in this capacitance is observed by applying a forward bias against the built-in voltage, which suggests this phenomenon does not arise from bias dependent aligning of polarizable species. Surprisingly, for the device with a PCBM EEL, this capacitance is orders of magnitude lower and is also independent of the applied voltage. Since both devices are similar in all aspects except the EEL contacting the perovskite, it clearly shows that the giant capacitances observed in the dark in $MAPbI_3$ are related to a purely interfacial phenomenon and not to the bulk perovskite layer. One concern regarding this interpretation is that the growth of Perovskite films depends on the substrate on which it has been grown, which may render the two films non-identical. However giant capacitances are observed for $MAPbI_3$ grown on almost all substrates and processing conditions, with consensus being developed in the research community that it is independent of the film growth conditions[43]. Also the crystal size changes observed for the two films are not large compared to the drastic quenching of the giant capacitance observed here. Hence the quenching is attributed to be a purely interfacial phenomena. Osbel et. al.[32] have recently suggested from their experiments with changing perovskite thickness, that the giant capacitances observed in the dark at low frequencies may originate from the interface. However

bias dependent changes were not probed. In these results, with a quenching of the giant capacitance at all voltages by solely modifying the interface evidence suggests towards the giant capacitances in dark originating at the interface.

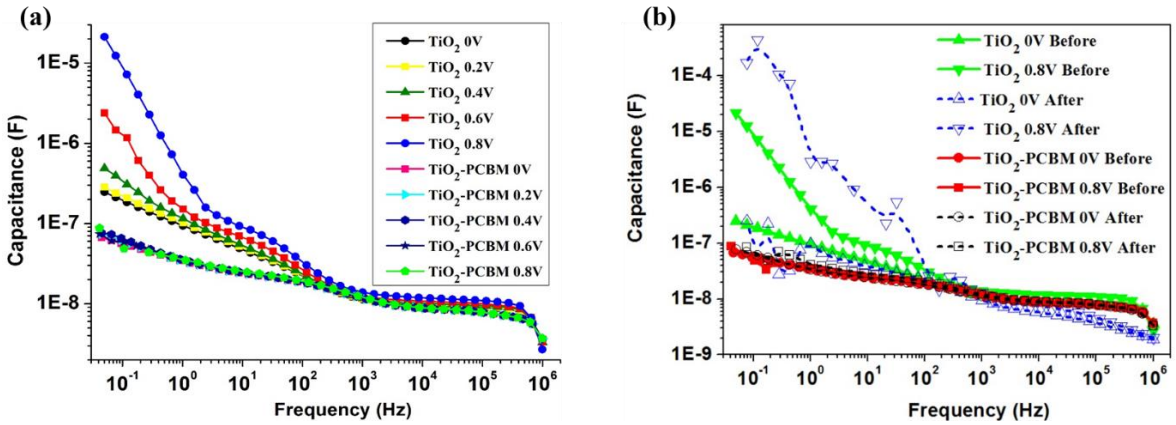

Figure 3-3 (a) Real part of the complex capacitance in dark is plotted as a function of applied voltage for the two devices with TiO_2 and PCBM EEL (b) The cells with the TiO_2 EEL show a continuous increase in the Giant Capacitance after light soaking the devices; while devices with a PCBM EEL remain stable with light soaking

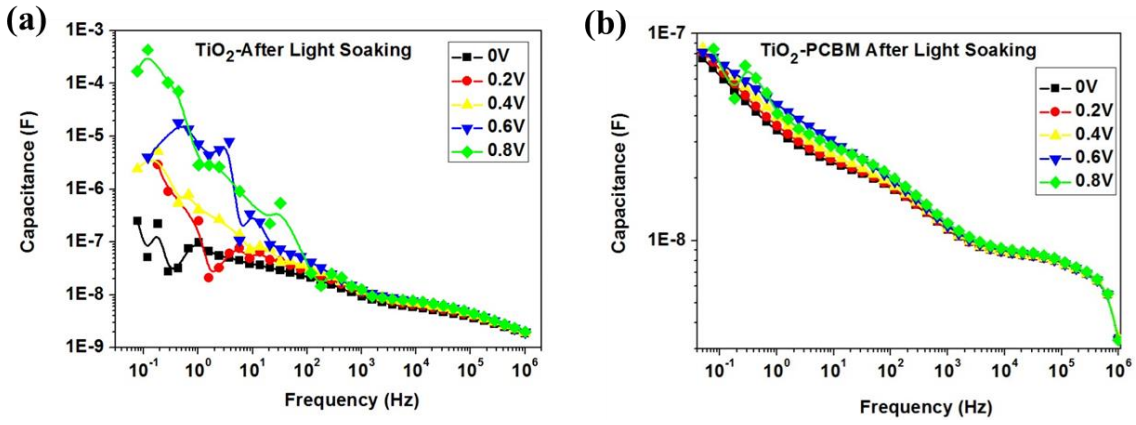

Figure 3-4 a) Large Noise in the EIS data for solar cells with the c-TiO_2 layer. b) Such noise measurements are not seen in devices with TiO_2-PCBM extraction layers

In order to look deeper into the stability of the respective interfaces IS in dark is measured after light soaking the samples in both short circuit and open circuit conditions in **Figure 3-3b**. A large increase in dark capacitance is observed after light soaking for the TiO_2 based devices. Such an enhancement is attributed to an increased injection of electronic charges as will be seen in chapter 4.

As seen from **Figure 3-4a** large noise is observed in measurements after light` soaking for the TiO_2 based solar cells. Large integration times as well as large averaging does not supress the large noise. Presence of ionic double layers in ionic conductors and ionic motion are known to cause noise at low frequencies[21,22,44]. $MAPbI_3$ semiconductors are also well known to demonstrate such a motion and accumulation of ions, which then indicate the large noise to be an effect of ions. For the PCBM EEL cells, surprisingly no drift in the giant dark capacitance and noisy data are not observed with light soaking. Since the two types of solar cells are similar in all aspects but the interface we expect the extent of ionic motion in the two cells to be similar. The lack of any noise in the case of PCBM then suggests towards a physical passivation of these ions in the PCBM cells which will be seen in the next chapter.

3.4 Case for Electronic Charge Accumulation for TiO_2 Interfaces

Large Capacitances in $MAPbI_3$ solar cells have been one of the long standing questions that have perplexed the research community. It was initially assigned to a ferroelectric process or polarization of ionic bulk species which have however been shown not to be the case[45,46]. Accumulated ions at the interface creating a double layer capacitance was also ruled out due to the sheer magnitude of the capacitance observed (~mF). One of the key observations by Osbel et.al recently suggest that the large capacitances in dark may arise from the interface. The exact nature of mechanism still remains unknown. Recently Isaac et.al. suggest polarization of the perovskite contacts as a possible mechanism for obtaining such large values observed in perovskites[33]. They find a standard Capacitance Vs Voltage plot with a slope of $q/2k_BT$. A $q/2k_BT$ dependency is usually observed during the formation of accumulation zones of electronic charges at a semiconductor-oxide interface in Metal-Oxide-Semiconductor interfaces, where the fermi-level of the semiconductor is pushed close to the band edge by applying voltages to the oxide. The formation of accumulation zones is used to drive Metal Oxide Field Effect Transistors (MOSFETs) in the accumulation regime[47].

As observed by Isaac et.al. also here, a $q/2k_BT$ slope for the giant capacitance is observed at low frequencies as a function of voltage (**Figure 3-5a**). A closer look at the frequency dependence shows that as we move to higher frequencies, the $q/2k_BT$ dependency decreases. This initially suggests the presence of a text book like accumulation-depletion capacitance observed in Metal-Oxide-Semiconductor interfaces. However applying a reverse bias a symmetrical trend in frequency is seen, unlike what is observed for depletion regime capacitances. This gives first suggestions that an accumulation zone capacitance model may not be at the origin of the large capacitances observed here.

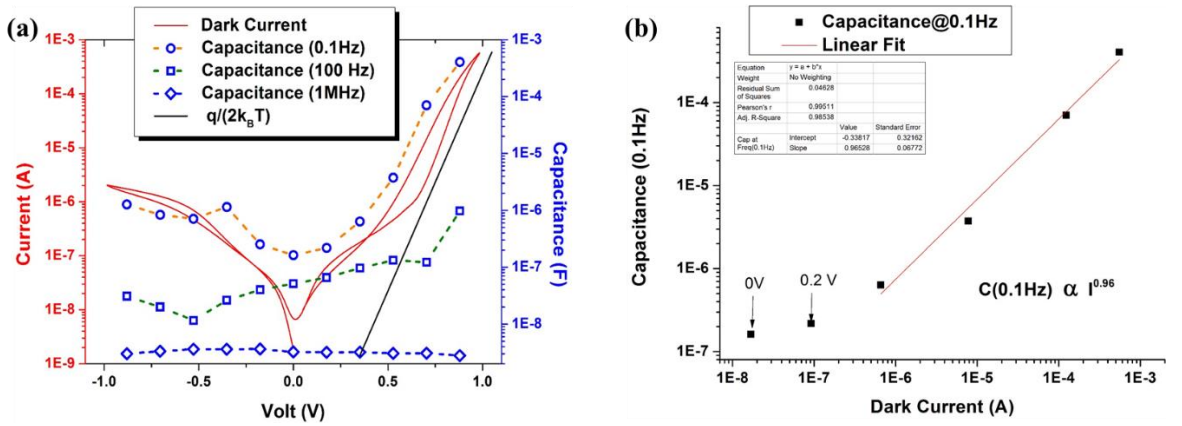

Figure 3-5 (a) Frequency dependence of low frequency capacitance and its co-relation with the injected dark current. The straight line is a line with a $q/2k_BT$ slope (b) A linear co-relation between the Current and Capacitance. A fitting of slope of 0.88 is observed with the 0.2V point included in the fit

Surprisingly the low frequency giant capacitances observed have a direct correlation with the injected dark current within the device. This correlation holds true for both forward and reverse biasing of the device which suggests that this large capacitance is partly related to the injected dark current and not only the formation of accumulation zones. We find that the capacitance is directly proportional to the injected dark current with $C \alpha I^{0.96}$ with an exponent of 0.88 obtained with a 0.2V point included. At 0V with zero-current, of course a Zero-Capacitance is not expected where the influence of the bulk and other layers is expected to have a significant contribution. Such a correlation between device currents and measured capacitances are rare.

Interestingly a p-n junction operated at forward bias shows a diffusion capacitance directly proportional to the dark current (given by $(q\ I_D\ \tau)/\ 2k_BT$, where I_D is the injected dark current and τ is the carrier lifetime) and is set up by the field created by the majority electronic carriers diffusing across the depletion region. Such a dependence cannot be ruled out in our case where trapped electronic charges at interfaces can possibly set up a field at the interface.

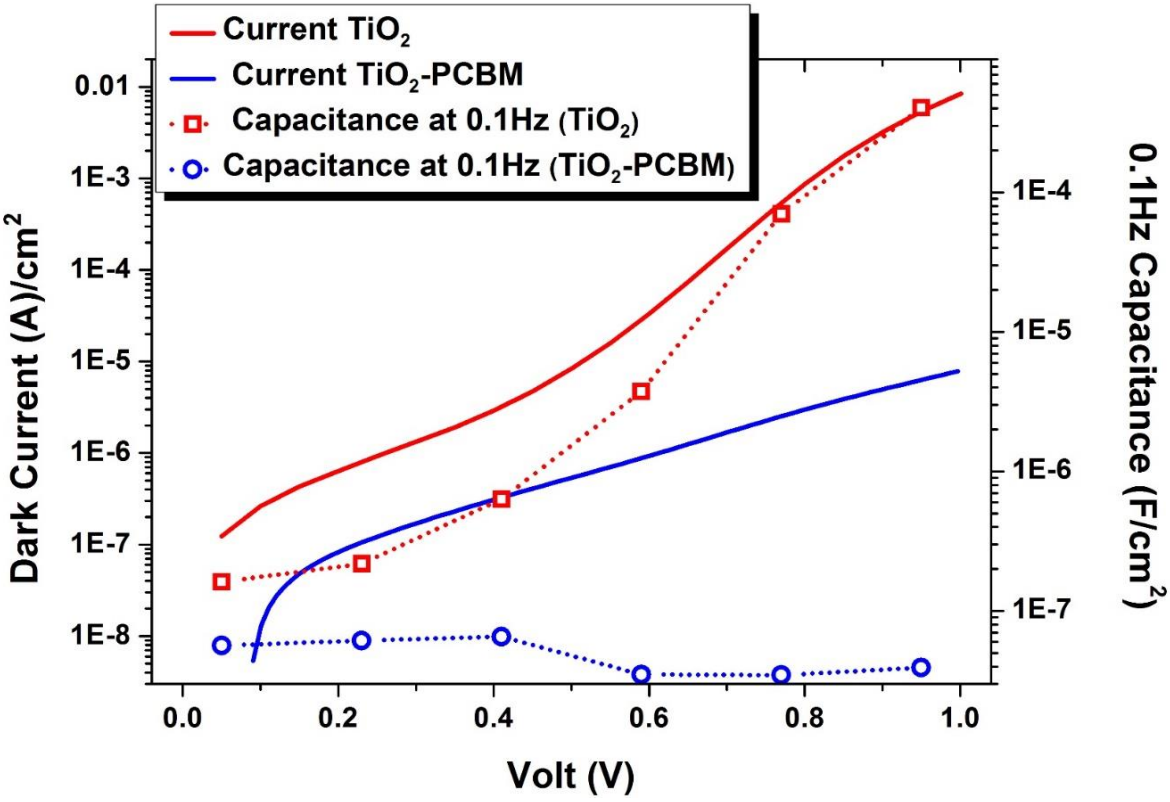

Figure 3-6 Difference in the Capacitance Vs Injected Dark Current for solar cells with the two types of contacts

Solar cells with a PCBM EEL do not show such a correlation with the injected current in the device (**Figure 3-6**). Even at the similar injected dark currents the dark capacitances vary significantly. Polycrystalline MAPbI3 perovskite films have shown trap densities in the range of ~ 10^{14}-10^{17} /cm3 which are orders of magnitude higher than that observed in crystalline GaAs[9,14,16,18,19,48]. Also Sargent and co-workers have shown an effective passivation of trap states originating by anti-site iodide defects by fullerene molecules[38]. Hence trapped charges at the interfaces may very well be the origin of the large capacitances observed in dark at low frequencies and also the origin of the slow transients observed in CP and other similar studies[39].

3.5 Interfacial Polarization in Light

Consistent but larger differences are obtained when IS is performed under 1 Sun illumination

Figure 3-7.

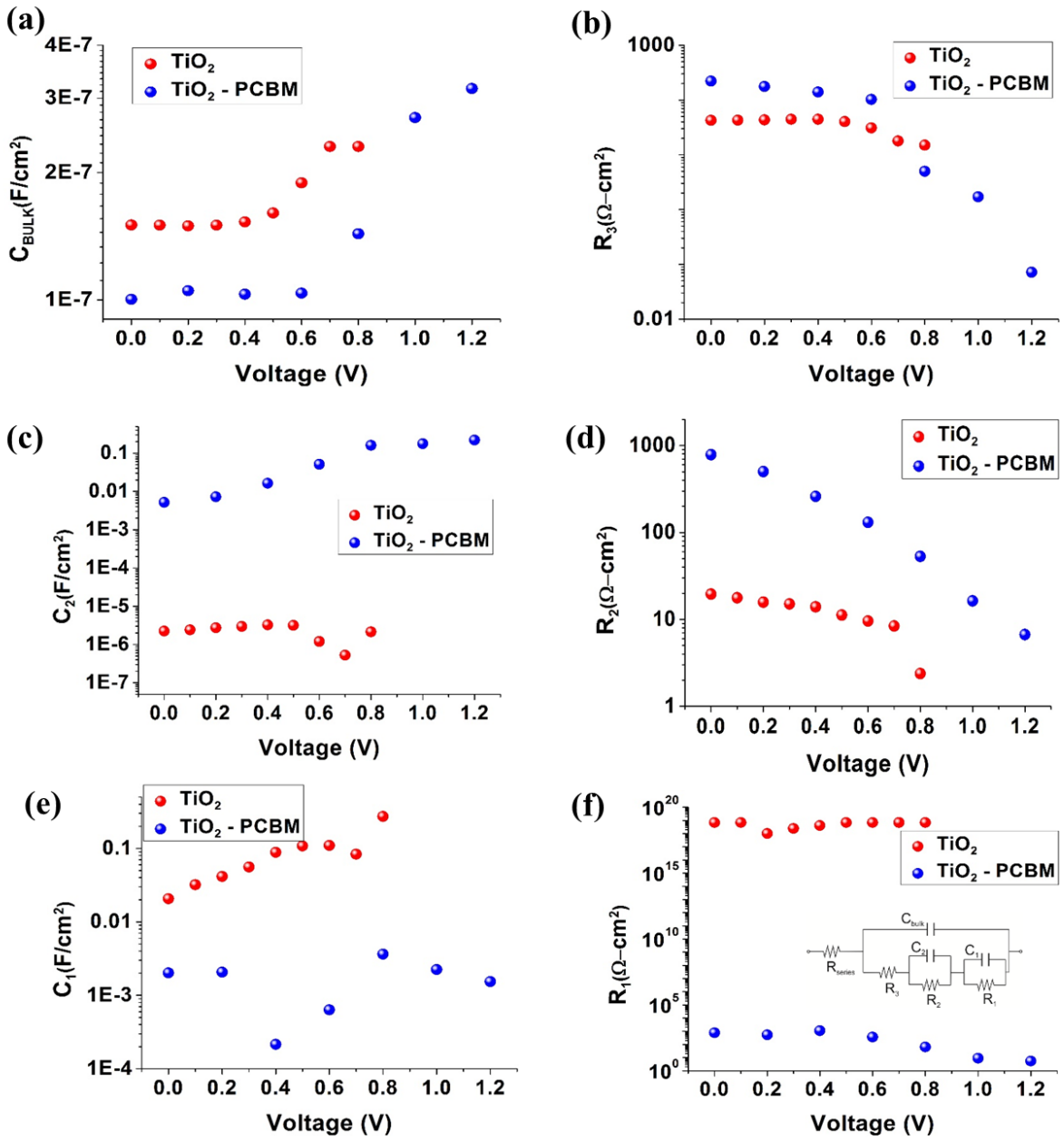

*Figure 3-7 Impedance spectroscopy parameters R_1-C_1 **(a,b)** R_2-C_2 **(c,d)** R_3-C_3 **(e,f)** under 1 sun light intensity for TiO_2 cells (ITO/TiO_2/$MAPbI_3$/Spiro/Au) circles in red and for TiO_2 – PCBM cells (ITO/TiO_2/PCBM/$MAPbI_3$/Spiro/Au) circles in blue, resulting from the equivalent circuit in the inset in **(f)***

The circuit model for the solar cell in light is shown in the inset of **Figure 3-7f** as recently proposed by Antonio et.al[31]. The applied model is the only model that is consistent with the IS of various planar $MAPbI_3$ solar cells observed from low frequencies (0.1Hz) up to 1MHz. The basic parameters of the model to the present level of understanding are explained. C_{bulk} is related to the bulk capacitance of the perovskite, which are related to the multiple dipolar mechanisms reported previously[43]. R_3 on the other hand corresponds to the transport resistance of the perovskite with contribution from the contacts for low efficient devices. The low frequency large capacitance (C_1) gives information regarding the contact polarization effects [23,29,31,32,49,50] caused by the interfacial double layer of accumulated ions and electronic charges at the interface. R_1 provides the resistance of the polarized contact in the presence of this double layer. The origin of R_2 and C_2 is yet to be completely established, however preliminarily studies suggest their origin related to additional interfacial states in solar cells.

The parameters C_{bulk} and R_3 show nearly identical values for the two cells, which confirm the validity of the assumption of identical bulk perovskites for the two cases. On the other hand, in the low frequency range, parameters R_1 and C_1 related to the polarization of the interface in perovskite solar cells show much larger values for the TiO_2 contact than those for the PCBM cells. It is important to note that for the TiO_2 contact the resistance is so high that it is only observed the beginning of the arc. Then, R_1 values are an extrapolation that leads to values beyond the detection limit of the potentiostat with large associated errors. Much larger R_1C_1 values indicate much larger polarization of the TiO_2 contact w.r.t. the PCBM contact. This indicates that the major contribution to R_1C_1 arises from accumulated electronic charges at the TiO_2 interface like in dark.

The accumulation of ionic charges can be ruled out, since the extent of ionic motion and accumulation in the two devices are expected to be similar and also as referred earlier, the magnitude of the capacitance values cannot account for the accumulated ions by itself. In the

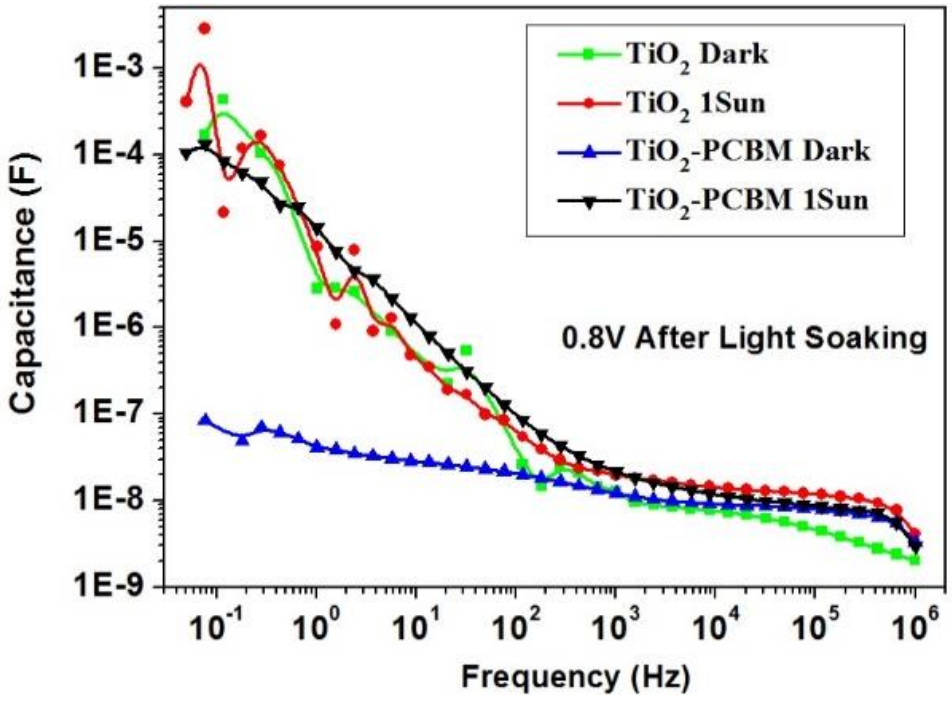

Figure 3-8 Comparison of the C-f curves for high electronic charge density conditions in dark and light

intermediate frequency range, parameters R_2 and C_2 show larger values in the case of bare PCBM EEL than the TiO_2 EEL, suggesting that hysteresis in $MAPbI_3$ solar cells are more reliant on contact polarization and charge accumulation (R_1,C_1). The combined analysis indicate that the slow transients observed in perovskite solar cells may be due to the different characteristics in the time constant $\tau_1 = R_1 C_1$. From **Figure 3-7e**, PCBM greatly decreases the interfacial capacitance, consequently in literature devices with PCBM contacts in standard as well as inverted structures show quick responses to external electrical perturbations and changing polarizations. The role of electronic charges is also visible in **Figure 3-8** where the low frequency capacitance for large injected currents in dark (near V_{oc}) approaches of what is observed in light. It is important to note that in the presence of light electronic charges required for accumulation are light generated.

3.6 Charge Transport and Recombination: Transient Photocurrent and Transient Photovoltage

Accumulated interfacial electronic charges at the interface is expected to give rise to a trapping affected transport and large recombination of electronic charges at this interface. A useful tool to track this is the small perturbation Transient Photo-Voltage (TPV) and Transient Photo-Current (TPI) measurements as described in Chapter 2[11,14,16].

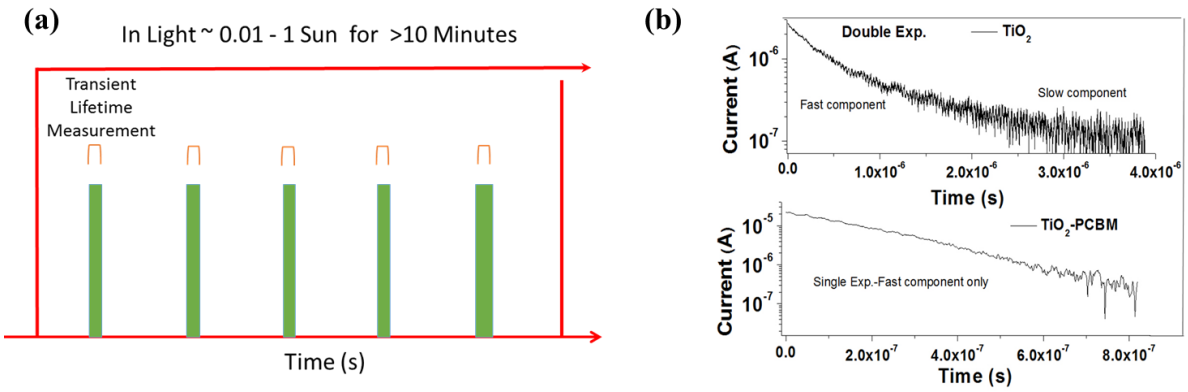

Figure 3-9 (a) Experimental scheme for Transport Measurements where the measurements are performed over a period of ten minutes.(b) Semi-log plot of the transient current responses for devices with a TiO_2 EEL and with a PCBM EEL showing a clear bi and mono exponential behaviour respectively

Measurements are made at regular intervals of 30s (30s of averaging) for a period of 10 minutes as shown in **Figure 3-9a**. We first proceed to see the effect of accumulated interfacial electronic charges and the lack of it in TiO_2 and PCBM EEL devices respectively. In TPI the transport dynamics of charges in solar cells kept at short circuit condition is tracked and since a 100% EQE is not guaranteed, recombination and trapping at short circuit also exists. In TPV the recombination dynamics of electronic charges in solar cells kept at open circuit conditions is tracked. Typical transient dynamics are shown in **Figure 3-9b** which is shown for the TPI. Samples with a PCBM EEL typically show a mono-exponent decay while devices with a TiO_2 EEL typically show a bi-exponential decay.

TPI transients give the transit time of charges in solar cells at short-circuit. A mono-exponential (τ_{1T} ~ 200 ns) extraction lifetime of charges is found from devices with a PCBM EEL and a bi-exponential extraction lifetime of charges (τ_{1T} ~ 300ns and τ_{2T} ~ 1 µsec) from devices with only a TiO_2 EEL. 'T' stands for transit. The τ_{1T} of the two cells with TiO_2 and TiO_2-PCBM are well matched indicating this decay related either to the bulk transit time of charges or the extraction time of holes at the Spiro-OMeTAD-$MAPbI_3$ interface. $MAPbI_3$ inverted solar cells with a different hole extraction layer of PEDOT:PSS (with the same PCBM electron extracting layer) also exhibit a single exponential lifetime of ~ 250ns, which matches well with τ_{1T} observed here(ref). This suggests that τ_{1T} is related to the bulk transit time of charges as it remains constant for $MAPbI_3$ solar cells with different extracting layers. In any case, the additional slower component τ_{2T} present only in the TiO_2 devices demonstrate that transit times of charges increase due to the c-TiO_2-$MAPbI_3$ interface. This indicates trapping of electronic charges at the c-TiO_2-Perovskite interface that are not present in the PCBM-Perovskite interface.

Turning to the transient photo-voltage signals (which are similar to as shown in **Figure 3-9b**) measuring recombination dynamics at open circuit, a strong bi-exponential behaviour of recombining charges for the cells with the TiO_2 interface (τ_{1R} ~400ns & τ_{2R} ~5 µsec) is observed. For solar cells with a PCBM interlayer a weakly bi-exponential dynamics in the recombination of charges (τ_{1R} ~300ns & τ_{2R} ~3 µsec) is observed only for the first few minutes of light soaking the solar cells. Also in these first 1-2 minutes the exponential is predominantly dominated by τ_{2R} (>90%). After about 2 minutes only a mono-exponential

dynamic of τ_{2R} remains for the PCBM with τ_{1R} dying. The τ_{2R} of the two cells with TiO_2 and TiO_2-PCBM match well indicating this decay to be related to the bulk recombination of charges or recombination at the Perovskite-Spiro-OMeTAD interface. Recent reports of $MAPbI_3$ solar cells with different hole extraction layers of PEDOT:PSS (with a PCBM electron extracting layer) also show a single recombination lifetime of charges (~ 2-5 µsec) which coincides well with τ_{2R} observed here. Similar lifetimes of trapped electronic charges (few µsec) in the bulk perovskite have been observed from Transient Absorption studies (ref). This commonly observed lifetime observed for all these different devices (τ_{2R}) then should represent the bulk recombination of charges. The additional τ_{1R} observed only in the TiO_2 cells (after the cell stabilizes with ~1-2 minutes of light soaking) arises due to a secondary recombination pathway of charges at the c-TiO_2-perovskite interface. The electrostatic interaction between the accumulated ions and the electronic charges creating this extra component also can be ruled out since the extent of accumulated ions are expected to be similar in all devices which should then give rise to this extra component in all device structures. Also TPV is performed at open circuit conditions at 1 Sun where we would not expect accumulated ions at interfaces which should lead to a weaker bi-exponential behaviour that is not observed here. Hence the electrostatic interaction between the electronic charges and ions are not at the origin of the observed differences.

To plot succinctly, the evolution of the transport/recombination of charges in time is tracked while the solar cells are kept under continuous light soaking. The evolution of the transit lifetimes is shown in **Figure 3-10a**. The faster lifetimes associated with the bulk perovskite (τ

$_{1T}$) remains stable with light soaking for both the devices. However for the cells with a TiO_2 interface, the trap assisted transport lifetime (τ_{2T}) related to the TiO_2-pervoskite interface

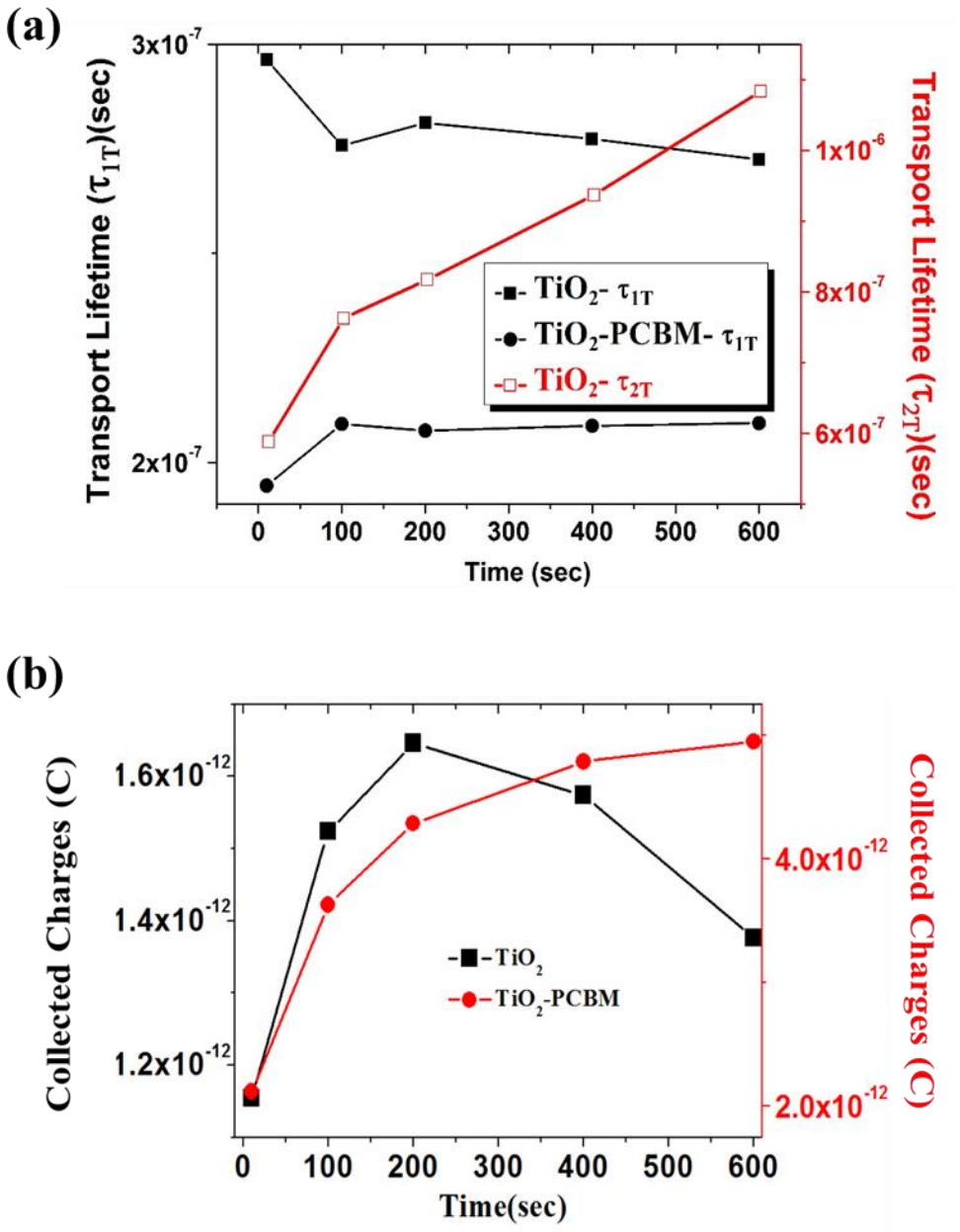

Figure 3-10 (a) Evolution of Transport lifetimes under 1 Sun illumination is shown for the two different photovoltaic cells. The slower component in transport (τ_{2T}) in (a) is only present for TiO_2 photovoltaic cells. (b)Collected Charges per pulse showing the stability of the TiO_2-PCBM devices. The initial increase in both the cells is yet to be clearly understood, but can be attributed to a trap filling phenomena

continuously evolves becoming slower with light soaking. This indicates a dynamic increase in trapping at this interface in short circuit conditions. This slow increase in trapping over many minutes may be indicative of drifting ions accumulating at the interface creating these traps.

This is also in line with what was seen earlier with IS studies where an increased dark capacitance after light soaking is found. From TPI the dynamics of collected charges per perturbation light pulse is shown for the two devices in **Figure 3-10b**, which shows the stability of the PCBM interface. Over a period of 30 minutes we do indeed find a continuous decrease in collected charges for the devices with a TiO_2 EEL while devices with a PCBM EEL remain stable.

For the evolving recombination dynamics, the changing TPV lifetimes are plotted **Figure 3-11a**. (τ_{2R}) associated with the bulk recombination of charges remains stable with light soaking for the two cells. Surprisingly the recombination lifetimes (τ_{1R}) associated with the TiO_2 interface also remains quite stable after an initial decrease. In order to quantify the contribution of the secondary pathway of recombination arising from the TiO_2–$MAPbI_3$ interface, the contribution of τ_{1R} as a percentage of the total recombination is plotted in **Figure 3-11b**. For this calculation the amplitudes of the two fitted exponents (τ_{1R} & τ_{2R}) are compared. The interfacial recombination contributes to as much as 45% of the total recombination in comparison to a negligible amount for the TiO_2-PCBM interface. This again is a signature of large electronic charge accumulation at the interface wherein recombination of charges occurs in the region of maximum charge density. Continuous tracking of the real-time changes in transport and recombination shows a continuous build-up of electronic trapping which slows charge transport and provides a strong secondary pathway for recombination at the TiO_2-perovskite interface. It is likely that the continuous degradation of the interfacial energetics and accumulation of interfacial trap states observed here leads to the dark giant capacitance seen from IS measurements.

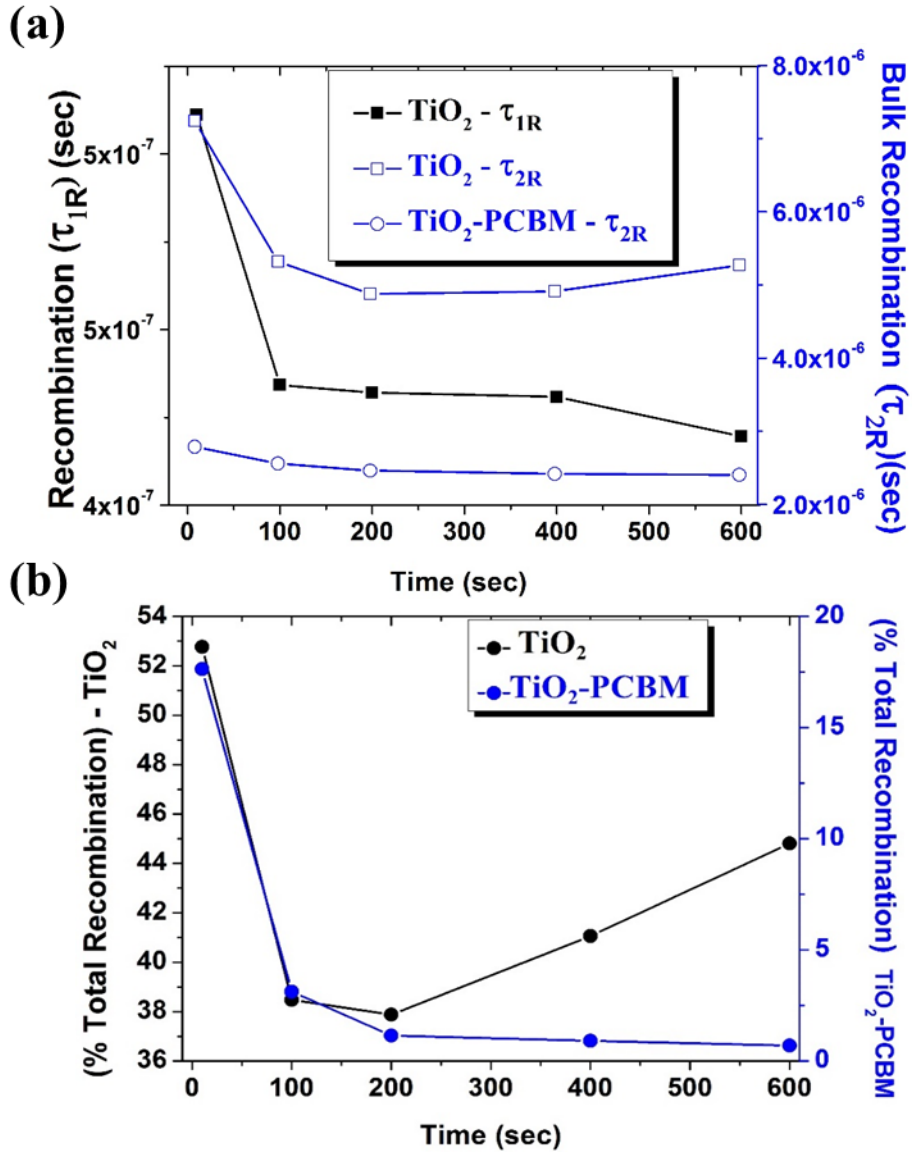

Figure 3-11 (a) Evolution of Recombination lifetimes under 1 Sun illumination is shown for the two different photovoltaic cells. The faster component of recombination (τ_{1R}) is negligible for cells with PCBM interlayers and not shown in (a). (b)The evolution of the of interface recombination under 1Sun illumination as a fraction of the total recombination is shown in the solar cell

3.7 Conclusion

We now summarize all our observations. It is worthwhile to remember that since the perovskite here is formed by partial evaporation, the PCBM layer remains intact and the two cells remain similar in the other aspects. Also the PCBM is only present at the interface and not in the bulk. Hence changing properties between the two devices are attributed to interfacial phenomena and

surface effects while the bulk $MAPbI_3$ semiconductor effects can be ruled out. A schematic depicting the conclusions is shown in **Figure 3-12.** From dark IS large capacitances at low frequencies for TiO_2-$MAPbI_3$ devices is seen which is supressed in the presence of PCBM at the interface. A direct correlation between the injected dark current and the low frequency giant capacitance in the TiO_2-$MAPbI_3$ devices is observed which is not present in devices with a PCBM EEL. This indicates large electronic charge carrier accumulation at the TiO_2-$MAPbI_3$ interface in dark. The large increase in capacitance with injected current also indicates that the electronic charge contribution would dominate the formation of a double layer at the interface than the ionic contribution. Similar trends in the presence of light are observed with much larger interfacial capacitances at low frequencies for the TiO_2 devices. The large low frequency capacitances in dark and light lead to the presence of a much larger RC time constants for the TiO_2 devices. This explains the presence of a slow changing response of these devices to external perturbations and which consequently lead to I-V hysteresis in dark and light, slow changing C-P transients, unstable DC currents with applied voltages and others.

From TPI/V a concomitant increase in trapping of electronic charges and the formation of a secondary pathway for recombination of electronic charges at the TiO_2-$MAPbI_3$ interface is observed. These processes evolve in time under light soaking which suggest towards a slow accumulation of trap states at this interface. This accumulation of interfacial trap states which are capable of holding electronic charges may be at the origin of large capacitances observed in the dark in the TiO_2-$MAPbI_3$ devices. Such formation of interfacial traps is not present in the PCBM devices, which is consistent with the absence of large capacitances in these devices. Hence devices with PCBM show smaller RC time constants, small hysteresis, and fast transient response to C-P experiments.

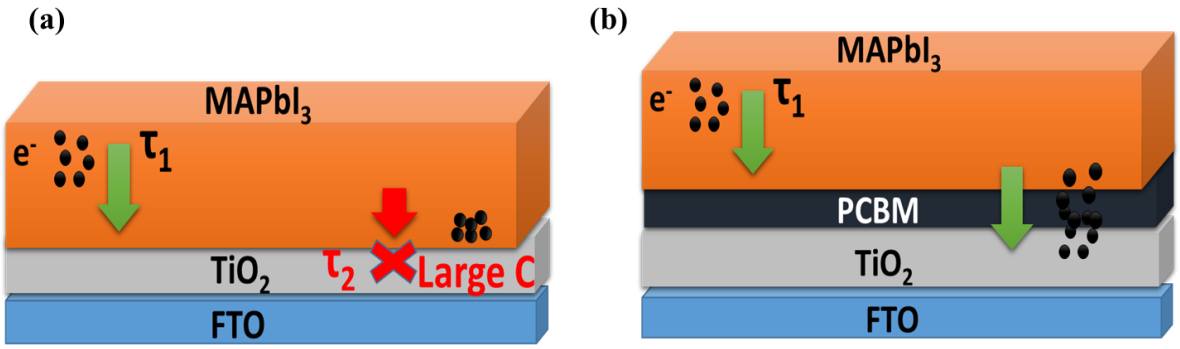

Figure 3-12 Schematic depicting the dynamics of electronic charges (either electrons/holes) in the two devices. (a) Shows the trapped transport/recombination of electronic charges at the TiO_2-$MAPbI_3$ interface creating the large low frequency capacitances at the interface and (b) Shows the efficient transport of charges across the PCBM-$MAPbI_3$ interface

In the next chapter an argument is put forth supporting the case that it is quite likely that these accumulation of interfacial states/interfacial electronic charging are caused by the accumulation of I^- ions, which are the most mobile ions[51] in $MAPbI_3$ perovskites and accumulate at the EEL interface. Accumulated ions creates defect in crystals that have shown to form electronic trap states in the deep band-gap, band edge as well as in the conduction band[51,52] by been Density Functional Theory predictions. The question of how PCBM then passivates the accumulating I^- is then probed in the next chapter. This idea is consistent with majority of the charges accumulating at the interface being electronic

4 Investigating the Roles of PCBM in $MAPbI_3$ Solar Cells

4.1 Background

First, a recap in brief the relevant details of Chapter 3 essential here. In the last chapter two device structures differing only in the EEL were considered. Much larger hysteresis, trapped transport of electronic charges, recombination and large accumulation of electronic charges in devices with the TiO_2 EEL were found. A simple introduction of a thin PCBM layer between $MAPbI_3$ and TiO_2 completely supresses the observed hysteresis, trapped transport, recombination and leads to a suppressed accumulation of electronic charges in the device. For the TiO_2 devices these characteristics slowly drift in time under 1Sun light soaking, for example the transit of charges become slower and slower in time and under light from trapping of electronic charges. It was suggested that this slowly drifting electronic properties may be an indirect effect of the slowly accumulating ionic species in $MAPbI_3$ solar cells.

The existence of moving ions in $MAPbI_3$ solar cells is well documented with I^- and MA^+ ions having the lowest activation energies along with the motion of their respective vacancies in the crystal[25,26,35,39,45,53–57]. As the two solar cells studied here are similar in all aspects except the EEL, the magnitude of ionic motion is expected to be similar in the two cases. Besides, small changes in crystal sizes and the role of substrate in the crystallization of $MAPbI_3$ have shown to have low effects on the motion of ions and their activation energies[11,25,26,44,53,58]. Hence the

magnitude of ionic motion can be assumed to be similar in the two cases. It then becomes significant to probe how the presence of PCBM as an EEL at the interface passivates the build-up of these trapping electronic charges and large capacitances which in turn could be related to the accumulating ions at the interface. Since it is the I^- that accumulate towards the EEL, the role of I^- and vacancies of MA^+ at the EEL interface is of significant interest.

Three seminal reports on the interaction $MAPbI_3$ with PCBM have been reported. The first report by Sargent.et.al[38] show that by adding PCBM in $MAPbI_3$ in solution, an active doping of PCBM by I^- in the solution phase occurs (by formation of a PCBM polaronic peak). Standard DFT calculations show that the halide can easily interact at room temperature with anti-site iodide defects (wherein I^- takes the place of Pb in the crystal) in perovskite as they do in solution. However formation of anti-site defects have yet to be studied in terms of formation energies and their presence is yet to be detected. The second report from De Batiani et.al [27]. show an active interaction between the MAI and PCBM in the solution phase and demonstrate the effect on the electronic characteristics in solid state devices. Lastly Huang et al.[59] show from Thermal Admittance Spectroscopy (TAS) that PCBM decreases the trap density of states by two orders of magnitude in $MAPbI_3$ solar cells. However like in the previous cases, they use an inverted structure wherein PCBM is present not only in the interface but also in the grain boundaries of the $MAPbI_3$ semiconductor. While in our experiments we only observe only the interfacial effects. Two key questions that need to be answered are:

1. Since most devices are made in solid state the basic question that needs to be addressed: Is the same interaction observed in solution phase also valid for solid state devices? If not, then the dynamics of the interaction observed in solution is of no consequence to what is observed in the devices here.
2. In case of a reaction occurring, how does it affect the interfacial energetics and how does it affect electronic transport-recombination?

An attempt to answer these relevant questions is made in this chapter. Further, explanations of our observations in context with the results of the earlier chapter 3 are provided.

4.2 Solid State Reaction between Moving Ions and PCBM

To experimentally tackle point number one of the possibility of a solid-state reaction between the iodide ions and the PCBM we move to a horizontal device architecture to overcome the difficulty of buried interfaces **Figure 4-1a** (Inset). A sensitive technique of Photothermal Deflection Spectroscopy (PDS) is employed. The aim of this experiment is to check the presence of polaronic charges in our devices that would exist in the presence of doped PCBM. Since PDS is sensitive to transparent conductive oxides and metals the substrate used is quartz. The PDS spectra of the Perovskite-PCBM device shows highly enhanced sub-bandgap features during poling and after relaxation of the device in **Figure 4-1a**. This is suggestive of formation of polaronic charges indicating the presence of doped PCBM in these films.

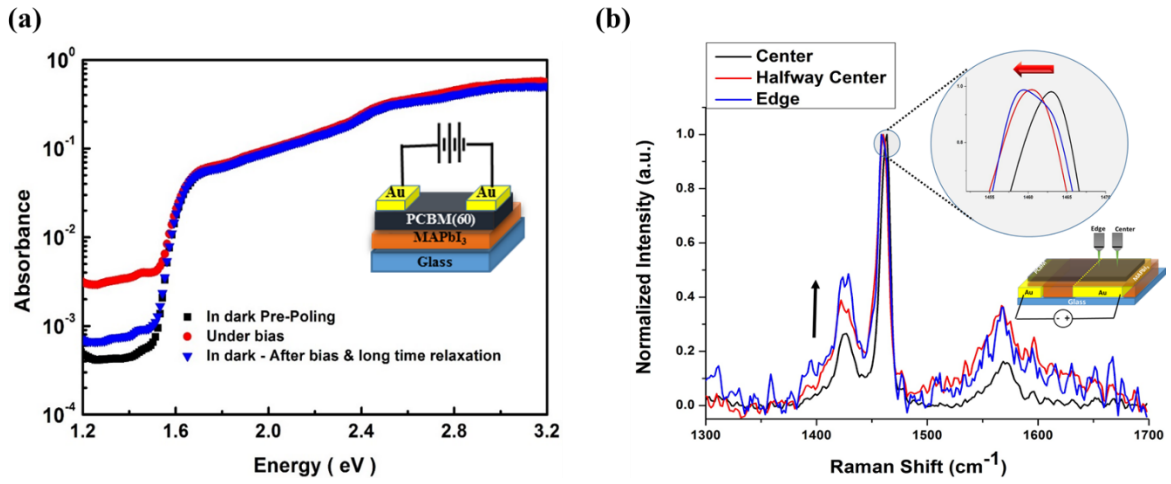

Figure 4-1 (a) PDS spectra on PCBM-$MAPbI_3$ showing the presence of increased charges at lower sub-bandgap energies indicating the presence of polaronic species (b) Raman Spectra of PCBM on top of the positively biased electrode during poling. Zoomed in region shows the shift in the $A_g(2)$ peak towards lower wavenumbers. Inset: Planar geometry of the sample used for position dependent doping

To chemically verify the presence of the radical species Raman measurements are performed, which has been effectively used in quantitatively tracking the doping of PCBM[60]. We maintain

the planar structure geometry (Au electrodes placed below the Perovskite-PCBM bi-layer for a better S/N ratio). Surprisingly Raman measurements of PCBM on top of $MAPbI_3$ do not demonstrate any chemical shift, w.r.t. the Raman of PCBM on glass. Since Raman of pristine PCBM and PCBM on $MAPbI_3$ are same, no chemical interaction between $MAPbI_3$-PCBM in the solid state seems to occur. However, the possibility of an interaction between the accumulating ions (I^-) in the perovskite film and the PCBM still remains.

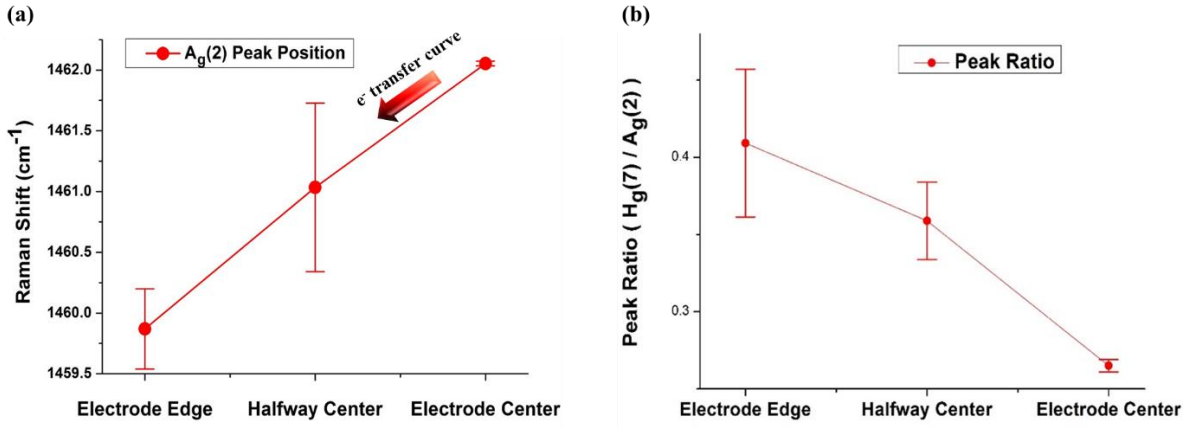

Figure 4-2 (a) Shift and of the $A_g(2)$ peak towards lower wavenumbers as we move from a region of large concentration to a lower concentration of diffused ions confirming charge transfer between moving ions and the PCBM in solid state. (b) The decrease of the relative intensity of the $A_g(2)$ peak is also shown which is a characteristic of electron transfer to PCBM

In order to induce ionic motion, the sample is poled in the presence of light (1 Sun / N_2) where I^- move towards the positive electrode. Since the motion of ions are diffusive in nature, a build-up of ions at the edge of the positive Au electrode is expected. Also one would expect a decreasing concentration of I^- ions as we move from this edge of the electrode towards the centre of the electrode. After poling, Raman measurements are taken across the positively biased Au electrode, from the centre towards the edge as shown in the inset of **Figure 4-1b**. **Figure 4-1b** shows the background corrected Raman spectra change as the measurement area is moved from the centre of the electrode to its edge. The $A_g(2)$ peak related to the pinch mode of PCBM (breathing of the cage) shifts towards lower wavenumbers, and also decreases in

relative intensity with respect to the other peaks. A shift to lower wavenumbers of the $A_g(2)$ peak conclusively provides evidence of a charge transfer to PCBM[60].

The changes in the $A_g(2)$ peak position from the 'Electrode Center'(lowest accumulation of ions) to the 'Electrode Edge' (largest accumulation of ions) is shown in **Figure 4-2a**. The decrease in the peaks relative intensity with respect to the $H_g(7)$ peak is plotted in **Figure 4-2b**. A minimum of 2.18 cm^{-1} shift is observed at the electrode edge which yields a modest doping of $0.3e^-$ transfer[60]. A lower shift is observed as we move towards the centre. Importantly at the centre of the electrode the spectra matches well with pristine PCBM [61] indicating the existence of a lateral doping profile in the PCBM film as we move from the electrode edge to the electrode centre. The larger error bars for the measurements in the doped regions is also evidence of an uncontrolled doping of PCBM due to the diffusing I^- ions. All these results indicate that motion of I^- is necessary for a solid state charge transfer to take place between the perovskite and PCBM. In the absence of such an ionic motion and accumulation of ions no interaction takes place between $MAPbI_3$ and PCBM. It must be noted that the electric field applied here (10V/mm) is much lower than what is present in working solar cells (~3000V/mm). Hence with more effective motion of ions in $MAPbI_3$ solar cells, solid state solid state reaction is bound to occur in the cells between the accumulated I^- and the PCBM interfacial layer. Once I^- dope PCBM, a charge transfer complex formation is expected[60,61]. It is interesting to note that the formation of charge transfer complexes should decrease the drift diffusion mobility of I^- ions themselves, thereby also acting as physical traps for the moving ions.

4.3 Changing Work-Function and Electrical Properties

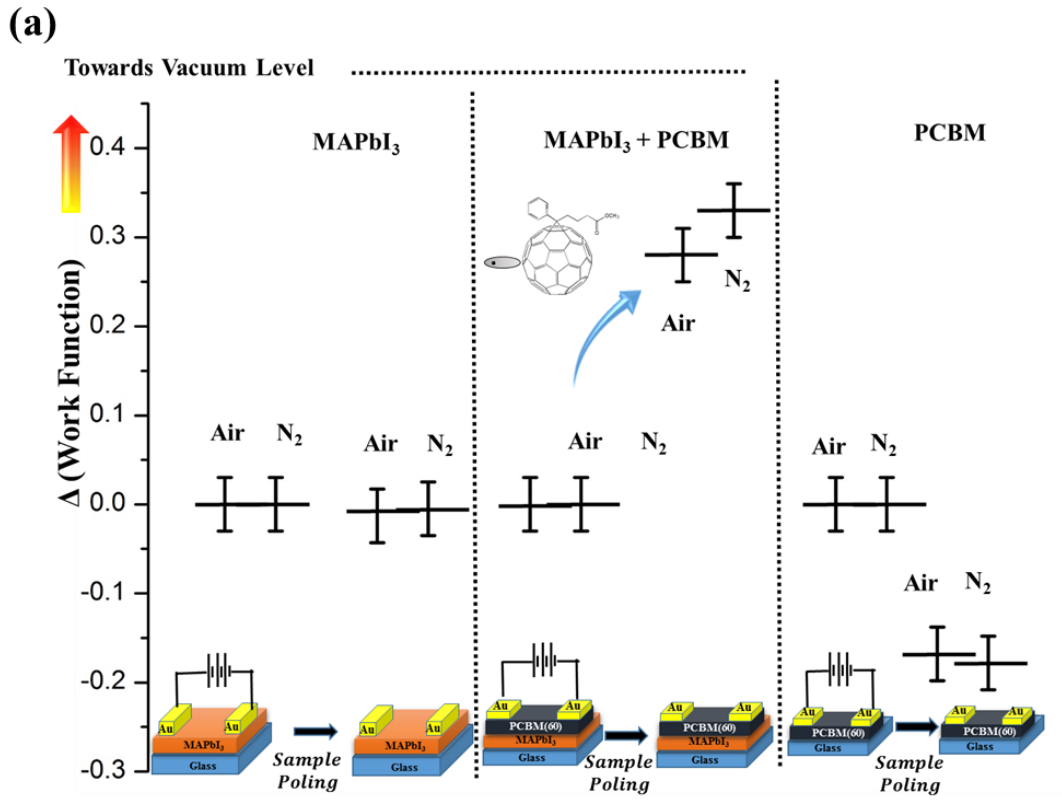

Figure 4-3 (a) Change in work-function after poling the samples is shown. The values of work function before poling are normalized to zero while the change in work-function after poling is plotted w.r.t. the pre-poled samples. The PCBM work function on perovskite decreases after poling while that of pristine PCBM increases

To understand how the PCBM ionic doping affects the interfacial electronic properties of the cell as whole, Kelvin Probe Microscopy (KPM) measurements are performed to track the changing interfacial energetics with doping **Figure 4-3**. Since poling the samples is necessary for inducing a reaction, changes in the work function (W.F.) after poling are plotted for all samples (Δ(W.F.) = W.F. $_{before\ poling}$ – W.F. $_{after\ poling}$). The reference perovskite remains quite stable with poling **Figure 4-3**. Pristine PCBM becomes more p-type (increase in work-function hence Δ is negative) after poling presumably due to oxygen or creation of trap states in PCBM (ref). For the PCBM on top of perovskite, a significant (~ 0.3ev) decrease in the work-function (Δ is positive) after poling is observed. This gives evidence of an n-type doping occurring of

the PCBM due to the interaction occurring between the moving I^- and PCBM in solid state. In order to discard the possibility of any dipole effect in the kelvin probe measurements: changes in the W.F. of a thick metal (reduce the pillow effect) is tracked which is in direct contact with PCBM *Figure 4-4*. For this a third Au electrode is coated between the two poling electrodes which in direct contact with the PCBM-Perovskite bi-layer and we track the work function changes of the metal after poling**.** We find similar changes where the work-function of the central Au on top of PCBM decreases by 0.3ev. This reaffirms the n-type doping of PCBM in solid state after poling the perovskite beneath which can be attributed to the interaction between I^- and the PCBM.

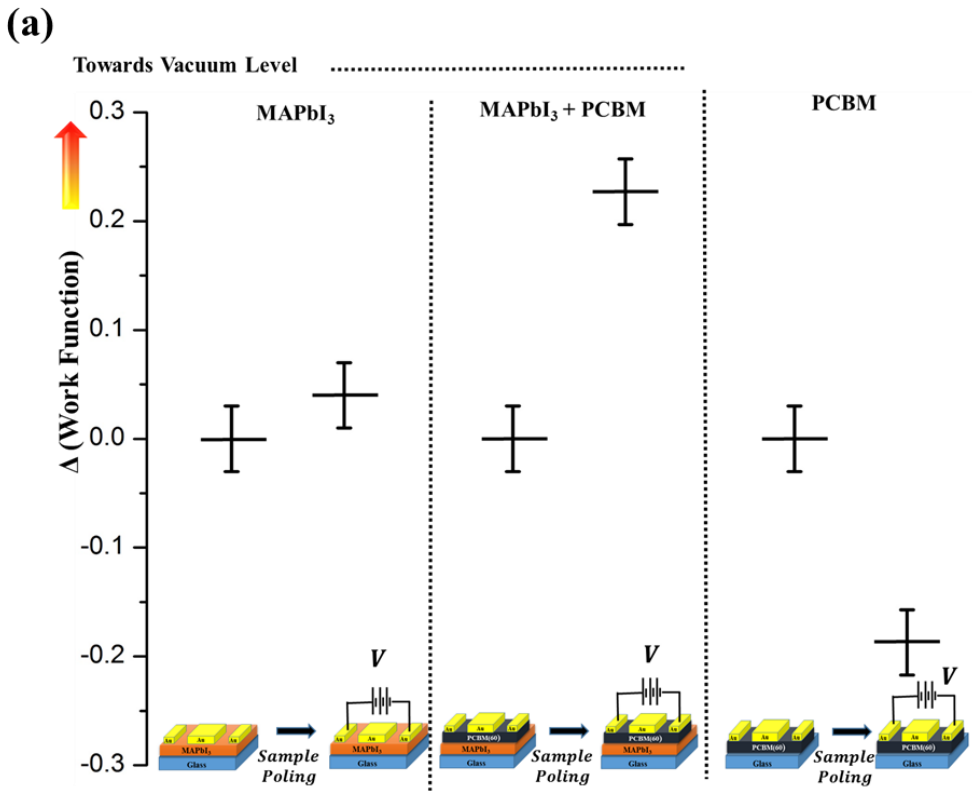

Figure 4-4(b) Changing Work-Function of the Contacts (Au here) before and after poling in light/N_2 conditions.

An important consequence of this is, in a working perovskite solar cell with PCBM as the EEL, the fermi level of the n-type extraction layer gradually moves towards the vacuum level due to an active doping of the interlayer. Hence an active increase in the built-in potential can be

expected in the cells with a PCBM interface. Preliminary evidence of this is observed by comparing the Dark-IV of the two devices used in Chapter 3, before and light soaking (before and after accumulating of ions within the device). They are shown in **Figure 4-5**. Considering a standard Schottky junction for moderately doped semiconductors or even p-i-n systems, the dark current is given as[47] $J=(A^{**})\times T^2\times\exp(-q\,\varphi_{Bn}/kt)\times\exp(q(\Delta\varphi+V)/kT)$ and the interfacial barrier can be written as $\varphi_{Bn} = (kt/q) \times \ln(A^{**})T^2/J_0)$ where all symbols have their usual

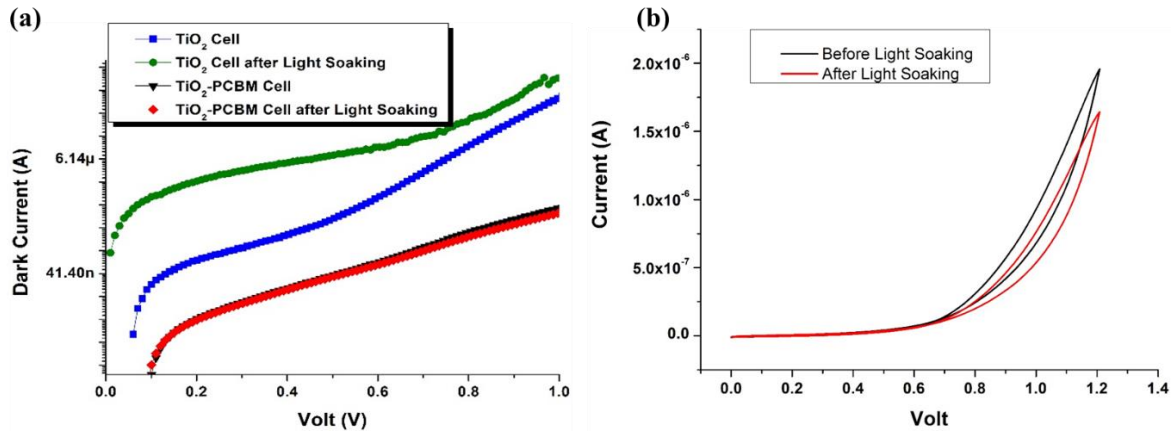

Figure 4-5 Dark I-V before and after light soaking for the two types of interfaces are shown

meaning. After light soaking, we find the injection barrier for TiO_2 interfaces significantly decreases and φ_{Bn} goes from 0.82V to 0.72V. While for the PCBM-Perovskite interface the injection barrier follows an exactly opposite trend where φ_{Bn} increases from 0.84V to 0.89V with light soaking. Though these values do not quantitatively represent the perovskite /n-type layer interface (it's a combination of the electron and hole injection from the two contacts), the opposite trends in the change of the barrier values is a signature of the changes occurring at this interface. This is true since all the other interfaces but the EEL-$MAPbI_3$ in the two devices are same.

For the PCBM case Doping pushes the Fermi level up at the n-type contact with the perovskite creating a larger band bending at the interface increasing the injection barrier and the built-in

potential. For the TiO_2 cells, the origin of the decreased barrier after light soaking is yet however unresolved and can possibly arise from multiple effects : the n-doping of the perovskite interface by I^-, or by image charges Schottky barrier change, or by one of the trap based injection of charges.

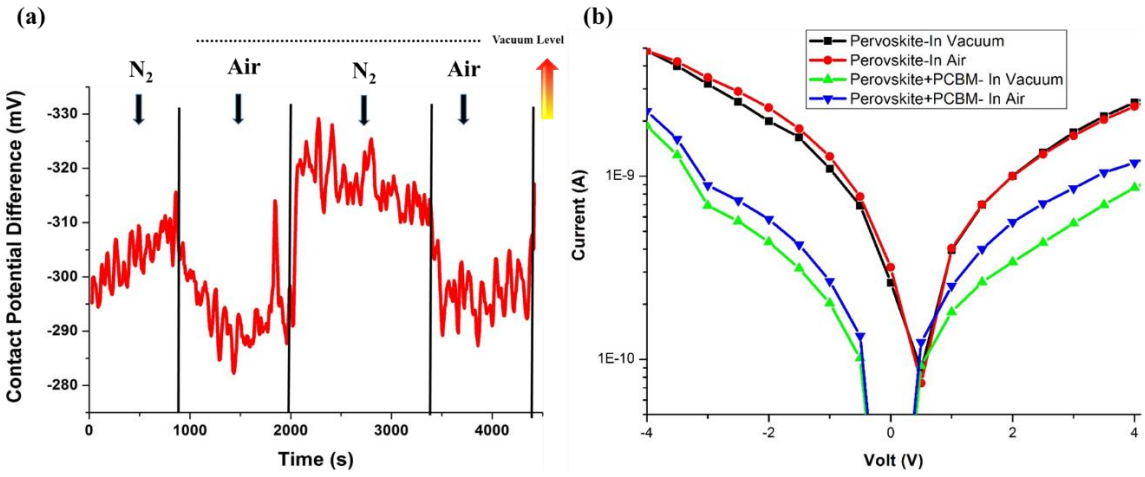

Figure 4-6 Dark I-V of only Perovskite and Perovskite coated with PCBM. While the Perovskite response is the same in both Air and N_2, the Pervoskite with PCBM consistently shows higher current in the presence of Air showing higher passivation in Air by PCBM.

Lastly the stability of our kelvin probe measurements is air and N_2 is taken. Here it is speculated that an active doping/de-doping of the ion doped PCBM occurs when it is cycled between N_2 and air **Figure 4-6a**. The de-doping in air occurs presumably by the oxygen triplet state which oxidises the doped PCBM. Cycling the doped PCBM in N_2 and air, a decrease and increase in W.F. is found respectively and propose the following 2-step reaction to occur:

$I^- + PCBM \rightarrow PCBM^- + I\ (Interstitial)$ in Nitrogen

$PCBM^- + O_2 \rightarrow PCBM + O_2^-$ in Air

The de-doping in principle can create a larger availability of PCBM to be doped by an accumulating iodide ion. Another evidence of this is seen in **Figure 4-6b** from the Dark-IV

scans in vacuum/N_2 and in air, where larger passivation as well as lower φ_{Bn} of perovskite is observed in air.

4.4 Effects on Interfacial Energetics, Device Stability and Discussion

We now summarize all our observations in view of the Chapter 3. Solid state reaction between the accumulated I^- and PCBM is highly likely to occur in the $MAPbI_3$ solar cells in solid state. In the presence of a reference TiO_2 EEL such a reaction is unlikely to occur. Since it was seen in chapter 3 that transport/recombination of charges is heavily affected by this EEL interface, it is worth understanding what role does the accumulating I^- play in the interfacial energetics.

A seminal report on calculating the defect formation energies, defect state energies (positively charged, neutral, and negatively charged) is shown by Du et.al.[51] **Figure 4-7** shows transition levels for the commonly affecting defects in $MAPbI_3$ perovskites. The values in the parenthesis (q,q') represent the state of the charge of the defects. For example for and Iodide interstitial (I_i) defect, q=0 represents a neutral defect, q=+1 represents a positively charged defect, q= -1 is a negatively charged defect, all of them being Iodide interstitial (I_i) defects in the crystal: And they are represented by I_i^0 I_i^+ I_i^- respectively. The charge transition level ε(q,q') for a defect type is determined by the Fermi-level at which the formation energies of the defect with charges q and q' are equal to each other. ε(q,q') can be calculated by:

$$\varepsilon(q/q') = \frac{E_{D,q'} - E_{D,q}}{q - q'}$$

Where $E_{D,q}$ ($E_{D,q'}$) are the total energy of the supercell used for calculations.

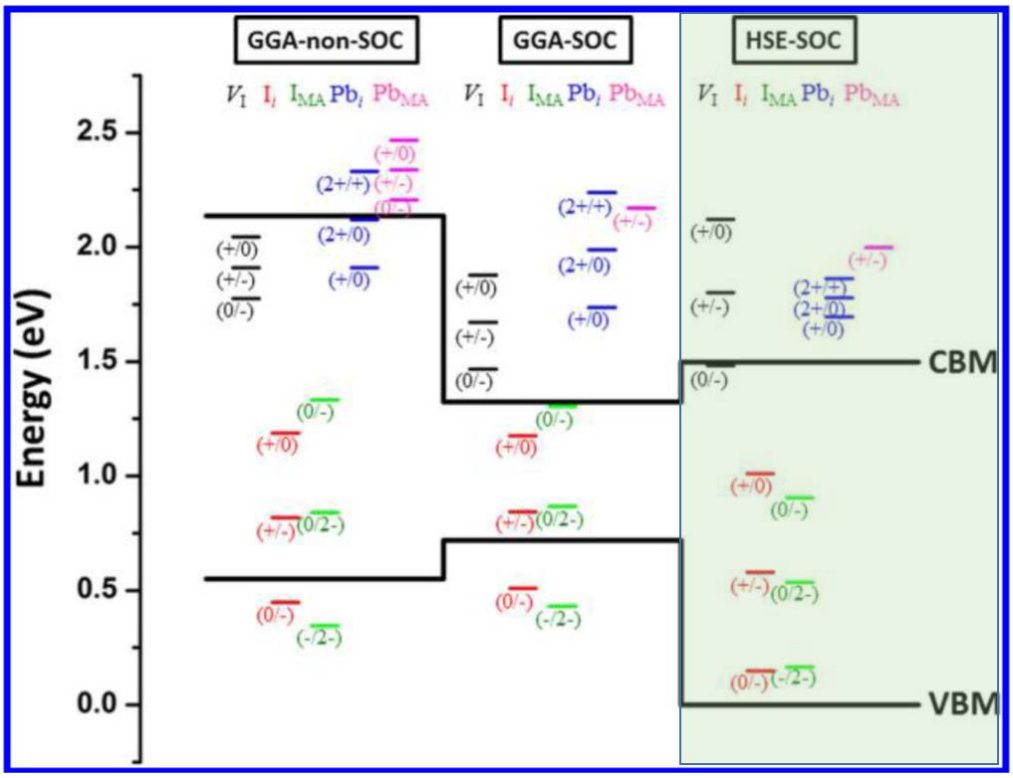

Figure 4-7 First Principles Calculation (DFT) calculating the defect levels in $MAPbI_3$ Perovskites. The HSE-SOC calculations are accurate due to the inclusion of the spin-orbit coupling.

Special interest to us is the Iodide interstitials and the vacancy of MA^+ that accumulate at the EEL. Since the formation energies of the MA vacancies are much larger and so is their activation energies for ionic motion, we focus on the more probabilistic case of I^- interstitials. For the I^- interstitial the (+/0) level is much higher than the (0/-) level : This shows that the defect trapping an electron would require a much larger crystal lattice relaxation (larger number/higher energies of lattice phonons) than trapping a hole. In other words it is much more probabilistic for I^- interstitial defects to trap holes than electrons from energetic considerations. The (+/-) level determines the charge transition between the two stable charge states of +1 and -1. The (+/0) level is the electron trapping level for the I_i^+ while the (0/-) level is for the hole trapping of the I_i^- . The Fermi-Levels in $MAPbI_3$ have been observed to be near the Mid-Gap or towards the Conduction Band. Under these conditions I_i^- are stable and their acceptor level is about 0.15ev above the VBM. It must be kept in mind that though these levels are thermodynamic hole trapping levels of I_i^- which are inside the band-gap and not their single-

particle levels (a result of which is that these states cannot be excited by sub band-gap excitations or seen easily by optical measurements). However their effects can be seen in electrical and other opto-electronic measurements. A defect level at 0.16ev above the VBM was recently observed using admittance spectroscopy for example (ref).

It is quite intuitive to expect negatively charged I^- interstitials to trap holes at the interface. First principle studies confirm this, and we can expect an accumulation of hole traps upon the accumulation of I^- ions at the EEL interface in our devices.

We now summarize the key findings of Chapter 3/4 . From dark IS, large capacitances at low frequencies for TiO_2-$MAPbI_3$ devices are found which is supressed in the presence of PCBM at the interface. A direct correlation between the injected dark current and the low frequency giant capacitance in the TiO_2-$MAPbI_3$ devices is seen indicating a large electronic charge carrier accumulation at the TiO_2-$MAPbI_3$ interface. From TPI/V a concomitant increase in trapping of electronic charges and the formation of a secondary pathway for recombination is observed at the interface. Finally all these processes evolve in time under light soaking which suggest towards a slow accumulation of trap states at this interface. This accumulation of interfacial trap states may be at the origin of large capacitances observed in the dark in the TiO_2-$MAPbI_3$ devices. We have seen that interstitial I^- ions create charged defect states close to the VBM ((0/-)) which act as shallow hole traps. Hence an accumulation of I^- defects at the TiO_2 interface would create a large population of hole traps at this interface increasing the interfacial defect states. Such formation of large capacitances, interfacial traps and electronic charging is not present in the PCBM devices, which is consistent with the absence of large capacitances in these devices.

The evolving interfacial dynamics is summarized in **Figure 4-8**. We first look at the TiO_2-$MAPbI_3$ devices. The built-in potential must already provide an initial concentration of Iodide

ions at the electron extraction (n-) interface (ref). Under light soaking of 1 Sun this accumulation of iodide ions is expected to aggravate and change the interfacial energetics. For simplicity we do not consider the contribution of the compensating field created by the accumulated ions here. Firstly, there is a lack of consensus in the measured built-in across the perovskite bulk due to the band-bending at the TiO_2-PVK interface[62,6349]. Few reports suggest a n-i-p type (n-EEL, i-$MAPbI_3$, p-Spiro-OMeTAD) structure for $MAPbI_3$ solar cells while others have reported a n-p type (n-EEL, p-$MAPbI_3$) behaviour. When we observe a continuous creation of interfacial defect states in time at the TiO_2-$MAPbI_3$ interface, it should then create a gradual drift from an n-i-p type structure to a n-p type configuration of the device (**Figure 4-8a,c**). Upon fermi-level normalization, a large portion of the injected charges are bound at these interface states (D_{it})/(N_A) creating a larger drop in the built-in potential across that interface and a smaller drop across the bulk. Possibility of a pinned Fermi level should not be ruled out in this state of the semi-conductor. Here we denote N_A acceptor states discussed above along with possible creation of single level interface states (D_{it}) created by I^- interstitials for the sake of completeness.

Shown in **Figure 4-8d** is the generation of free charge carrier in the device under light and dark. In dark, upon injection of a dark current (electrons/holes) we start filling the defect states at the TiO_2-$MAPbI_3$ interface with holes, plausibly creating higher number density of charged defect states. The direct correlation of the dark capacitance with the dark current I as $C \alpha I^{0.96}$ (Chapter 3) indicates that the electronic charge contribution dominates the formation of a double layer at this interface. This filling creates a large interfacial double-layer that provides a large field directly proportional to the trapped holes. This field causes an increased band bending at the interface which is proportional to both the density of traps and injected current. Isaac et.al[33]. hypothesized the formation of accumulation zones of holes forming at this interface from C-V measurements. Here we suggest that the field required to set up an

accumulation zone in the perovskite may be created by the injected holes that are trapped at the interface. The origin of why this capacitance has such low resonant frequencies needs to be explored further. The actual nature of the polarons created by the interfacial accumulation of I^- defects need to be explored further by ab-initio studies [64,65].

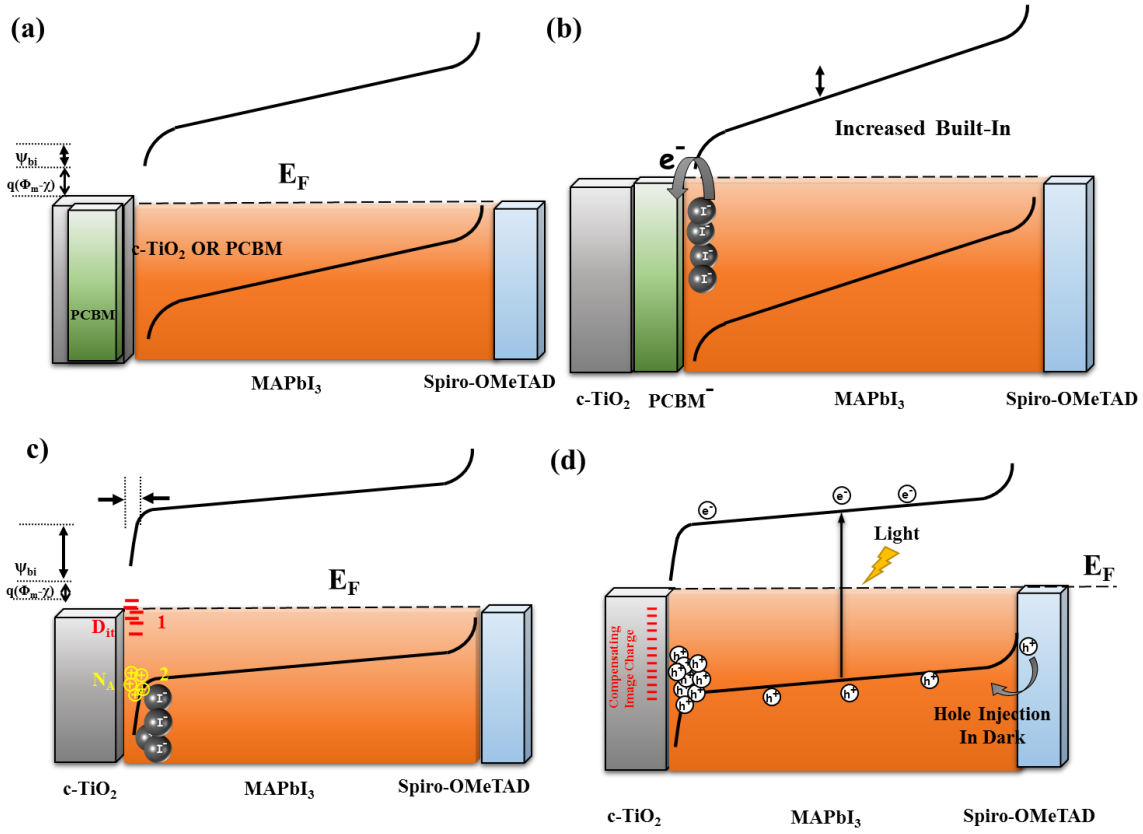

Figure 4-8 Band Diagrams for (a) Both types of cells in a fresh state before ionic accumulation where all symbols have their standard meaning. (b) With a PCBM interface which gets doped by the iodide ions resulting in fewer interface states and an increased built-in potential (c) With a TiO_2 interface where the iodide ions can form interface states (1) or charged defects (2) giving rise to a large drop of the built-in potential across the interface rather than the bulk. (d) The trapping of holes at the TiO_2 interface is shown. In dark the source of the trapped charge carriers are the injected dark current, in light it is the light generated free hole population

Interestingly under light, the rate and amount of accumulated interfacial charges depends on the free charge carrier density available within the film. Even at low light intensities one observes a large increase in the low frequency capacitance which can be attributed to the generation and trapping of light generated holes. Regarding transport and recombination observed from TPI/V, presence of defect states is bound to increase the non-radiative recombination as well as increase the trapping based transport of charges.

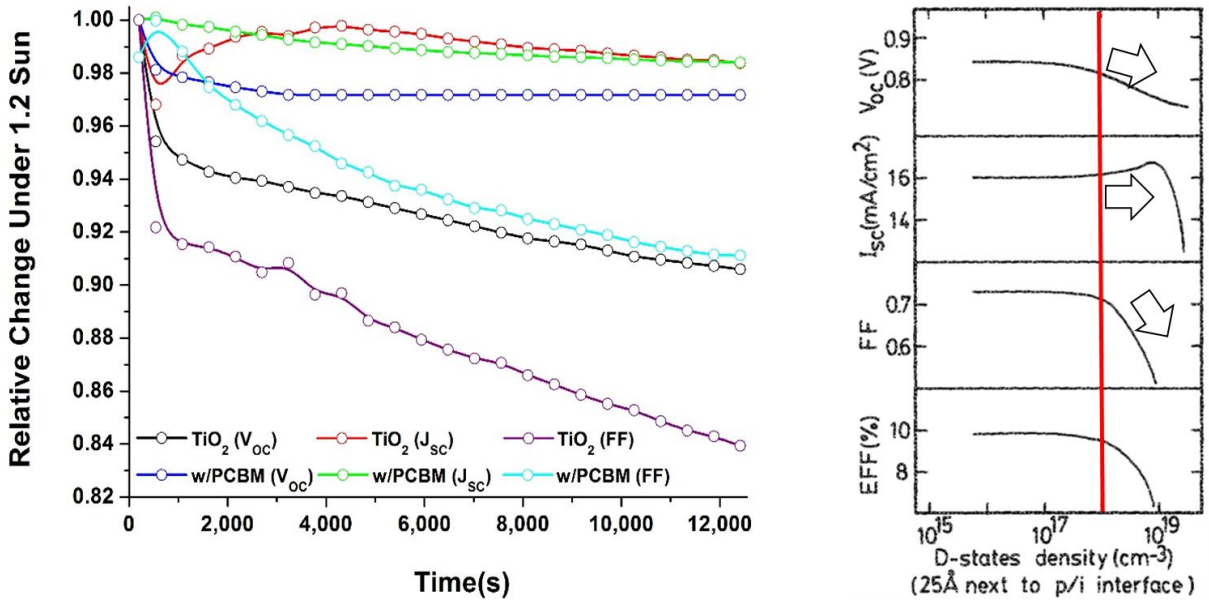

Figure 4-9 (a) Performance stability of the two types of devices where devices without PCBM show characteristics of devices with increasing interfacial states in time.(b) Changing performance of a silicon p-i-n solar cells with increasing interface defect densities[66]

In case of devices with a PCBM EEL **Figure 4-8b**, the accumulated I^- are passivated by the PCBM through a solid state chemical reaction. The absence of the large capacitances, electronic charging, trapped transport and larger recombination is consistent with the scenario of accumulating I^- ions undergoing a solid state reaction with the PCBM EEL. There is a good probability that the solid state reaction between I^- and PCBM passivate the interstitial I^- defects states which cause the interfacial charging in the TiO_2 devices. A possibility of diffusion of I^- into the PCBM EEL has also been suggested. A I^--PCBM charge complex formation may then be at the origin of passivation of electronic traps and accumulated electronic charges observed in $MAPbI_3$ perovskite solar cells.

A detailed ab-initio study is required to model the formation energies and transition energies of defects in $MAPbI_3$ perovskites in the presence of an I^--PCBM charge transfer complex. This would elucidate the exact nature of interfacial defect passivation by PCBM and would be interesting to study its effect on the I_i^- (0/-) defect state.

Finally the role of accumulating interfacial defect states on the working stability of the solar cells is shown in *Figure 4-9* under light continuous soaking of 1.2 Sun. For the TiO_2 cells a stable Short-Circuit current(J_{sc}) is seen while the Open Circuit Voltage(V_{oc}) and the Fill Factor (FF) of the device fall in time. The FF falls much more rapidly in time w.r.t. the V_{oc}. This is a classic representation of an increasing density of interfacial states [66] where D primarily affects the V_{oc} and FF in p-i-n solar cells (**Figure 4-9b**) (ref). **Figure 4-9b** shows for a standard p-i-n solar cell, the effect of increasing interface defect densities on the J_{sc},V_{oc} and FF of solar cells. The stable Jsc and decreasing FF and V_{oc} for the TiO_2 cells points towards our hypothesis of accumulating interfacial defects. The cells with PCBM EEL retain a stable Voc and Jsc with a slower drop in only the FF of the cells. The stability of the V_{oc} of these cells in comparison to the TiO_2 cells shows we avoid the formation of interfacial defect states in PCBM cells. Hence controlling interfacial defect accumulation is crucial to enhance the stability of these solar cells.

4.5 Overview and Future Outlook

In dark, the giant capacitance at low frequencies, the large charge accumulation and the slowly changing electrical response of $MAPbI_3$ cells can be attributed to accumulation and charging of interfacial defect states trapping holes. These defect states are most likely caused by the accumulating I^- interstitials at the interface. These states affect the built-in potential across the bulk perovskite regulating the recombination and transport dynamics of charges which finally decreases the working stability of these solar cells. A novel way to overcome these problems is to passivate the accumulating ions at the EEL interface. We suggest that using a dopable contact like PCBM can passivate all the above by acting like a sponge that chemically reacts with the accumulating iodide ions at the interface in solid state and thereby forming charge transfer complexes. This may prevent the formation of accumulating defect states at the

interface and thereby achieve a better working stability of these cells. The exact nature of passivation is yet to be uncovered through first principles modelling. A detailed first principles understanding would assist us in developing other interfacial materials that can passivate such defects caused by interfacial accumulation of ions. Hence learning from PCBM, we propose a new strategy of employing chemically engineered dopable interlayers capable of reacting with accumulated ions and vacancies at the interface to improve the working stability of perovskite solar cells.

5 Efficient $MAPbI_3$ Photoconductors through Selective Hole Circulation

5.1. Introduction:

One of the key advantages in solution processable semiconductors is making them printable on a large scale with Roll-to-Roll printing, slot-die coating, gravure coating, imprint printing and others[67–77]. There are few key challenges that have traditionally plagued solution processable semiconductors: they usually have low mobilities and are heavily trap limited. $MAPbI_3$ perovskites processed from solution have shown very large diffusion lengths of electrons/holes (Micro-meters > Device thickness), shown efficient band-type transport characteristics and also show high mobilities from Hall-Effect (>10 cm^2/V-sec) and field-effect transistor measurements (~ 1 cm^2/V-sec)[6,9,78,79]. Large absorption coefficients of ~$10^4 cm^{-1}$ with a tuneable band-gap are also exhibited. This makes $MAPbI_3$ extremely promising to achieve opto-electronic performances similar and better than polycrystalline silicon while all the time being fabricated through solution processable methods transferrable to high throughput printing. While the main focus has been placed by researchers on pushing the limit of solar cell efficiencies, many other areas where perovskites can also carve out a space for themselves has been comparatively overlooked. One such field of application is the use of mixed halide perovskite semiconductors in the application of light detection – as photoconductors (PCs) and photodetectors (PDs)[67–77,80–91]. Initial reports on $MAbI_3$ PDs show promising responsivities and comparatively low noise[71]. Recent performance of $MAPbI_3$ PDs better few commercially

available Si-PDs [72], show capability of detecting wavelengths in very narrow bandwidths (ref), detect X-Rays and γ-Rays [68] and also show lower noise compared to Si detectors. Ways forward in improving the performance of Perovskite detectors involves increasing their stability, decreasing the noise further, large area printing while maintaining high performances. Towards this end, in this chapter a printable $MAPbI_3$ PC is presented which demonstrates state of the art performance for Perovskite PCs. Rationalization of the high performance and is given in terms of band-engineering and trap passivation.

5.2. Materials Characterization: Fabrication, SEM, ,XRD,UV-Vis

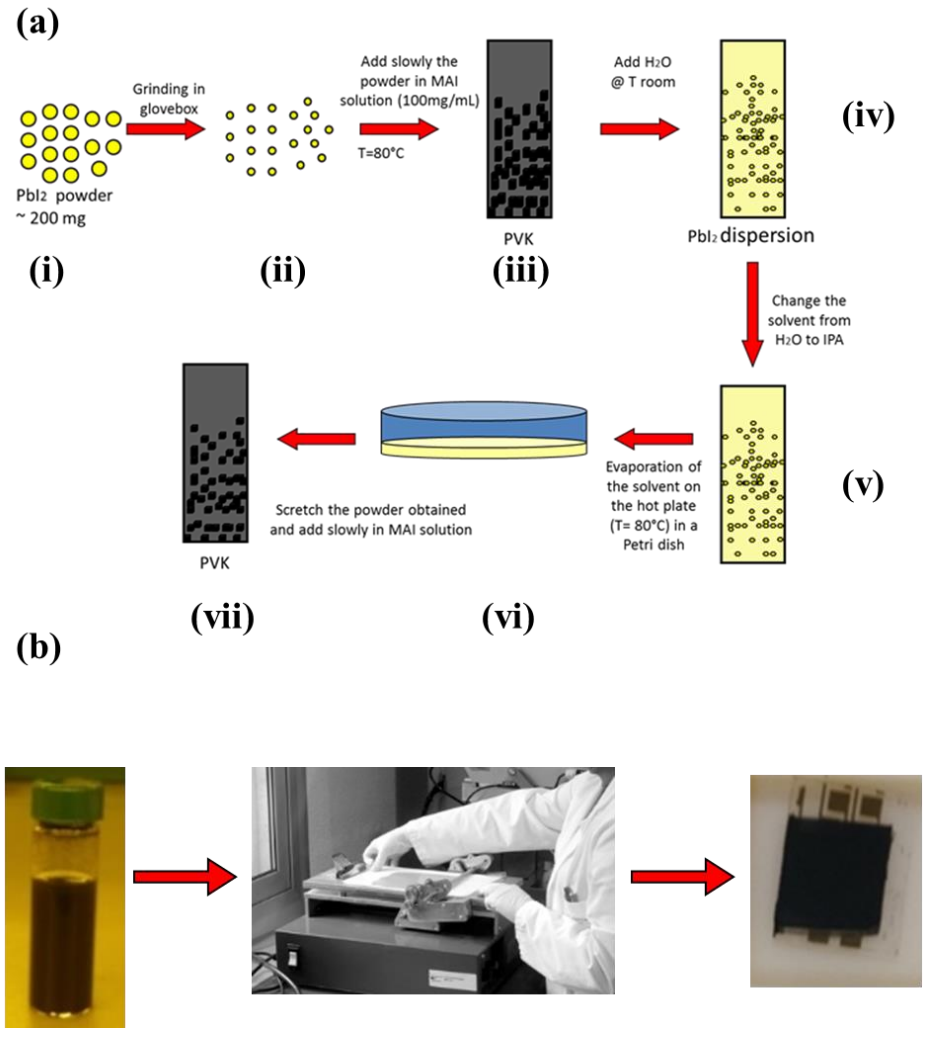

Figure 5-1 : a) Schematic of the synthesis of Printable Perovskite Particles (PPP) is shown. b) The PPP-ink is shown which is then bar-coated on pre-patterned electrodes to obtain uniform few micron thick PPP films.

Printing remains a golden standard for manufacturing large area sensors and detectors. However one of the persistent problem that needs addressing is the solvents used themselves; usually physically carcinogenic, corrosive and environmentally hazardous solvents like chlorobenzene and its derivatives, Dimethyl Formamide, Dimethyl Sulfoxide, Acetone, Toluene and others are used. To circumvent this, my colleagues Roberto Sorrentino and Peter Topolovsek have synthesized $MAPbI_3$ sub-micron to micron sized particles which is briefly described.

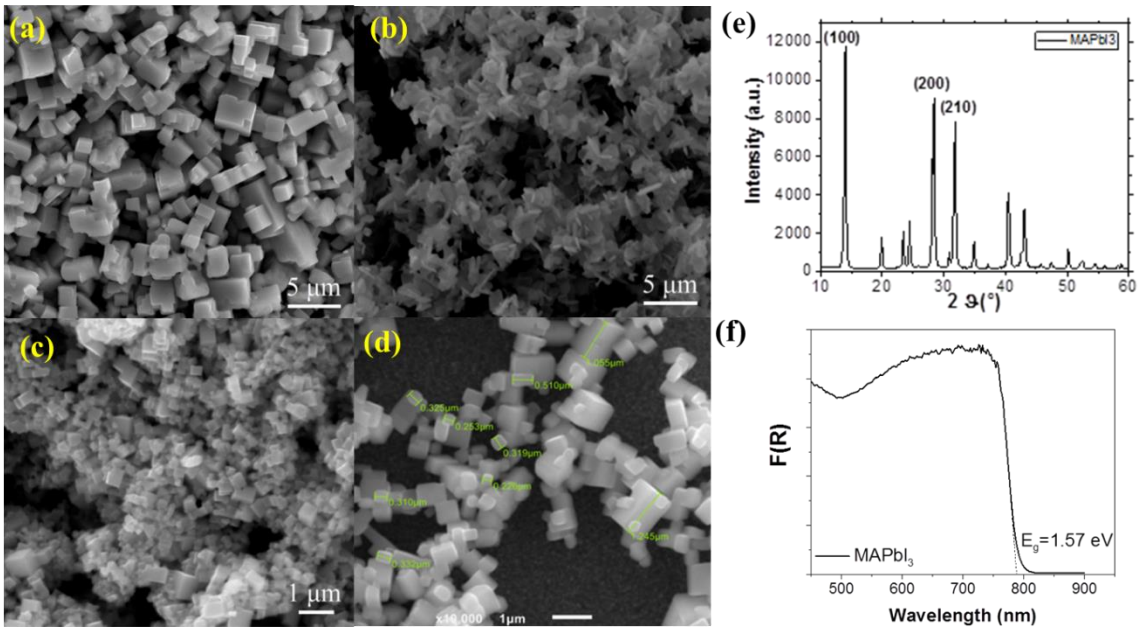

Figure 5-2 SEM images of a) Perovskite particles using physically grinded PbI_2 as precursors b) Re-crystallized PbI_2 hexagonal particles from solution c),d) PPP particles with sub-micron sizes e) X-ray Diffraction spectra of the PPP particles and f) Absorption spectra in the Reflection mode of the PPP particles is shown using the Kubelka-Munk method.

From **Figure 5-1a**, PbI_2 particles are initially grinded physically to obtain smaller and uniform PbI_2 particles (for obtain full conversion into $MAPbI_3$). They are then added to a solution of MAI in an alcohol based benign solvent of IPA to finally obtain $MAPbI_3$ particles (**Figure 5-2a**). The next step involves recrystallizing PbI_2 into sub-micron particles by slowly adding H_2O to the perovskite solution which dissolves the MAI. After solvent exchanging into IPA the precipitated PbI_2 is left to settle in the bottom and IPA is made to evaporate. The SEM of

the leftover PbI_2 particles are shown in **Figure 5-2b** -which are of a much smaller dimension. Finally these smaller sized PbI_2 particles are converted into $MAPbI_3$ particles by slowly adding them into an MAI solution in IPA. The finally obtained $MAPbI_3$ particles are in a dispersion form in IPA, and their SEM is shown in **Figure 5-2c** and **Figure 5-2d**. Sub-micron $MAPbI_3$ particles with a now acceptable size distribution are obtained which can be printed. Figure 5-1b shows the solution of the final dispersion of $MAPbI_3$ particles in IPA, which is then bar-coated on glass substrates with pre-patterned electrodes. X-Ray diffraction studies of the $MAPbI_3$ particles is shown in **Figure 5-2e**, where a complete conversion into $MAPbI_3$ is found with no residuals of leftover unreacted PbI_2 (at~12^o). **Figure 5-2f** shows the absorption spectrum of the Printed Perovskite Particles (PPP) measured from the reflectance mode using the Kubelka-Munk method which is that of a standard $MAPbI_3$ perovskite.

5.3. Device Performances: I-V, Responsivity, Gain, Noise Measurements, Specific Detectivity, Dynamic Range and Temporal Response

PCs devices structure as shown in **Figure 5-3**. The PPP are formed on interdigitated electrodes of Cr-Gold (Au) with a channel length of 5 micrometers and length 10mm. A layer, either an electron extraction layer PCBM or hole extraction layer Spiro-OMeTAD is spin coated on the on top of the Perovskite. A standard 2-step perovskite as a 'Reference' is also made where first a PbI_2 precursor is spin coated on the electrodes and then converted to $MAPbI_3$ by spinning a solution of MAI on top (See Experimental Chapter 2).

First the plot of dark currents in the device and their light response is shown in **Figure 5-4**. For this a Green LED (532nm ~$10mW/cm^2$) is used. The dark and light I-V are ohmic and there is no evidence for a Schottky barrier in dark or light. However caution is required before it is assumed that the contact to be ohmic for both or electrons and holes in the device.

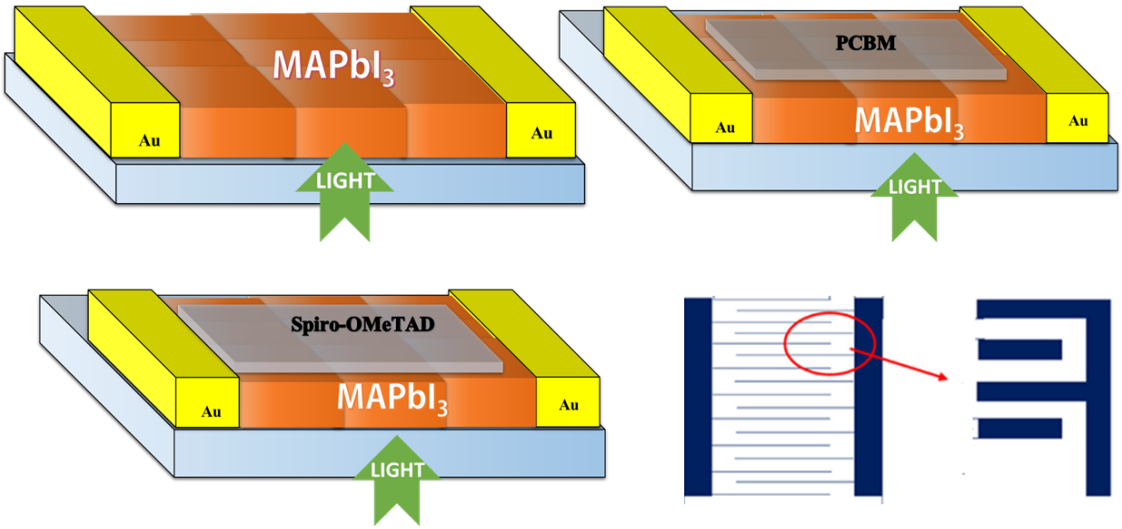

Figure 5-3 Schematic of the PCs used in this chapter are depicted where $MAPbI_3$ PPP semiconductors are placed between two Au electrodes. The last schematic is of the electrode geometry used in the study is shown which are interdigitated electrodes with a 5 micrometer distance between two electrodes.

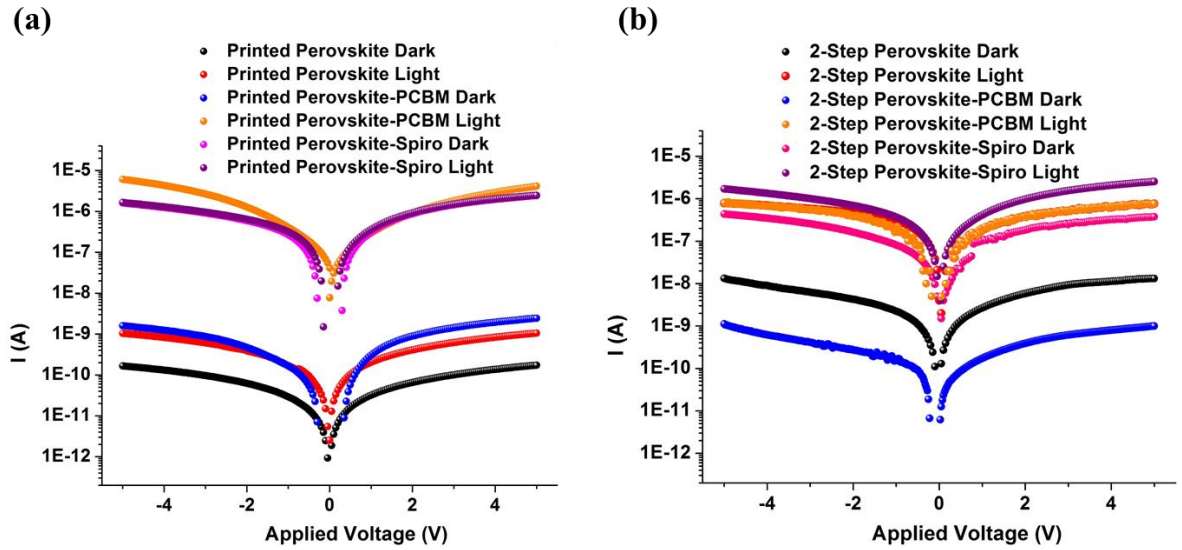

Figure 5-4 Dark and Light I-V for a) PPP and b) Reference 2-Step Perovskites as pristine, with PCBM and then Spiro-OMeTAD layer at the top. A 525nm light with intensity of 10mW/cm^2 is used as the light excitation source

A striking observation is the low photocurrent gain found in the Spiro-OMeTAD devices. It must be mentioned that at moderate and lower (<1mW/cm^2) light intensities the change in current with light is not observed with a Spiro-OMeTAD layer on top of perovskite. Hence in the spectral measurements (in wavelength), devices with Spiro-OMeTAD are not shown. Another point to note is an increase in the On/Off ratio of devices with a PCBM layer on top.

Much larger photocurrents and gain are found by coating PCBM on top of both perovskites : Reference and PPP.

Reported here are the basic parameters, the details of which can also be found in other text books[92] and is briefly described here. The Responsivity (R) which is given by:

$$R = \frac{J_{ph}}{P_s}$$

where J_{ph} is the photocurrent density in the device and P_s is the incident optical power on the photoconductor. Gain in the samples is the amplification in the device current due to the incident light and can be written as:

$$Gain = \frac{Number\ of\ collected\ elecronic\ charges}{Number\ of\ Incident\ Photons} = \frac{J_{ph}/e}{P_S/hv} = \frac{\tau_{Rec}}{t_{transit}}$$

where τ_{Rec} is the recombination lifetime of the excess carriers in the semi-conductor that is generated by light and $t_{transit}$ is the transit lifetime of the faster moving carriers (e^-/h^+) in the film. Gain can be simply understood as follows : Suppose electrons travel faster than holes in a semi-conductor for a given recombination lifetime. As the electron and hole are transported to opposite sides of the photoconductor due to the applied bias, the electrons complete their trip sooner than holes. The requirement of current continuity forces the external circuit to provide more electrons into the circuit as flowing current. These new electrons move again more quickly again completing their trip before the holes reach their electrode. This process continues until either the electron recombine with the holes or the holes reach their respective electrode. A single photon absorption can therefore result in an electron passing through the external circuit many times. The expected number of trips that the electrons make before the process terminates is the gain for PCs.

Specific Detectivity of the PCs are given as D*. For this the Noise Equivalent Power (NEP) of the device is calculated. NEP is defined as the input power density of the optical signal for which the Signal/Noise ratio equals 1, i.e. SNR=1. NEP is given by

$$NEP^2 = \frac{\overline{i_n^2}}{R^2}$$

where i_n is the total noise current. From NEP we derive the Specific Detectivity D* as

$$D^* = \frac{(\mathrm{AB})^{0.5}}{\mathrm{NEP}}$$

where A is the device area and B is the bandwidth of measurement. It is to be noted that it is in this bandwidth that the noise has been measured and integrated to obtain the total noise current in the device.

A standard spectrophotometer to scan throughout the wavelength spectrum is used along with a slow I-V scan taken at each wavelength. Shown are only the characteristics for 5V for simplicity. For lower voltages lower Responsivities, Gain and Specific Detectivities are observed as expected. Beyond 5V the devices degrade and a lack of reproducibility is also observed. **Figure 5-5** shows the Responsivity of the devices.

As with the Light I-V measurements a large increase in the device responsivities is found by the addition of an electron acceptor PCBM on top of the both the reference and PPP perovskites. A much larger improvement in the Responsivity for the PPP than the reference samples is seen and values of 80 A/W are obtained, close to state of the art perovskite PCs[71,85,86,88]. Usually high responsivities such as this is obtained due to a large gain the PCs and can be seen in **Figure 5-6**. There is a dramatic increase in the gain, over two orders of magnitude in PPP PCs when coated with PCBM. This indicates either a large increase in τ_{Rec} or a large decrease in $t_{transit}$ or both. To calculate the specific detectivities, the NEP in terms of

the spectral density of the noise current (at 5V) is shown in **Figure 5-7**. PPP exhibits much larger noise than the reference devices and show a clear $1/f^{\alpha}$ noise over the whole range of measured frequencies which is usually a sign of electronic traps. PPP devices with PCBM show a marked decrease in the $1/f^{\alpha}$ noise at higher frequencies which gives evidence of a passivation of electronic traps by PCBM.

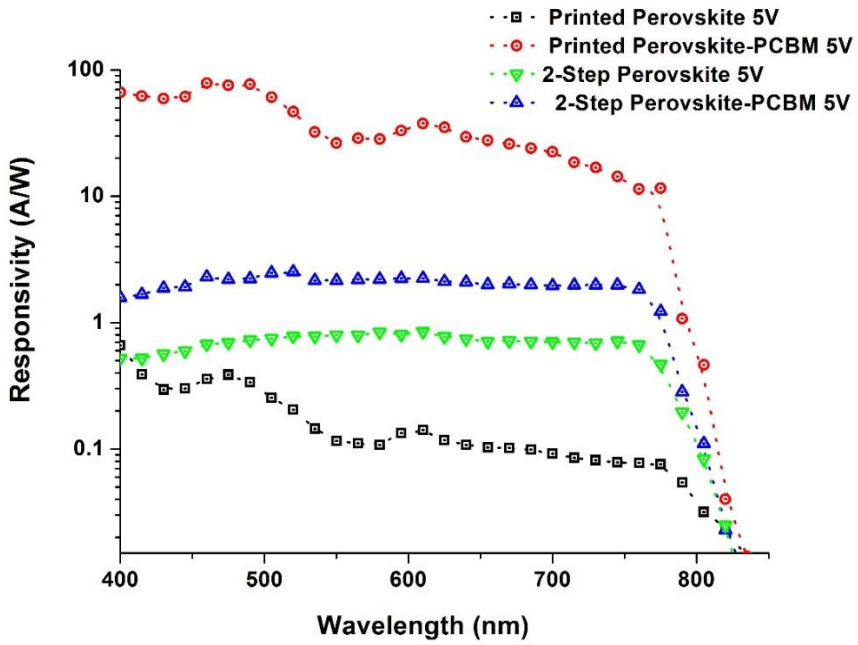

Figure 5-5 : Responsivity of all PCs are shown over the whole spectra (Input Power ~0.1µW-1µW)

In fact it is shown later that the high frequency noise for the PPP-PCBM case is close to the shot noise limit of the device that is the minimum theoretical limit that can be achieved. For the reference devices, much lower noise is found and is close to the theoretical shot noise limit.

The calculated D* is shown in **Figure 5-8**. Though responsivities and Gain for the PPP are higher than the reference devices, a much lower noise for the Reference devices yields a moderately higher Specific Detectivity value for the reference devices. In order to completely characterize the devices to better evaluate and understand the working of our PCs Intensity vs Photocurrent and transient photo-response measurements are performed. From Intensity Vs

Photocurrent measurements the Linear Dynamic range (LDR) is calculated, which is an important parameter for the photoconductor. LDR is defined as

$$LDR = 10 \log \left(\frac{P_S^{SAT}}{NEP} \right)$$

where P_S^{SAT} is the maximum power of the input light intensity until which the photocurrent is linear as a function of the input light intensity. As one approaches lower light intensities a linear dependency of photocurrent until the NEP of light (~pWatts) is assumed to obtain theoretical LDR numbers. We also present the measured LDR obtained using the lowest light intensity

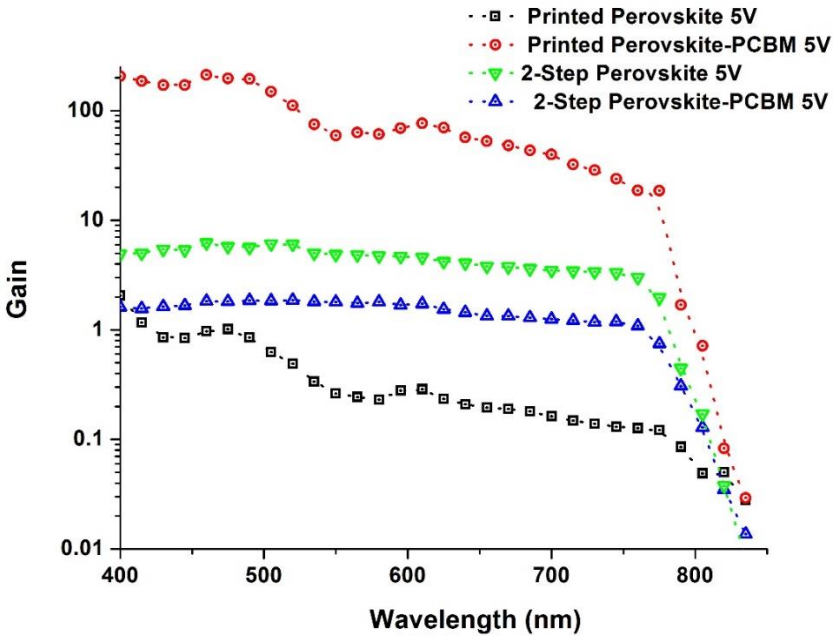

Figure 5-6 : Gain for all PCs are shown over the whole spectra (Input Power ~0.1µW-1µW)

that measured (which is an underestimation considering the limited capabilities to measure low light intensities). The importance of LDR is that indicates the range where the Responsivity (R) is linear with the Quantum Efficiency (η) of the device. The plot of Intensity Vs Photocurrent in shown **Figure 5-9** and the calculated LDRs are show in the table below. The first observation is that much larger P_S^{SAT} is obtained by applying PCBM on top of both PPP and the Reference Perovskites thereby obtaining much larger LDRs.

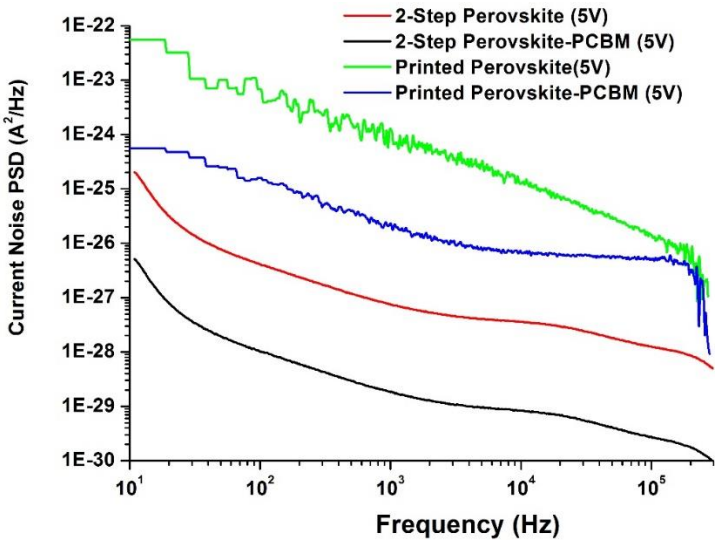

Figure 5-7 Current noise spectral density measured at 5V is shown

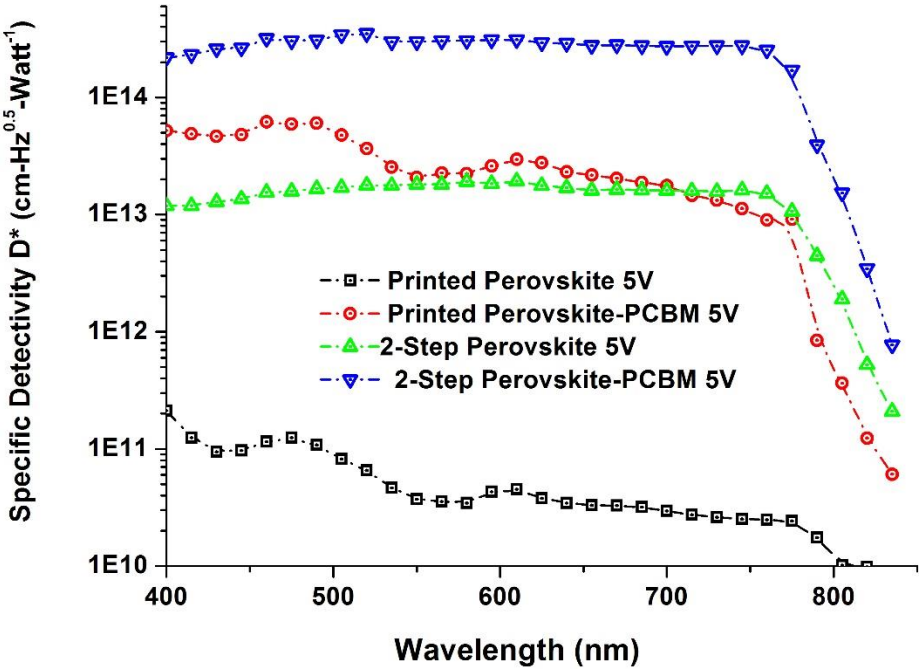

Figure 5-8 Specific Detectivity are shown for all PCs over the whole spectra (Input Power ~0.1µW-1µW)

Sample	Theoretical LDR	Measured LDR
PPP	87±3dB	27 ±3dB
PPP-PCBM	136±3dB	53±3dB
Reference (2-Step)	123±3dB	40±3dB
Reference-PCBM	141±3dB	53±3dB

It must be noted that the difference between the theoretical and measured LDRs are quite large. Since the NEP's in the devices are quite low (< pW/cm^2), it is a challenge to calibrate and reliably measure photocurrents at such low light intensities. The theoretically achievable LDRs are quite high and compare very favourable against GaN (50dB), InGaAs (66dB) and Si (120dB) photodetectors. In comparison to other PD's from $MAPbI_3$ the theoretical LDRs are the best achieved until date[71,72,80].

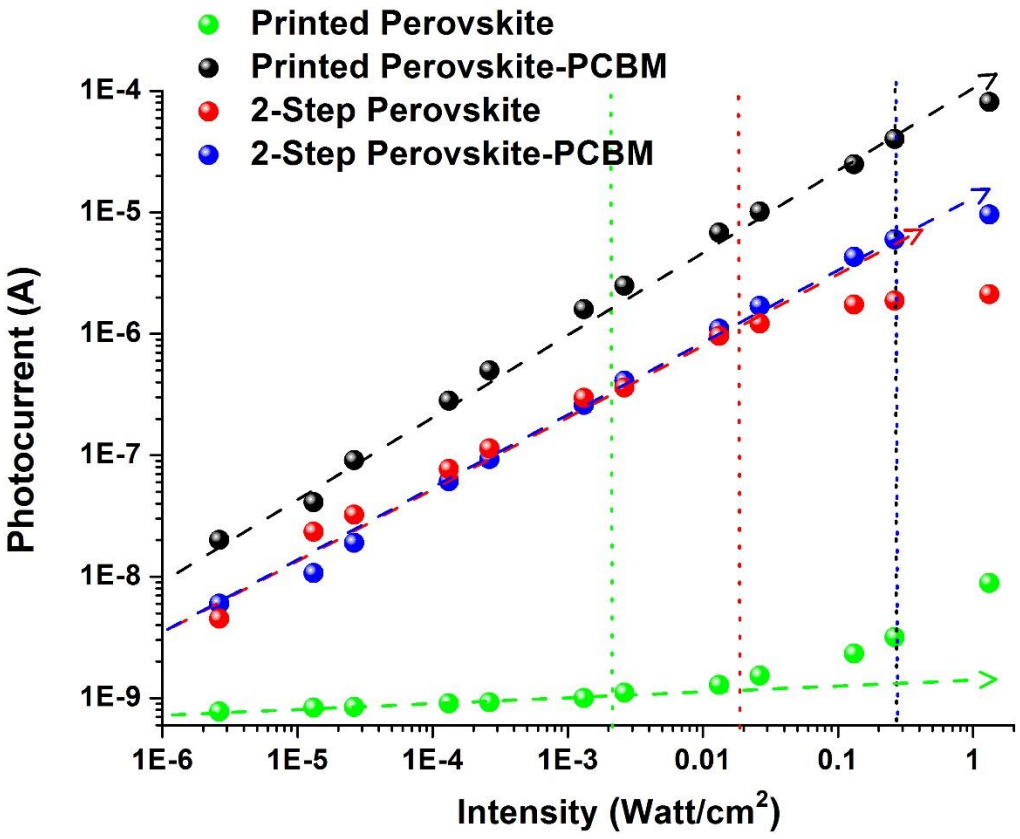

Figure 5-9 Light Intensity Vs Photocurrent is plotted for all PCs for LDR calculations. Dashed lines are P_S^{SAT}

Now proceed to look at transient light response (532nm LED 1mW/cm^2) of our devices and is shown in Figure 5-10. As is seen the transient response time of PPP greatly decreases from 60µs to 18µs due to PCBM which indicates much shorter transit times of charges after the PCBM coating. In case of Reference much faster transient responses (0.8µs) are found with little effect of PCBM. Only in case of Reference PCs did the Perovskite-Spiro show transient

photocurrents that could be measured. But this was achieved by using a minimum of 0.3 Sun light intensity (~ 30mW/cm^2) light source rather than the lower light intensities used earlier. The transient responses are very slow in the order of 60µs; two orders slower than Perovskite-PCBM. The consequence of such a slow transport will be discussed later.

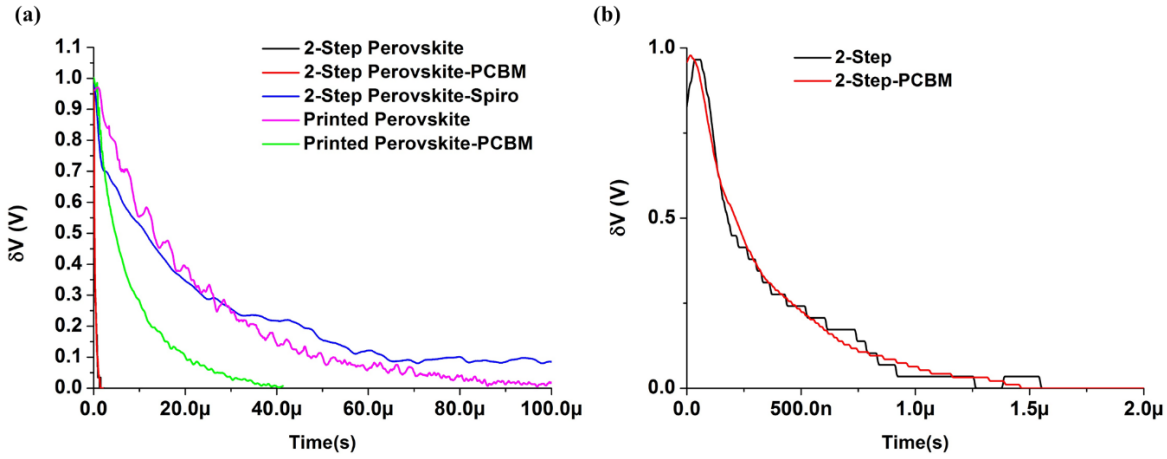

Figure 5-10 a) Shows transient photocurrent response of all PCs from a pulse of light b) Magnified image of the fast photo-response of Reference devices from panel a. Light source :532nm (1mW/cm^2) . However much higher light intensities (0.3 Sun White Light) had to be used to get any appreciable transient response from the Reference-Spiro device

The next section delves into understanding the good figure of merits of our devices. The role of PCBM/Spiro-OMeTAD on considerably enhancing/supressing the performance is also discussed.

5.4. Hole Only & Electron Only Device Mechanism: Injection/Trapping/Passivation?

Until date there have been only a few reports with $MAPbI_3$ PCs, with limited characterization and investigation of the working mechanism. The origin of large responsivities and large gains still remains unexplored. The effects of electron/hole accepting layers on $MAPbI_3$ PCs has not been investigated, the effects of which are quite drastic[81,85].

For selective charge injection (e^-/h^+) a photoconductor having electrodes with 2 different metals with varying work functions is fabricated. Au-Cr electrode contacts are fabricated on top of which a PPP photoconductor is printed. The work functions (φ) measured by Kelvin probe show our Au electrode to have φ- 5.15ev and Cr electrode to have φ-4.66ev which match well with literature values. Since these special interdigitated electrodes were fabricated on non-transparent silicon substrates, in these experiments the light is incident from the top side. Hence quantifying accurately the responsivities of the devices is challenging, since it would require measuring the exact 2-D profile of the absorption in our particle-film which is not trivial to estimate (it would require to measure the scattering cross-section of the particles, the 3-D size and position of the particles to take into account the void spaces in the particle type film).

The Dark and Light I-Vs with PPP on Au-Cr electrodes are plotted in **Figure 5-11**. It is convenient to plot all curves in one figure for comparison. From asymmetric I-Vs are observed for samples with PCBM/Spiro even in dark, when Cr is biased positive/negative w.r.t. Au. This points to the importance in understanding the interfacial band bending each of the interfaces. Many reports have measured the presence of the E_f for $MAPbI_3$ towards the Conduction band (CB) (4.0-4.2eV)rather than the Valence band (VB*)* or have found the E_f to be close to the mid-gap (~4.5eV)[93].. All the energy levels are shown in **Figure 5-12a**. Levels of the Au/Cr and E_f of PCBM have been measured which are consistent with literature and the value of Spiro is taken from literature. Under this scenario there is large Fermi level mismatch between Au and $MAPbI_3$ with a large band bending at this interface and a much smaller mismatch is with the Cr contact (See **Figure 5-12b**).

Now in case of PPP-PCBM/PPP-Spiro there is first a re-organization of the charge carrier densities between the two semi-conductors to thermalize into a new configuration. The final band diagrams are drawn with the electrodes by taking the semi-conductor bilayers (for eg:PPP-PCBM) as one unit. PCBM has an E_f around 4.5-4.6eV, near/little lower than the E_f of

the perovskite. More importantly the E_f of PCBM is much closer to the φ_m of Cr. Hence a smaller Schottky barrier is expected at the Cr : PPP-PCBM interface in comparison to the Cr : PPP interface(*Figure 5-12*c). However the barrier at the Au interface is still large. In case of PPP-Spiro in contact with Au/Cr the final band diagram is shown in **Figure 5-12d**. Since Spiro-OMeTAD has a much lower E_f, the effective work-function for the bilayer would be below the Cr φ_m giving a profile shown in **Figure 5-12d**. A high band bending at the Au:PPP-Spiro interface would still exist due to the appreciable difference between the Au φ_m and E_f of the Perovskite. It is useful to recall that the amount of band bending is directly proportional to the electric field across the junction. Since PPP is in contact with both Spiro-OMeTAD and Au (Metal: High Density of States) simultaneously, a large band bending is bound to occur at both interfaces between PPP:Spiro and PPP:Au.

With the basic band diagrams established we can relate back to the Dark and Light I-Vs observed in **Figure 5-11.** In the case of PPP-SpiroOMeTAD the dark currents show a Schottky behaviour for both polarities- Cr positive/negative w.r.t to Au. This is easily seen from *Figure 5-12*d where there is a large injection or collection barrier for e^-/h^+ from the Au/Cr contacts respectively. In the presence of light it is seen that $Cr^{(+)}$-$Au^{(0)}$ shows appreciable photocurrent while $Cr^{(-)}$-$Au^{(0)}$ shows no photocurrent. This because in the presence of light the PPP is predominantly populated by e^{-s} (due to the h^+ transfer to the Spiro) and are the majority carriers in PPP in this configuration. Only in the $Cr^{(+)}$-$Au^{(0)}$ configuration in which the e^- is extracted from the Cr electrode (Ohmic: See **Figure 5-12d**) can there be a photocurrent. In the reverse $Cr^{(-)}$-$Au^{(0)}$ direction due to the unfavourable bending of the bands lower/no photocurrent is seen. *Hence the barrier in the extracting of charges seems to be the main determining factor for obtaining maximum possible photocurrents.* It must also be noted that each Schottky junction (having a field associated with it) at both electrodes act as a driving pathway to collect

e^-/h^+. In this case the band bending at both electrodes also favour the photocurrent to flow in the $Cr^{(+)}$-$Au^{(0)}$ direction.

In the PPP-PCBM case the Dark IV for the $Cr^{(+)}$-$Au^{(0)}$ case shows a Schottky behaviour as expected. Surprisingly for the $Cr^{(-)}$-$Au^{(0)}$ case an ohmic behaviour is found (also seen for reference samples). This at present is poorly understood. It is well known (as also seen from Chapter.4) that PCBM reacts with the Iodide ions at the positively biased electrode (Au here) possibly forming charge transfer complex dipoles which may assist in creating an ohmic barrier. This is an interesting development that needs a different line of investigation that will not be delved into here. In the case of light, holes in the PPP-PCBM will be the majority carriers in PPP since photo-generated electrons are transferred to the PCBM. Ideally there are no barriers for the hole collection at both electrodes. So the Light-IV are quite symmetric (40µW). A slightly larger photocurrent in the $Cr^{(-)}$-$Au^{(0)}$ may be related to the injection of holes which is easier from Au than from Cr. Light-IV at lower light intensities is plotted (8µW) is plotted to show the effect of the Schottky barrier at the electrode acting as a possible driving mechanism for charge collection at lower light intensities. At higher light intensities always an ohmic behaviour is obtained.

In the case of only PPP, (**Figure 5-12b**) the Dark-IVs are not ohmic (**Figure 5-11c**). In the presence of light both electrons and holes must be present in equal numbers. Electrons and holes have shown to have similar effective masses and mobilities in perovskites. Recent reports show e^- to be the dominant trapped carriers, while some have shown h^+ to be the dominantly trapped carriers. Assuming equal charge carrier densities of e^-/h^+ one may expect a mixed current from both charge carriers. Photo-generated hole collection has no barrier in both applied polarities (**Figure 5-12b**). However photo-generated e^{-s} find a larger barrier for collection at the Au electrode due to a larger band bending. This is reflected in **Figure 5-11c** where $Cr^{(+)}$-$Au^{(0)}$ shows much larger photocurrents than the $Cr^{(-)}$-$Au^{(0)}$ configuration.

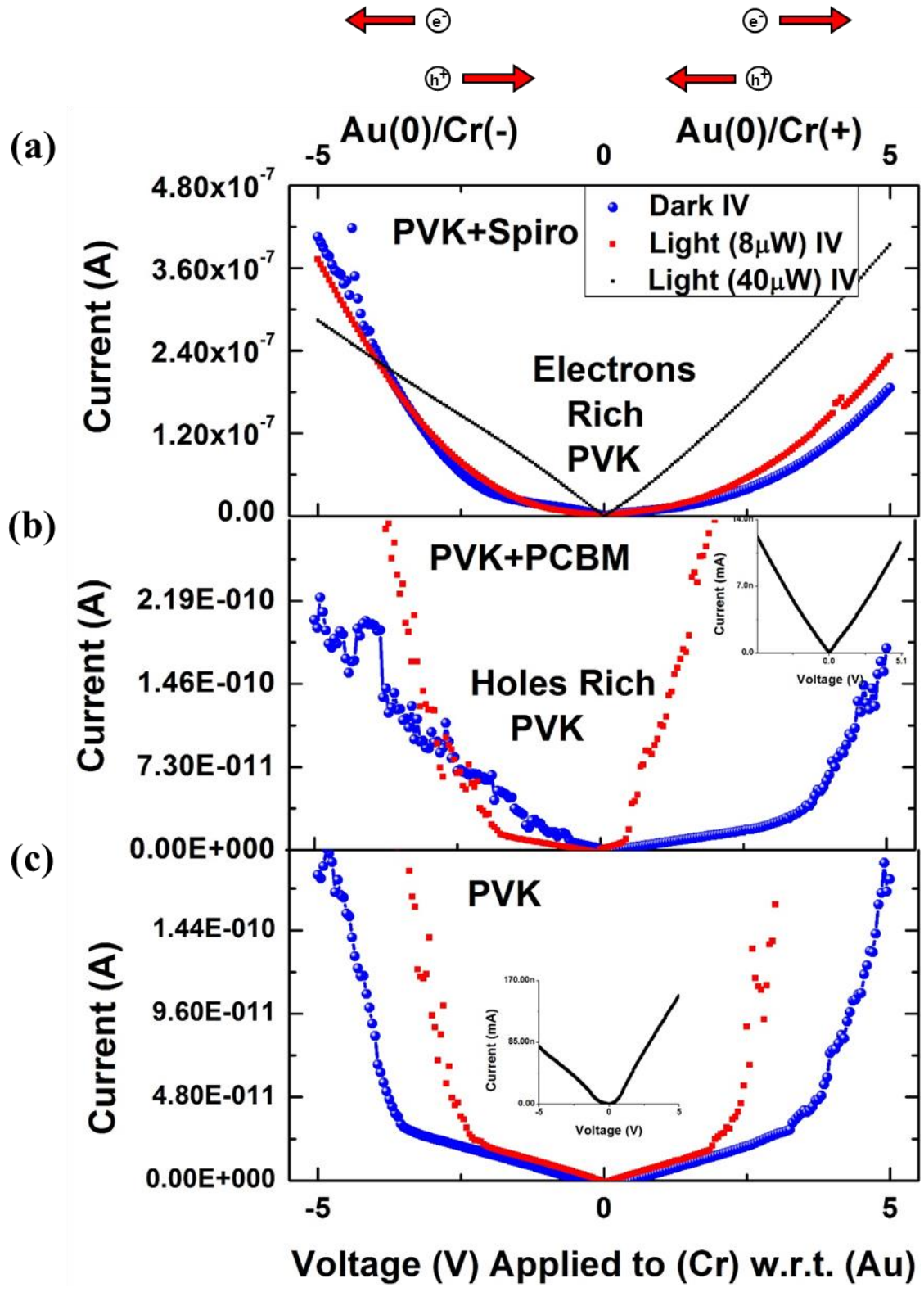

Figure 5-11 Use of Asymmetric Contacts (in terms of Work Function) in fabricating PPP PCs. Positive voltages are where Cr is biased positively and Negative voltages are where Cr is biased negatively- Au is always kept at 0V. Insets for b & c show I-V for higher light intensities for better clarity. Comments of Electron/Hole Rich in b & c is only valid in the case of light. Arrows on the figure top indicate the direction of transport of electrons and holes in the presence of light

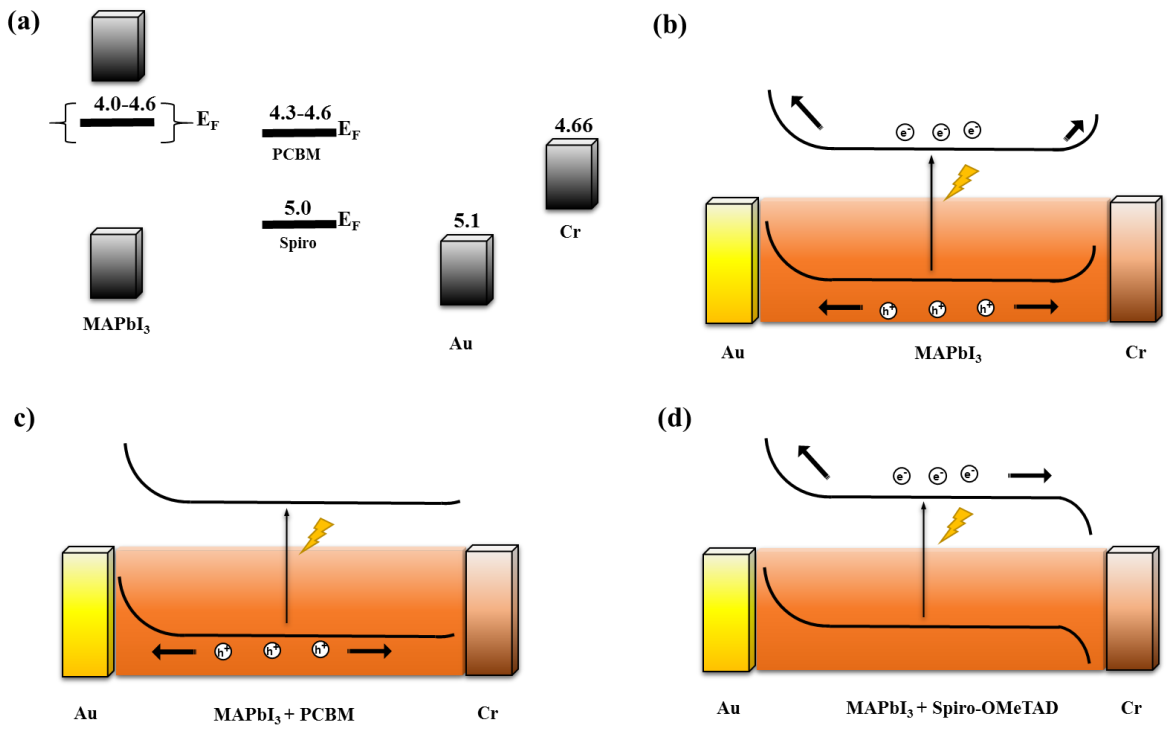

Figure 5-12 a)) Shows all the relevant energy levels of the active layers. Work function of Au/Cr/PCBM have been measured and give similar values to that in literature. Energy level alignments of the electrodes with $MAPbI_3$ (b) $MAPbI_3$+PCBM(c) $MAPbI_3$+SpiroOMeTAD (d). Also shown are the majority carriers in devices upon application of light on the device

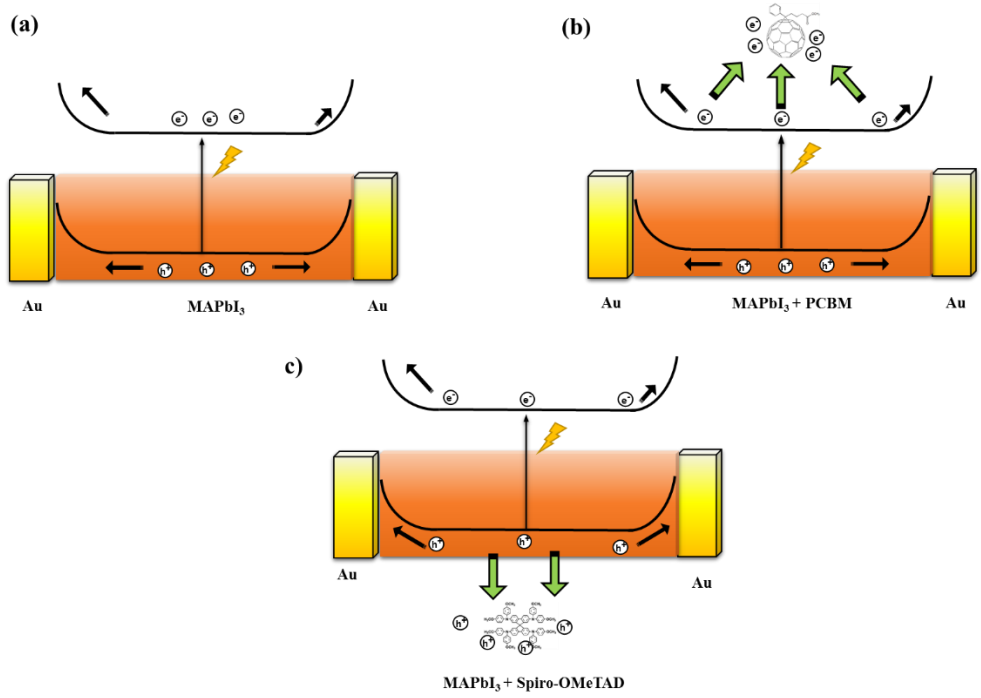

Figure 5-13 Energy level alignments of Au-Au PCs. a)In $MAPbI_3$ both e^-/h^+ are free to move b) In $MAPbI_3$+PCBM majority carriers are holes due to e^- transfer from $MAPbI_3$ to PCBM. c) In $MAPbI_3$+Spiro majority carriers are electrons due to h^+ transfer from $MAPbI_3$ to SpiroOMeTAD

In all of the three above cases the role of injection of charges (to maintain a photocurrent) from the electrode were not considered since in all cases injection of charges play little role in determining the final photocurrents. In the PPP:Spiro and the PPP cases, larger photocurrents are observed in polarities where the injection barrier was larger; *suggesting that collection barrier for either e^{-s} or h^{+s} is important*. The barrier for charge carrier collection plays a key role in the gain of the PCs.

In the studied PCs (Au-Au electrodes) the band-diagrams for the three cases, PPP, PPP-PCBM and PPP-Spiro are shown in (**Figure 5-13**). It is quite evident that the collection of photo-generated e^{-s} is highly restricted while that for holes collection is ideal. Hence for all three samples holes will be the faster extracted carriers. In **Figure 5-13a** with the PPP, due to the energetic barriers, electrons are bound inside the perovskite either in the band or into traps/defect states while the hole current remains efficient. The electrons recombine with the holes in a bi-molecular (radiative) or monomolecular (trap assisted) fashion which then dictates the gain in the PC. A simple way to improve the gain is the addition of PCBM, an electron acceptor which would accept the photo-generated electrons in PPP (**Figure 5-13b**). This would supress both the radiative recombination (PPP is depleted to e^{-s} & Recombination =Bnp , B=Bimlecular Recombination Co-efficient, n/p – Electron/hole density respectively) as well as the trapping of electrons (contributing to the monomolecular recombination). Few DFT models also show the effective passivation of deep electron traps by PCBM which can again improve the gain in these systems. Hence a three-fold strategy: 1. Confine the electrons within the CB of the PPP by creating a large barrier for extraction by having a U-Shaped band alignment 2.Simultaneously transfer the e^- to an electron acceptor and 3. Passivate electronic traps in the PPP, result into a large gain in these systems. It is now easy to see why PPP-SpiroOMeTAD samples do not work – photo-generated holes are transferred to the SpiroOMeTAD (**Figure 5-13b**) while the photo-generated electrons face a barrier for collection. Finally in order to

reconfirm if extraction barrier plays an important role, Cr-Cr electrodes on Si substrates are fabricated and the PPP-Spiro samples (where the e^{-s} are the majority carriers) are measured for light response. Though the U-shaped band type is valid even for the Cr-Cr samples the barrier for e^{-s} is considerably lowered and should be evidenced in our device response. As seen from **Figure 5-14**, Cr-Cr PCs show a much better On/Off ratio as well as larger photocurrents on a PPP-Spiro-OMeTAD than the Au-Au electrodes (40µW/Top illumination). This reaffirms the role of extraction barrier and the U-Shaped band scheme to obtain high gain in our devices.

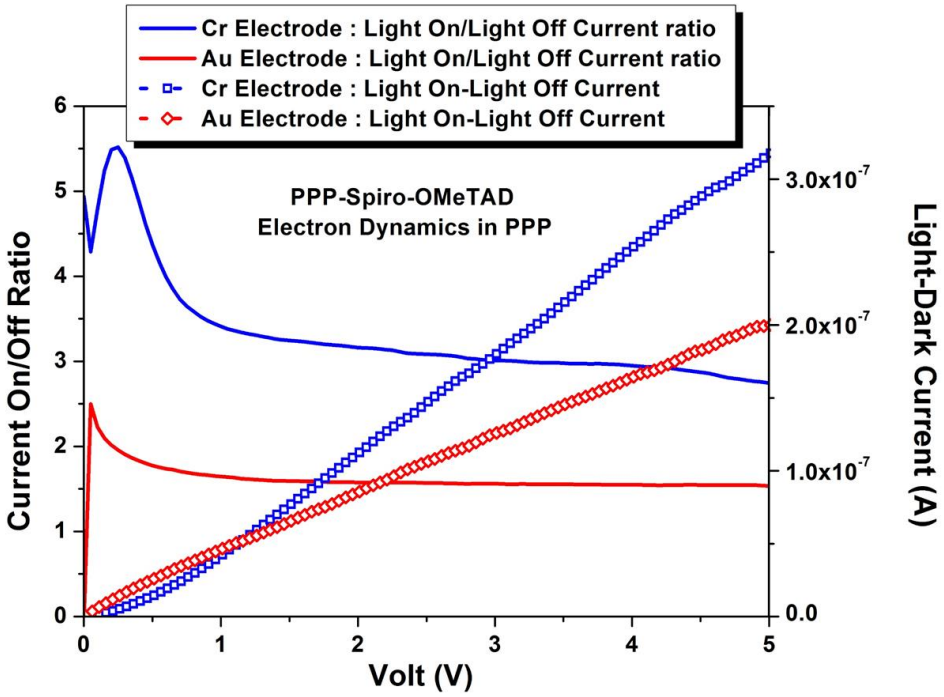

Figure 5-14 Electron Rich devices comparing Au-Au and Cr-Cr PCs. Here again the light is incident from the top side

Coming back to the photocurrent transients **Figure 5-10:** for the Reference devices with PCBM we have a transit time of ~ 800ns which is the transit lifetime of the hole conduction, the faster moving carriers ($t_{transit}$). For the Reference-SpiroOMeTAD we obtain close to a lifetime of 60µs which is the recombination lifetime of electrons the slower moving charge in the PC(τ_{Rec}) and hence obtain a gain close to 70. It must be noted that with the SpiroOMeTAD much higher intensities (10x times more intensity and a white light Sun source) had to be used, hence a

discrepancy (of a factor of 10) w.r.t to the measured Gain of 7 can be expected since for trap assisted SRH recombination, lifetimes are proportional to the excess charge carrier density of the recombining species (e^{-s} here). The transit lifetimes obtained demonstrate that application of Spiro-OMeTAD considerably supresses the gain while application of PCBM considerably enhances the gain as was expected where the gain is collection limited.

Trap Passivation:

Lastly, the role of defect states passivation by PCBM is probed which was seen in chapters 3,4 and the signs of which is also seen from noise measurements (**Figure 5-7**). First , a $1/f^{\alpha}$ noise (α is the exponent of the 1/f noise) is observed for PPP devices across the measured frequencies (**Figure 5-7**). With the addition of PCBM a clear suppression of $1/f^{\alpha}$ (characteristic of many trapping mechanisms[94,95]) noise is seen. Plotting the flat noise in the PPP-PCBM system against the theoretically minimum achievable noise of shot noise is shown in (**Figure 5-15**). Clearly seen is that the flat noise at higher frequencies in these devices are shot noises with no contribution from trap states which indicates of a good passivation by PCBM.

For bulk semiconductors the 1/f noise is usually dominated by the bulk volume. For such a bulk property the 1/f noise follows a Hooge's dependency[84,94,95]. **Figure 5-16** shows that only PPP-PCBM PCs show a1/f noise that follows a Hooge-type dependency while the PPP PCs show a much larger slope indicating an additional contribution of surface states to the 1/f noise. This reaffirms an effective passivation of surface states of PPP by PCBM in which the 1/f noise shows a bulk-like dependency for PPP-PCBM PCs.

As was seen in Chapter 4, applying a bias moves iodide ions creating interstitials/vacancies and creating defect states. Iodide interstitials act as hole traps [51], which in Chapter 4 is proposed are passivated by PCBM. This should also in principle increase the gain in these devices. Also DFT modelling, Thermal Admittance Spectroscopy studies have shown passivation of deep

level defects by application of PCBM. Hence as also seen from the noise measurements passivation is another important factor to improve the G, D* and transient lifetimes in these devices.

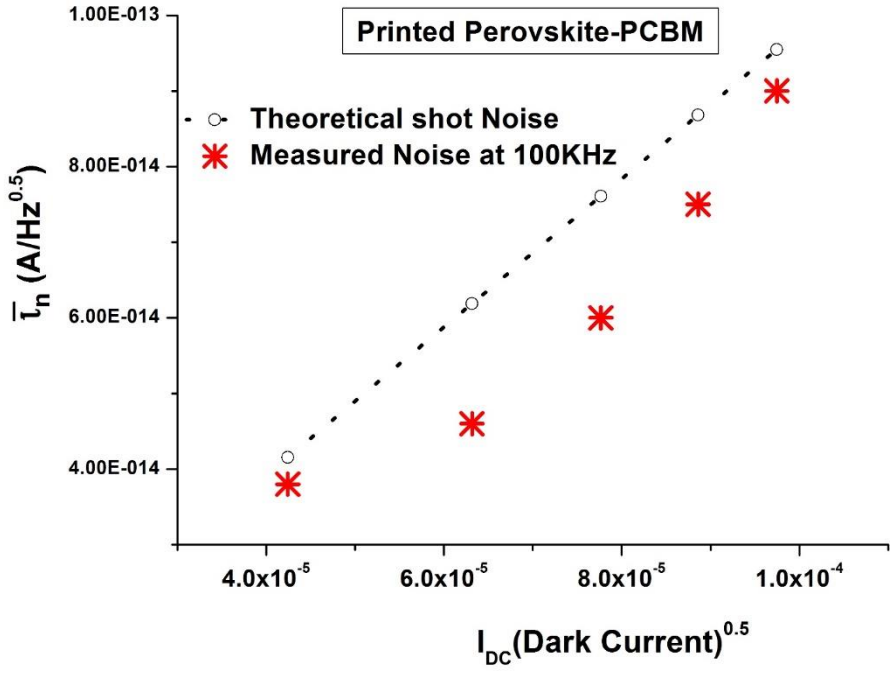

Figure 5-15 The flat-noise current obtained at higher frequencies for the PPP-PCBM PC as a function of the theoretical shot noise in the system obtained from the dark current in the device.

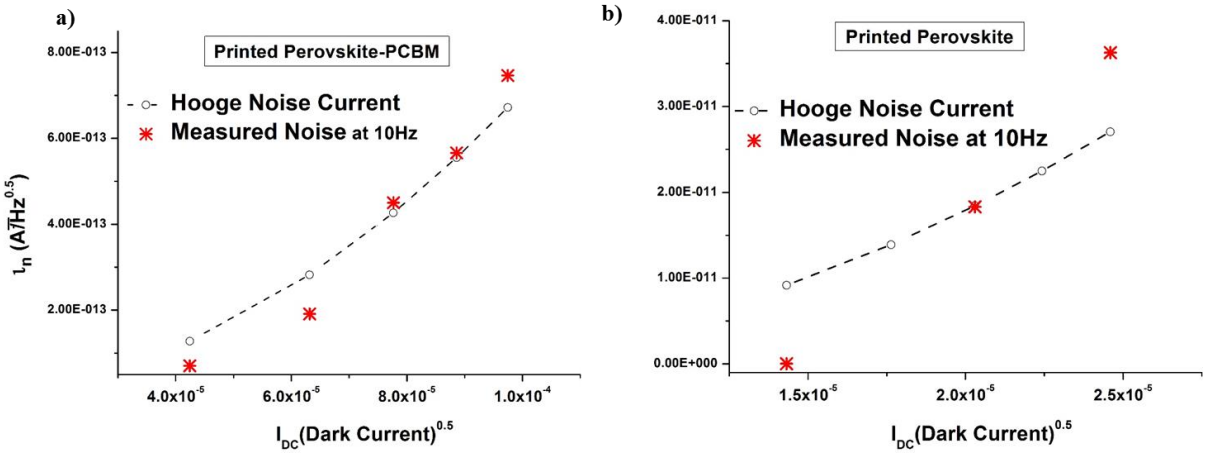

Figure 5-16 Dependency of the 1/f noise current (f=10Hz) for PPP-PCBM and PPP PCs with respect to the dark current. We find a Hooge type dependency only for the PPP-PCBM PC

Finally a comment on the comparison of the PPP devices with reference 2-Step perovskites. Much larger Responsivities in PPP-PCBM are found in comparison to the Reference-PCBM because the PPP films are micro-crystal films and are porous. Hence a better contact can be made between PPP and PCBM and a much effective passivation can be achieved. Hence the effect of PCBM on PPP is expected to be much larger.

5.5. Conclusion

In conclusion, in this chapter it has been demonstrated that through a very simple chemical route of synthesis one can print state of the art $MAPbI_3$ PCs. This is done without using any corrosive or harmful solvents. Large responsivities close to 80A/W for these devices and Gain more than 100 are obtained. Also Specific Detectivities D* (cm-$Hz^{0.5}$-$Watt^{-1}$) ~ 6×10^{13} for PPP-PCBM films and 3×10^{14} for reference films are observed. Our PCs are exceptionally fast and show transient response in 18µs for PPP-PCBM and 800ns for our Reference-PCBM films. They also exhibit exceptionally high theoretical Linear Dynamic Range of 142dB with the PCBM layer on top for both PPP and Reference films. We were able to measure an LDR of up to 53dB. On probing the mechanism that delivers good figures of merit it is found that extraction of charges and the band-alignment in these PCs is important. By using Au electrodes we create a large barrier for collection of photo-generated electrons while providing a favourable transport and collection of photo-generated holes by creating a U-Shaped band alignment. This provides a good gain in the device by selectively circulating photo-generated holes in the device while photo-generated electrons are electrostatically trapped in the C.B. A drastic improvement in the performance is achieved by applying an electron accepting PCBM on the perovskite which accepts photo-generated electrons. This depletes the perovskite of photo-generated electrons while the flow of holes in the device continues. Finally the PCBM

not only acts as an electron acceptor to improve the performance of the PCs but also plays an active role in passivating surface trap states pf the PPP thereby further improving the performance of the PCs

6 Enhancing Interfaces for $MAPbI_3$ devices–Layered Materials and Chemical Defect Passivation

6.1 Layered Materials: WS_2 as Hole Transport Materials to Supress Noise and Boost Detectivity of MAPbI3 Photodetectors

Introduction

In the previous chapters we discussed the stability of $MAPbI_3$ interfaces. Along with $MAPbI_3$, the stability and processing of the charge selective layers are of high importance. Organic semi-conductors such as Spiro-OMeTAD have been the clear favourites as Hole Transport Layers (HTL) in devices. However these organic HTLs degrade at high working temperatures (85^0C) over a short period of time, they do not inhibit the migration of the metal cathode electrodes decreasing the stability of the devices. Another major setback for the Organic-HTL are their very high pricing due to multi-step synthesis and low yields. A promising alternative are the use of inorganic-HTLs, especially transition metal dihalcogenides (TMDCs) which are inorganic HTLs that can be large area processed from solution[58,96–99]. TMDCs with a chemical formula of MS_2 grow in a layered form where one hexagonal metal plane (M) is sandwiched between two hexagonal chalcogen planes (S). The thickness of this one unit of 3 planes is about 1nm. The units are weakly bound and form a large anisotropic crystal. Herein the well-studied TMDC of Tungsten-Di-Sulphide (WS_2) is utilized as a replacement of the organic HTL. The WS_2 is processed in air through spray coating and fabricate photodetectors (PDs) of a Mixed

Cation-Mixed Halide Perovskite ($Cs_{0.175}FA_{0.825}PbBr_{0.3}I_{0.7}$). We find that for HTL formation, air-processed WS_2 show lower noise and higher specific detectivities than the usually employed Spiro-OMeTAD HTL that is processed in inert N_2 conditions. Also since the WS_2 is spray coated it is much more amiable to industrial and printing processes than spin coating that is used for Spiro-OMeTAD. The air and working stability of PDs with WS_2 is expected to be much higher than Spiro-OMeTAD and is presently being tested.

Materials and Device Characterization:

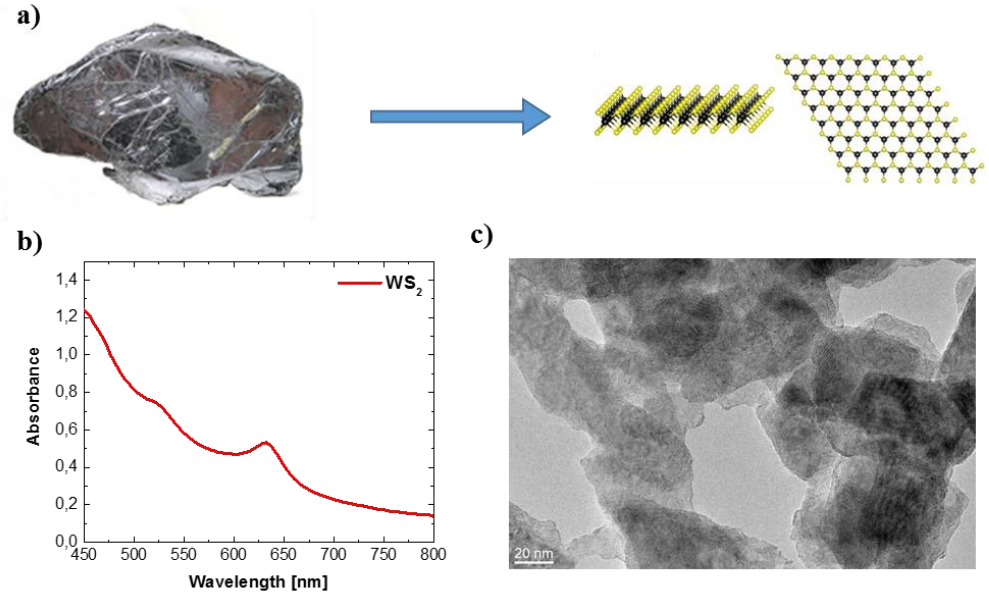

Figure 6-1 : a) Exfoliation of sheets of WS_2 is performed through a surfactant and sonication b) Absorption spectrum of the exfoliated particles c) TEM image of the exfoliated particles on a Cu mesh.

The WS_2 preparation and device making was performed by my colleague Peter Topolovsek and is briefly described here. WS_2 crystalline powder is treated with a surfactant sodium cholate dehydrate solution in a mixture of ethanol and water by intense sonication. The surfactant exfoliates the individual TMDC units bound by a weak hydrogen bonding. The unexfoliated large particles are separated by centrifugation. The exfoliated particles in the solution are treated with high seed centrifugation and material washing (3 Steps Milli-Q and final step

ethanol) to remove the surfactants. After the particles are dispersed in ethanol and is used to spray coat the HTL on top of the Perovskite. **Figure 6-1a** indicates the process of converting a WS_2 crystal into layered units of WS_2. **Figure 6-1b** shows the absorbtion spectrum and **Figure 6-1c** shows the TEM image of the layered particles. The lateral dimension of the particles are around 20-30nm with each particle being single layer thick. The final devices structure used for PDs are shown in **Figure 6-2**. We use a mixed cation mixed halide perovskite since they have demonstrated good air and temperature stability (ref). This is a critical requirement for the possibility of our HTLs being processed in air.

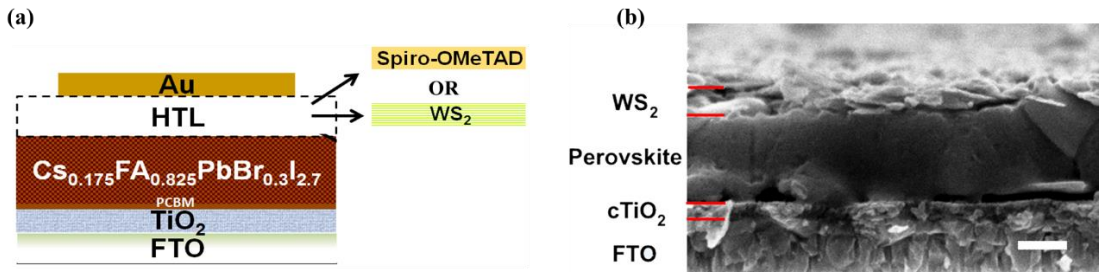

Figure 6-2 a) Shows the schematic of the device structures used. The commonly used HTL of Spiro-OMeTAD is replaced by layered particles of WS_2 with varying thickness b) Cross-section of the device. Scalebar-200nm

Device Performance

The PDs studied here are the reference with the Spiro-OMeTAD and two varying thickness of layered-WS_2 layer (5nm and 10nm) that show best responsivities (R). All presented data is at short-circuit condition at 0V. **Figure 6-3a** shows the responsivities for the three PDs which show similar performances. It must be kept in mind that Spiro based devices are fabricated in an inert N_2 atmosphere while in devices with WS_2, the HTL is processed and spray coated in air. Hence obtaining similar R for the two devices is evidence of good stability of the mixed cation perovskite layer. **Figure 6-3b** shows that the Specific Detectivity calculated is appreciably higher for devices with WS_2 where we achieve good values of up to 1.5×10^{12} cm-$Hz^{0.5}$/Watt. To probe this, we fabricate devices with varying thickness of WS_2. **Figure 6-3c**

shows the reverse dark current. PDs with WS_2 consistently show a decreased dark current in comparison to the Spiro-OMeTAD devices. The exception being very low thicknesses of WS_2 which lead to a non-continuous layer of the WS_2 and create shorting paths between the electrode and the perovskite. Suppression of dark currents is usually a sign of supressed noise in devices. **Figure 6-3d** shows the noise in the devices, where lower noise is observed for devices with layered-WS_2 as the HTL. Lower noise hence leads to higher Specific Detectivities for devices with layered-WS_2. This is an important development since interfacial traps increase the noise in the system, indicating that processing of WS_2 in air has not led to additional traps in the PDs. At frequencies beyond 3kHz the peak is due to the narrow band-width of the measurement setup (Capactive part of the Op-Amp) and is not indicative of the noise from the device. Increasing the thickness of the WS_2 layer we see a decrease in the noise. However at much larger thickness we see a saturation in this decrease of noise.

We now characterize the temporal response of the devices and is shown in **Figure 6-4a**. All devices show fast response in the order of few microseconds. The devices with Spiro-OMeTAD have a response time of 4.5 µs while devices with layered WS_2 have a response time of about 12µs. These response times are much faster than solution processed organic photodetectors and are one order slower than the best Perovskite Photodetectors. The linearity of the photocurrent as a function of the light intensity is shown in **Figure 6-4b**. All devices show saturation of the photocurrent at the same high light intensities. The lower noise in the WS_2 devices however gives us a better theoretical LDR for the WS_2 devices (112dB) than Spiro based devices (103dB).

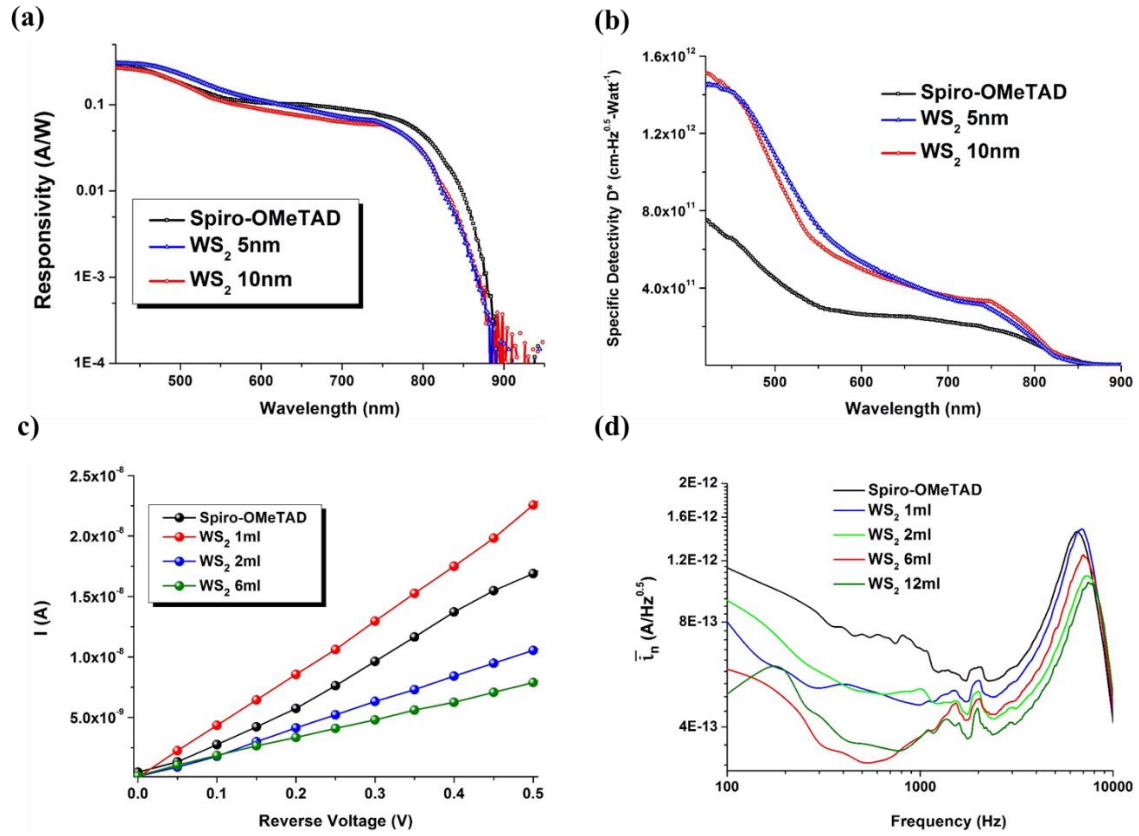

Figure 6-3 a) Responsivities of all the PDs are shown where the reference and the devise with layered WS_2 show similar performance b) Specific Detectivities for the devices are shown where layered WS_2 higher performane than the reference devices c) Dark current suppression in the reverse bias upon using layered WS_2 as a HTL d) Noise current for devices with layered WS_2 show lower noise. The bandwidth is limited up to 3kHZ due to the measurement circuit.

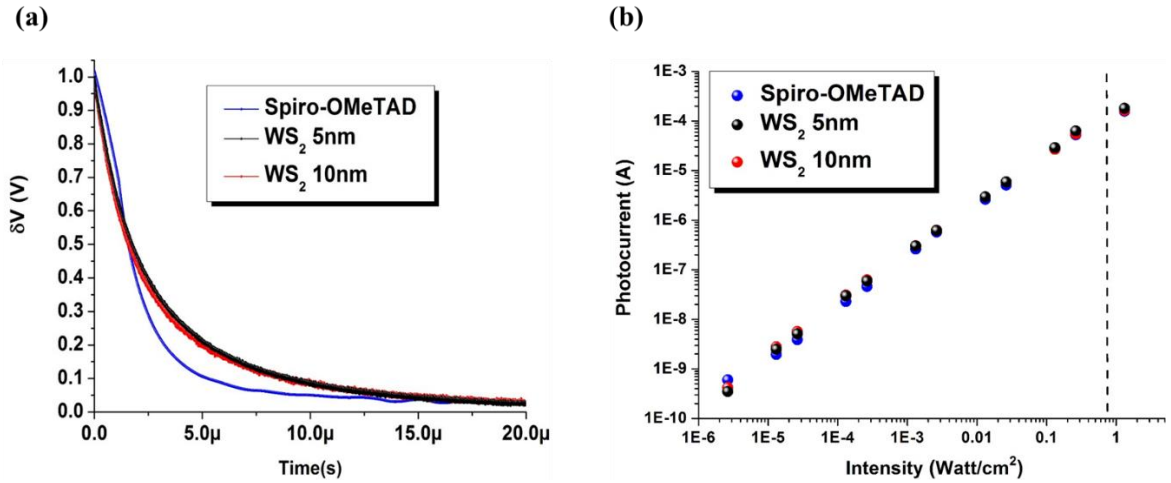

Figure 6-4 a) Temporal response of all the devices are shown b) Linearity of the photocurrent is plotted against the incident light intensity (Red 672nm)

Conclusion and Outlook

In conclusion in this chapter layered inorganic TMDC - WS_2 has been successfully used to replace the commonly used organic HTL of Spiro-OMeTAD in Perovskite PDs. The HTL is

processed in air and does not require an inert atmosphere for deposition. It outperforms the reference Spiro-OMeTAD PDs by successfully supressing the dark current and reducing the noise in the devices. Presently stability tests are being performed where the inorganic HTLs are expected to well outperform the organic counterparts. Hence layered TMDCs represent a promising alternative to organic HTLs for Perovskite PDs to improve their performance as well as working stability.

6.2 Chemical Defect Passivation in $MAPbI_3$ Perovskite Solar Cells

1. Introduction

In this section of the chapter, chemical passivation of the $MAPbI_3$ interface by using passivants molecules is presented. The molecules are synthesized by my colleague Jeroen van der Welden. It has been recently reported that thiophene, pyridine and similar molecules spin coated on top of $MAPbI_3$ lead to higher efficiencies and possible passivation of traps at the interface[100–108]. One of the possible mechanism suggested are the anchoring of the the acidic sections of the molecules at the un-cordinated lead sites on the surface of the $MAPbI_3$ films. During film formation, presence of uncoordinated lead atoms at the surface is expected due to an abrupt end of the perovskite crystal. Also the migration of I^- ions can cause the formation of such uncoordinated lead atoms in the perovskite crystal. These Pb sites act as point defect and can be expected to increase the non-radiative recombination in solar cells [12]. One method to passivate such sites is to use pyridine and thiophene based organic ligands that will electrostatically bind with such Pb sites.

2. Materials and Devices:

In this work two molecules of Pyr-TPA and Thiophene-TPA are used with the binding groups of Pyridine and Thiophene **Figure 6-5a**. To effectively passivate only the uncoordinated Pb atoms on the surface, the passivants treated $MAPbI_3$ film is washed with ethanol to remove the

extra passivants molecules. So only a mono-layer of the passivants molecules is expected on top of the $MAPbI_3$. An additional hole transporting moiety of TPA is attached to the anchoring group which can act as a conduit between the $MAPbI_3$ and the HTL. Hence the passivation is applied to the perovskite surface between the $MAPbI_3$ and the HTL of Spiro-OMeTAD.

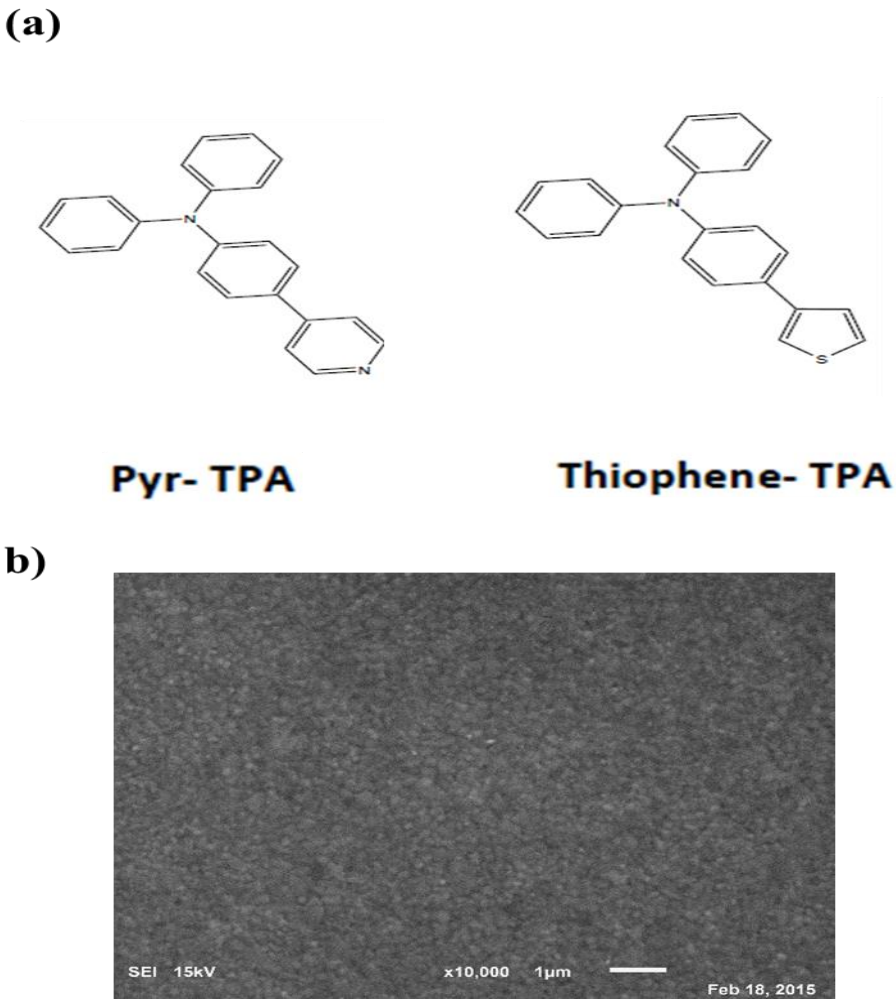

Figure 6-5 a) Chemical structure of the two passivants molecules Pyr-TPA and Thiophene-TPA b) SEM image of the Passivants treated $MAPbI_3$ film free of ponholes

The anchoring groups anchor to the uncoordinated Pb passiating defect sites while the TPA enables a good hole conduction to the HTL Spiro-OMeTAD. Passivants treated $MAPbI_3$ films are shown in **Figure 6-5b** which is free of any pinholes. We use a standard device structure used in chapters 3 and 4 without the PCBM interlayer between the TiO_2 and $MAPbI_3$. The performance of the devices are shown in **Table 1**. The fast scans (500mV/sec) and slow scans (50mV/sec) both show higher efficiencies for devices treated with passivants molecules. The

J-V for the devices are shown in **Figure 6-6 a-c**. As can be clearly seen is that in the presence of passivants molecules there is large drop in the hysteresis of the solar cells. Hysteresis is a paramount issue in Perovskite solar cells and using passivants can be an effective way to supress it. Besides supressing hysteresis there is also a slight improvement in the stabilized efficiency for devices with the Thiophene-TPA **Figure 6-6d**.

AVERAGE:		Efficiency)	Jsc	Voc	FF	Efficiency	Jsc	Voc	FF
		FWD Scan				Backward Scan			
Reference	FAST	11.58	16.50	0.969	72.40	8.334	16.55	0.906	55.51
Molecule Pyr		10.87	16.90	0.948	67.88	9.953	16.93	0.915	64.23
Molecule Thioph		11.65	17.63	0.977	67.63	9.870	17.84	0.914	60.54
Reference	SLOW	9.790	15.50	0.926	68.09	5.155	15.15	0.931	36.40
Molecule Pyr		10.37	16.10	0.941	68.62	3.935	15.75	0.941	26.48
Molecule Thioph		10.32	15.84	0.929	70.27	4.451	15.15	0.948	30.96

Table 1 : All the solar cell J-V characteristics listed. Shown are Reference devices without passivation and for Pyr-TPA and Thiophene-TPA. Both Fast Scans and Slow Scans in Forward (Voc-Jsc) and Reverse (Jsc-Voc) directions are shown. The shown values are averages over 10-15 individual devices

One of the major challenges in this work remains in increasing the reference efficiency of the devices. The Perovskite here is fabricated with a 2-Step method as described in the Materials and Methods Chapter. As a part of the project these molecules have been also tested with a collaborator at Oxford and indeed a much larger increase in efficiency is observed (13% Reference to a 16% with passivant). However for those devices, a different route for forming the Perovskite by using a PbAc precursor is used which is expected to change the surface of their film in comparison to our films[109].

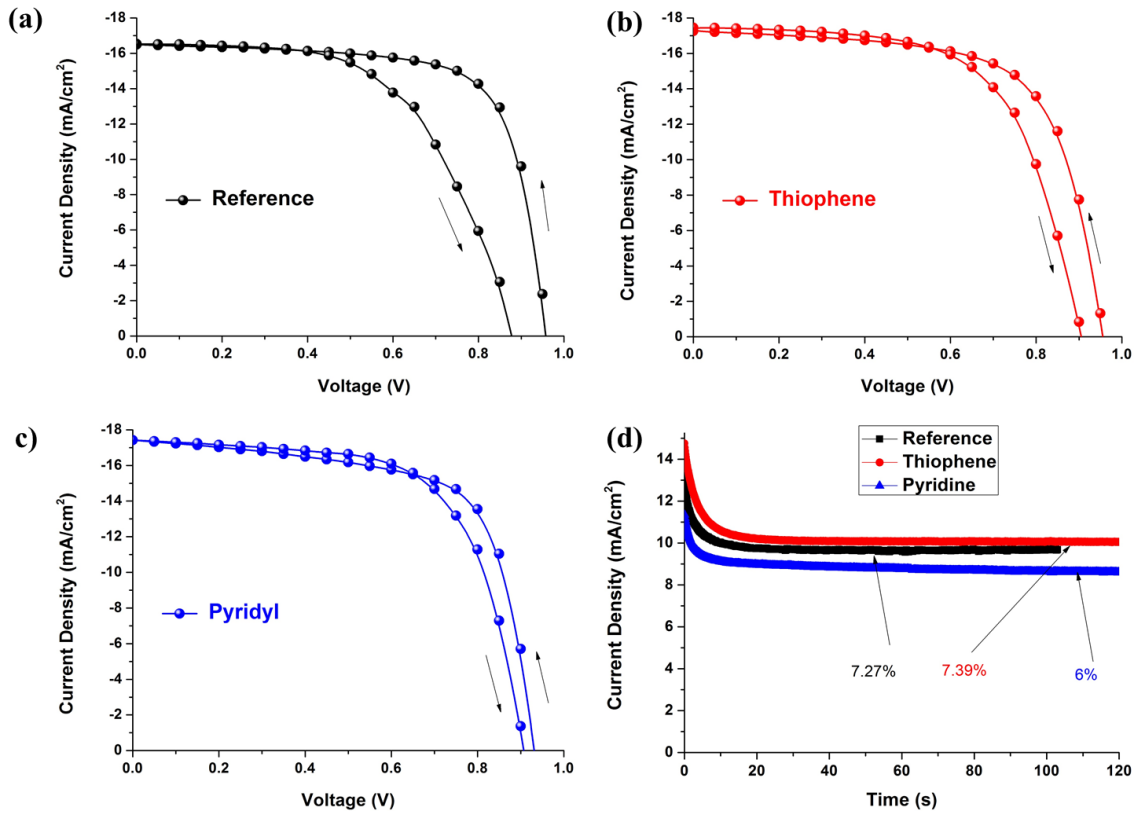

Figure 6-6 J-V curvs for a fast scan rate are shown for a) Non-treated Reference b) Thiophene-TPA and c) Pyr-TPA based devices d) Stabilized power efficiencies for the three solar cells.

3. Conclusion and Outlook

In conclusion of this section of the chapter, it is found that chemical passivants which are able to electrostatically bind to the uncoordinated atoms in the perovskite surface improve the performance of the solar cells. Also a decrease in hysteresis is seen in comparison to untreated devices. We attribute this to a possible passivation of the point defects at the Perovskite surface. A TPA is used to achieve an efficient hole transfer from this passivated site to the Spiro-OMeTAD. Hence this work reveals the promise of using passivants materials or Hole Transport Layers themselves with anchoring groups such as a thiophene group which can anchor and coordinate with the point defects on Perovskite surfaces. Moving forward this work can expand

into employing Passivants or HTLs with anchoring group attached to a Relay structure (ref), graded energetic structure (ref) and electron/hole blocking moieties.

7 Conclusions and Outlook

Conclusions:

The major focus of this thesis is on understanding the critical role interfaces and interfacial layers play in determining the working efficiencies and stability of Organic Lead Halide Perovskites (OHP) based devices. While quite diverse in the applied techniques and devices, the main theme remains on understanding the importance of the interfacial energetics in OHP based devices. It is seen that surface energetics critically dictate the working efficiencies and stability of these devices and in many cases are the bottleneck for achieving higher performances.

In Chapter 3 evidence of large accumulated electronic charges in OHP solar cells at the OHP/TiO_2-EEL(Electron Extraction Layer) interface in dark and under light is presented. The accumulated electronic charges at this OHP/TiO_2 interface produce giant capacitances at low frequencies. At OHP/PCBM interfaces, the large charge accumulation and giant capacitances are supressed and thus demonstrating the important role of interfaces. In the presence of light an extra trapping and recombination process is observed for the OHP/TiO_2 interface in comparison to the OHP/PCBM interface. This is a suggestive evidence for the passivation of interfacial trapping states by PCBM. The accumulation and trapping of electronic charges increases over time under light soaking.

In Chapter 4, the working mechanism and the role played by the EELs in devices is explored. It is expected that the accumulating I^- ions at the interface create defect states. DFT modelling has shown I^- interstitials to create hole traps. These suggest that the accumulated and trapped charges observed in Chapter 3 at the OHP/TiO_2 interface are holes. Large accumulation of positively charged species have also been observed experimentally at OHP/EEL interfaces in devices. However, these are preliminary reports and the further nature of the defect states needs to be explored. Further, the role played by PCBM in passivating the OHP interface is probed. It is seen that PCBM reacts chemically with the accumulating I^- ions at the OHP/EEL interface. PCBM becomes n-type doped by the accumulated I^- ions. This might provide insights for understanding the exact mechanism of how PCBM reacting with accumulated I^- passivates the interface states. Applying interfacial EEL layers that react with I^- ions can prove to be an effective strategy for stabilizing OHP based devices. Indeed the working stability of devices for PCBM based devices is shown to be much larger.

In Chapter 5, continuing with the use of interfacial layers to enhance device performances, PCBM is used as an electron acceptor and as trap passivation layer to improve the working of Printable Perovskite Particle (PPP) Photoconductors (PCs). PCBM acts as an interfacial electron acceptor that accepts photo-generated electrons from the PPP, thereby circulating holes in the PPP-PCs. From noise analysis, the $1/f^{\alpha}$ noise in the PCs are supressed by using PCBM, indicating passivation of interfacial traps in the PPP. The performance of the PCs are comparable to many Si-Photodiodes and display the promise of OHPs in photo-detection applications.

In Chapter 6, two works based on WS_2 layered materials as a Hole Transport Layer (HTL) and different molecules for passivating the uncoordinated lead sites are discussed. Inorganic HTLs (layered WS_2) are shown to be a promising alternative for OHP based photodetectors (PDs) by supressing the noise and increasing device stabilities in devices. Next, chemical passivation

with molecules that can bind with the uncoordinated lead bonds in OHPs is shown to enhance the performance and decrease the observed J-V hysteresis in devices.

Outlook:

OHPs have shown great promise of providing a pronounced impact for energy harvesting and opto-electronic device applications. Since device operation causes ion migration within the Perovskite semiconductor, interfacial defect states may play a more significant role in these semiconductors than their counterparts. The migrating ions are anticipated to accumulate at the semi-conductor interfaces which may then increase the density of interface states[12,28,66]. Many strategies can be applied to mitigate these effects. Applying an interfacial layer that interacts with the accumulated ions to mitigate the effects as shown in the thesis is a promising approach. Other approaches include applying interfacial layers that passivate interfacial vacancies and dangling bonds in OHPs. Presently these strategies are not very well explored in comparison to traditional Si and GaAs semiconductors which presents an exciting opportunity for further exploration. A golden standard still remains finding strategies to fabricate OHPs where migration of ions is supressed. The rapid progress made in OHPs in the last 6 years, only shows a promising scenario for the research community to find multiple solutions.

Future Work: Transient Photocurrent at Open Circuit Voltage

Building upon the transient techniques used in the thesis, a new technique is developed herein for obtaining deeper insights into the working of PSCs. One of the main problem associated with the Transient Photocurrent/Photovoltage (TPV/TPI) techniques applied for PSCs is related to the differential capacitance and charge densities calculated from this technique[18,19]. Δq is the collected charges from TPI transients. Δq is used to calculate differential capacitances and charge densities in the transient measurements. In Organic/DSSC solar cells few conditions need to be satisfied for this treatment to be valid: In particular the non-geminate recombination

needs to be negligible. However Perovskite Solar Cells (PSCs) are different, since the semi-conductor $MAPbI_3$ consists of migrating ions and can be polarized. Hence, similar arguments may not hold valid in the case of PSCs. The spatial distribution of ions and the Polarization within $MAPbI_3$ is significantly different when the PSCs are at Open Circuit (TPV) or at Short Circuit (TPI) conditions. It has been shown that ions and different polarizations of $MAPbI_3$ change the rates of electronic charge transport/recombination[11,14,16]. Hence comparing transients and lifetimes from short circuit or open circuit conditions are no longer valid for Perovskite Semiconductors: since the semi-conductor is at two different inequivalent states. This new technique is developed that can hold valid for Perovskite and other similar semi-conductors.

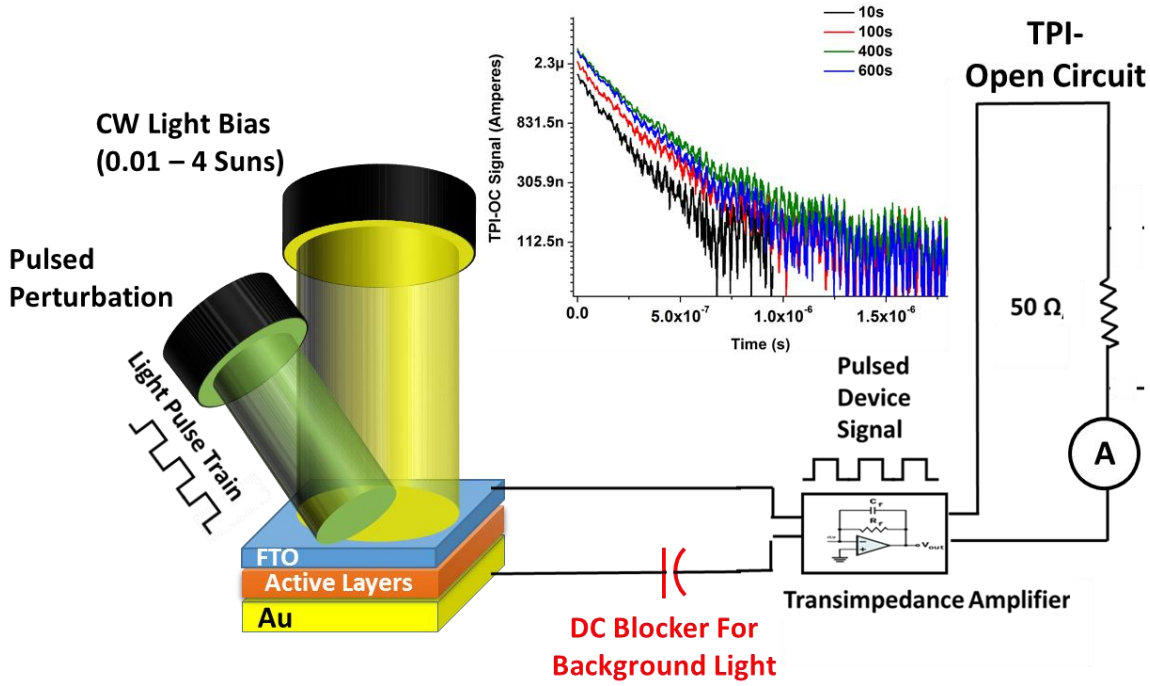

Figure 7-1 Setup of the TPI-OC is shown with the DC blocker foe the Background Light. The inset shows evolution of the TPI-OC transients for PSCs under light soaking.

In order to overcome this, measuring TPI near Open Circuit Voltage (TPI-OC) is developed. Small perturbation photocurrent is measured near the Open Circuit, which ensures that the TPV and TPI are measured in the same state of the cell of Open Circuit. This ensures that TPI-OC

& TPV are measured when $MAPbI_3$ in the two measurements is at the similar polarization, charge density and spatial configuration of migrated ions.

The cell is kept at the Open Circuit condition only for the DC Background Light source. While for the perturbation pulse the current is let to flow in the cell to obtain the small perturbation current (TPI-OC). Since the light pulse is a perturbation in comparison to the background light, the solar cell is at an Open-Circuit condition for all practical purposes. Hence similarity in the device configuration at TPI-OC and TPV is realized. To achieve this a capacitor $C(\omega)$ is connected across the PSC that blocks the DC current created by the Background Light, while passes only the AC Perturbation current created by the Perturbation Pulse. The Value of the Capacitor required is designed by considering the device geometrical capacitance and the other capacitances in the device at the Perturbation Frequency (~100KHz). The design is shown in. For PSCs , capacitors of around 100nF-1µF are used. Like with TPV/TPI measurements are done at an interval of 5-10secs with averaging. Preliminary results on TiO_2 devices used in Chapters-3/4 are shown in the inset of . An evolution of TPI-OC with light soaking is also observed. Charge density calculations and temperature dependent studies using this technique will be pursued for PSCs in the near future.

Bibliography

1. NASA. Global Warming Data Center : Carbon Dioxide Levels http://climate.nasa.gov/evidence/.

2. PV-Insights:Market Research: http://pvinsights.com/.

3. Park, N. Switchable photovoltaics. *Nat. Mater.* **14,** 140 (2015).

4. Woon Seok Yang, 1* Jun Hong Noh, 1* Nam Joong Jeon, 1 Young Chan Kim, 1 Seungchan Ryu, 1 Jangwon Seo, 1 Sang Il Seok. High-performance photovoltaic perovskite layers fabricated through intramolecular exchange. *Science (80-.).* **348,** 1234 (2015).

5. Saliba, M. *et al.* Cesium-containing triple cation perovskite solar cells: improved stability, reproducibility and high efficiency. *Energy Environ. Sci.* **9,** 1989–1997 (2016).

6. Abate, A., Giordano, F., Baena, J. C. & Decoppet, J. Efficient luminescent solar cells based on tailored mixed-cation perovskites Efficient luminescent solar cells based on tailored mixed-cation perovskites. (2016). doi:10.1126/sciadv.1501170

7. Tsai, H. *et al.* High-efficiency two-dimensional Ruddlesden–Popper perovskite solar cells. *Nature* **536,** 312–316 (2016).

8. Li, X. *et al.* A vacuum flash-assisted solution process for high-efficiency large-area perovskite solar cells. *Science (80-.).* **353,** 58–62 (2016).

9. Ball, J. M. & Petrozza, A. Defects in perovskite-halides and their effects in solar cells. *Nat. Energy* **1,** 16149 (2016).

10. Sidebottom, D. L. Colloquium: Understanding ion motion in disordered solids from impedance spectroscopy scaling. *Rev. Mod. Phys.* **81,** 999–1014 (2009).

11. Calado, P. *et al.* Evidence for ion migration in hybrid perovskite solar cells with minimal hysteresis. *arXiv* 1–40 (2016). doi:10.1038/ncomms13831

12. Azpiroz, J. M., Mosconi, E., Bisquert, J. & De Angelis, F. Defect migration in methylammonium lead iodide and its role in perovskite solar cell operation. *Energy Environ. Sci.* **8,** 2118–2127 (2015).

13. Bryant, D. *et al.* Observable Hysteresis at Low Temperature in 'hysteresis Free' Organic-Inorganic Lead Halide Perovskite Solar Cells. *J. Phys. Chem. Lett.* **6,** 3190–3194 (2015).

14. Barnes, P. Optoelectronic Transient Probes of the Mechanism Underlying Hysteresis in Hybrid Perovskite Solar Cells. *Light. Energy Environ.* PM4B.1 (2016). doi:10.1364/PV.2016.PM4B.1

15. Richardson, G. *et al.* Can slow-moving ions explain hysteresis in the current-voltage curves of perovskite solar cells? *Energy Environ. Sci.* **9,** 1476–1485 (2016).

16. Belisle, R. A. *et al.* Interpretation of inverted photocurrent transients in organic lead halide perovskite solar cells: proof of the field screening by mobile ions and determination of the space charge layer widths. *Energy Environ. Sci.* **131,** 6050 (2017).

17. Jacobs, D. *et al.* Hysteresis phenomena in perovskite solar cells: the many and varied effects of ionic accumulation. *Phys. Chem. Chem. Phys.* **19,** 3094–3103 (2017).

18. Montcada, N. F. *et al.* Analysis of Photo-Induced Carrier Recombination Kinetics in Flat and Mesoporous Lead Perovskite Solar Cells. *ACS Energy Lett.* acsenergylett.6b00600 (2016). doi:10.1021/acsenergylett.6b00600

19. Tao, C. *et al.* Fully Solution-Processed n-i-p-Like Perovskite Solar Cells with Planar Junction: How the Charge Extracting Layer Determines the Open-Circuit Voltage. *Adv. Mater.* 1604493 (2017). doi:10.1002/adma.201604493

20. Onoda-Yamamuro, N., Matsuo, T. & Suga, H. Dielectric study of CH3NH3PbX3 (X = Cl, Br, I). *J. Phys. Chem. Solids* **53,** 935–939 (1992).

21. Jonscher, A. K. Dielectric relaxation in solids. *J. Phys. D. Appl. Phys.* **32,** R57–R70 (1999).

22. Schroder, T. & Dyre, J. Scaling and universality of ac conduction in disordered solids. *Phys. Rev. Lett.* **84,** 310–3 (2000).

23. Bisquert, J., Bertoluzzi, L., Mora-sero, I. & Garcia-belmonte, G. Theory of Impedance and Capacitance Spectroscopy of Solar Cells with Dielectric Relaxation , Drift-Di ff usion Transport , and Recombination. (2014).

24. Correlation spectrum analyzer for direct measurement of device current noise. *Rev. Sci. Instrum.* **73,** 2717–2723 (2002).

25. Eames, C. *et al.* Ionic transport in hybrid lead iodide perovskite solar cells. *Nat. Commun.* **6,** 7497 (2015).

26. Li, C. *et al.* Iodine Migration and its Effect on Hysteresis in Perovskite Solar Cells. *Adv. Mater.* **28,** 2446–2454 (2016).

27. De Bastiani, M. *et al.* Ion migration and the role of preconditioning cycles in the stabilization of the J-V characteristics of inverted hybrid perovskite solar cells. *Adv. Energy Mater.* **6,** 1–9 (2016).

28. Van Reenen, S., Kemerink, M. & Snaith, H. J. Modeling Anomalous Hysteresis in Perovskite Solar Cells. *J. Phys. Chem. Lett.* **6,** 3808–3814 (2015).

29. Sánchez, R. S. *et al.* Slow Dynamic Processes in Lead Halide Perovskite Solar Cells . Characteristic Times and Hysteresis Slow Dynamic Processes in Lead Halide Perovskite Solar Cells . Characteristic Times and Hysteresis. *J. Phys. Chem. Lett.* **5,** 2357–2363 (2014).

30. Gonzalez-pedro, V. *et al.* General Working Principles of CH 3 NH 3 PbX 3 Perovskite Solar Cells. *Nano* (2013).

31. Guerrero, A. *et al.* Properties of Contact and Bulk Impedances in Hybrid Lead Halide Perovskite Solar Cells Including Inductive Loop Elements. *J. Phys. Chem. C* **120,** 8023–8032 (2016).

32. Almora, O. *et al.* Capacitive dark currents, hysteresis, and electrode polarization in lead halide perovskite solar cells. *J. Phys. Chem. Lett.* **6,** 1645–1652 (2015).

33. Zarazua, I., Bisquert, J. & Garcia-Belmonte, G. Light-Induced Space-Charge Accumulation Zone as Photovoltaic Mechanism in Perovskite Solar Cells. *J. Phys. Chem. Lett.* **7,** 525–528 (2016).

34. De Bastiani, M., D'Innocenzo, V., Stranks, S. D., Snaith, H. J. & Petrozza, A. Role of the crystallization substrate on the photoluminescence properties of organo-lead mixed halides perovskites. *Apl Mater.* **2,** 81509 (2014).

35. Leijtens, T. *et al.* Mapping electric field-induced switchable poling and structural degradation in hybrid lead halide perovskite thin films. *Adv. Energy Mater.* **5,** 1–11 (2015).

36. D'Innocenzo, V. *et al.* Excitons versus free charges in organo-lead tri-halide perovskites. *Nat. Commun.* **5,** 3586 (2014).

37. Tao, C. *et al.* 17.6% Stabilized Efficiency in Low-Temperature Processed Planar

Perovskite Solar Cells. *Energy Environ. Sci. Energy Environ. Sci* **8,** 2365–2370 (2015).

38. Xu, J. *et al.* Perovskite–fullerene hybrid materials suppress hysteresis in planar diodes. *Nat. Commun.* **6,** 7081 (2015).

39. Yang, T.-Y., Gregori, G., Pellet, N., Grätzel, M. & Maier, J. The Significance of Ion Conduction in a Hybrid Organic–Inorganic Lead-Iodide-Based Perovskite Photosensitizer. *Angew. Chemie* **127,** 8016–8021 (2015).

40. Giorgi, G., Fujisawa, J. I., Segawa, H. & Yamashita, K. Small photocarrier effective masses featuring ambipolar transport in methylammonium lead iodide perovskite: A density functional analysis. *J. Phys. Chem. Lett.* **4,** 4213–4216 (2013).

41. Wu, X. *et al.* Composition-dependent light-induced dipole moment change in organometal halide perovskites. *J. Phys. Chem. C* **119,** 1253–1259 (2015).

42. Pockett, A. *et al.* Characterization of planar lead halide perovskite solar cells by impedance spectroscopy, open-circuit photovoltage decay, and intensity-modulated photovoltage/photocurrent spectroscopy. *J. Phys. Chem. C* **119,** 3456–3465 (2015).

43. Da Como, E., De Angelis, F., Snaith, H. & Walker, A. *Unconventional Thin Film Photovoltaics*. (The Royal Society of Chemistry, 2016). doi:10.1039/9781782624066

44. Mizusaki, J., Arai, K. & Fueki, K. Ionic conduction of the perovskite-type halides. *Solid State Ionics* **11,** 203–211 (1983).

45. Leguy, A. M. A. *et al.* The dynamics of methylammonium ions in hybrid organic-inorganic perovskite solar cells. *Nat. Commun.* **6,** 7124 (2015).

46. Zou, H. *et al.* Polarization-induced enhancement of photoluminescence in Pr3+ doped ferroelectric diphase BaTiO3-CaTiO3 ceramics. *J. Appl. Phys.* **114,** 73103 (2013).

47. Kittel. *Principles in Solid State Physics*.

48. Petrus, M. L. *et al.* The Influence of Water Vapor on the Stability and Processing of Hybrid Perovskite Solar Cells Made from Non-Stoichiometric Precursor Mixtures. *ChemSusChem* **9,** 2699–2707 (2016).

49. Guerrero, A., Juarez-Perez, E. J., Bisquert, J., Mora-Sero, I. & Garcia-Belmonte, G. Electrical field profile and doping in planar lead halide perovskite solar cells. *Appl. Phys. Lett.* **105,** (2014).

50. Gottesman, R. *et al.* Dynamic Phenomena at Perovskite / Electron- Selective Contact Interface as Interpreted from Photovoltage Decays. *Chem* **1,** 776–789 (2016).

51. Du, M. H. Density functional calculations of native defects in CH<inf>3</inf>NH<inf>3</inf>PbI<inf>3</inf>: Effects of spin - Orbit coupling and self-interaction error. *J. Phys. Chem. Lett.* **6,** 1461–1466 (2015).

52. Mosconi, E., Meggiolaro, D., Snaith, H., Stranks, S. D. & De Angelis, F. Light-induced Annihilation of Frenkel Defects in Organo-Lead Halide Perovskites. *Energy Environ. Sci.* 1–7 (2016). doi:10.1039/C6EE01504B

53. Shao, Y. *et al.* Grain boundary dominated ion migration in polycrystalline organic–inorganic halide perovskite films. *Energy Environ. Sci.* **501,** 395–398 (2016).

54. Gratia, P. *et al.* Intrinsic Halide Segregation at Nanometer Scale Determines the High Efficiency of Mixed Cation/Mixed Halide Perovskite Solar Cells. *J. Am. Chem. Soc.* jacs.6b10049 (2016). doi:10.1021/jacs.6b10049

55. Besleaga, C. *et al.* Iodine Migration and Degradation of Perovskite Solar Cells Enhanced by Metallic Electrodes. *J. Phys. Chem. Lett.* 5168–5175 (2016). doi:10.1021/acs.jpclett.6b02375

56. Jeangros, Q. *et al.* In Situ TEM Analysis of Organic-Inorganic Metal-Halide Perovskite Solar Cells under Electrical Bias. *Nano Lett.* **16,** 7013–7018 (2016).

57. Mosconi, E. & De Angelis, F. Mobile Ions in Organohalide Perovskites: Interplay of Electronic Structure and Dynamics. *ACS Energy Lett.* acsenergylett.6b00108 (2016). doi:10.1021/acsenergylett.6b00108

58. Domanski, K. *et al.* Not All That Glitters Is Gold: Metal-Migration-Induced Degradation in Perovskite Solar Cells. *ACS Nano* **10,** 6306–6314 (2016).

59. Shao, Y., Xiao, Z., Bi, C., Yuan, Y. & Huang, J. Origin and elimination of photocurrent hysteresis by fullerene passivation in CH3NH3PbI3 planar heterojunction solar cells. *Nat. Commun.* **5,** 5784 (2014).

60. Pichler, T., Matus, M., Kürti, J. & Kuzmany, H. Phase separation in KxC60 ($0 \leq x \leq 6$) as obtained from in situ Raman spectroscopy. *Phys. Rev. B* **45,** 13841–13844 (1992).

61. Kikuchi, P. B. and M. K. and M. A. G. and F. L. P. and W. H. and P. D. and K. Raman and infrared studies of single-crystal C 60 and derivatives. *J. Phys. Condens. Matter* **5,** 2739 (1993).

62. Chen, Q. *et al.* Quantitative operando visualization of the energy band depth profile in solar cells. *Nat. Commun.* **6,** 7745 (2015).

63. Jiang, C.-S. *et al.* Carrier separation and transport in perovskite solar cells studied by nanometre-scale profiling of electrical potential. *Nat. Commun.* **6,** 8397 (2015).

64. Even, J., Pedesseau, L., Jancu, J. & Katan, C. Importance of Spin − Orbit Coupling in Hybrid Organic/Inorganic Perovskites for Photovoltaic Applications. (2013).

65. Brivio, F., Butler, K. T., Walsh, A. & van Schilfgaarde, M. Relativistic quasiparticle self-consistent electronic structure of hybrid halide perovskite photovoltaic absorbers.

Phys. Rev. B **89,** 155204 (2014).

66. Computer simulation model of the effects of interface states on high-performance amorphous silicon solar cells. *J. Appl. Phys.* **63,** 550–560 (1988).

67. Kesari, Y. & Athawale, A. Ultrasound assisted bulk synthesis of CH3NH3PbI3 perovskite at room temperature. *Mater. Lett.* **159,** 87–89 (2015).

68. Yakunin, S. *et al.* Detection of X-ray photons by solution-processed lead halide perovskites. *Nat. Photonics* **9,** 444-U44 (2015).

69. Lin, Q., Armin, A., Burn, P. L. & Meredith, P. Filterless narrowband visible photodetectors. *Nat. Photonics* **9,** 687–694 (2015).

70. Náfrádi, B. *et al.* Optically switched magnetism in photovoltaic perovskite CH3NH3(Mn:Pb)I3. *Nat. Commun.* **7,** 13406 (2016).

71. Dong, R. *et al.* High-Gain and Low-Driving-Voltage Photodetectors Based on Organolead Triiodide Perovskites. *Adv. Mater.* **27,** 1912–1918 (2015).

72. Fang, Y. & Huang, J. Resolving weak light of sub-picowatt per square centimeter by hybrid perovskite photodetectors enabled by noise reduction. *Adv. Mater.* **27,** 2804–2810 (2015).

73. Ramasamy, P. *et al.* All-inorganic cesium lead halide perovskite nanocrystals for photodetector applications. *Chem. Commun.* **52,** 2067–2070 (2016).

74. Baumann, A. *et al.* Identification of Trap States in Perovskite Solar Cells. *J. Phys. Chem. Lett.* **6,** 2350–2354 (2015).

75. Lee, Y. *et al.* High-performance perovskite-graphene hybrid photodetector. *Adv. Mater.* **27,** 41–46 (2015).

76. Jones, E. W. *et al.* A novel dimethylformamide (DMF) free bar-cast method to deposit organolead perovskite thin films with improved stability. *Chem. Commun.* **52,** 4301–4304 (2016).

77. Sutherland, B. R. *et al.* Sensitive, Fast, and Stable Perovskite Photodetectors Exploiting Interface Engineering. *ACS Photonics* **2,** 1117–1123 (2015).

78. Xing, G. *et al.* Long-Range Balanced Electron- and Hole-Transport Lengths in Organic-Inorganic CH3NH3PbI3. **6960,** 498–500 (2013).

79. Stranks, S. D. *et al.* Electron-Hole Diffusion Lengths Exceeding. *Science* **342,** 341–344 (2014).

80. Dou, L. *et al.* Solution-processed hybrid perovskite photodetectors with high detectivity. *Nat. Commun.* **5,** 5404 (2014).

81. Gottesman, R. *et al.* Extremely Slow Photoconductivity Response of CH 3 NH 3 PbI 3 Perovskites Suggesting Structural Changes under Working Conditions. *J. Phys. Chem. Lett.* **5,** 140722203534006 (2014).

82. Fang, Y., Dong, Q., Shao, Y., Yuan, Y. & Huang, J. Highly narrowband perovskite single-crystal photodetectors enabled by surface-charge recombination. *Nat. Photonics* **9,** 679–686 (2015).

83. Lin, Q., Armin, A., Lyons, D. M., Burn, P. L. & Meredith, P. Low noise, IR-blind organohalide perovskite photodiodes for visible light detection and imaging. *Adv. Mater.* **27,** 2060–2064 (2015).

84. Lezzi, F., Ferrari, G., Pennetta, C. & Pisignano, D. Suppression of Low-Frequency Electronic Noise in Polymer Nanowire Field-Effect Transistors. *Nano Lett.* **15,** 7245–7252 (2015).

85. Saidaminov, M. I. *et al.* Planar-integrated single-crystalline perovskite photodetectors. *Nat Commun* **6,** 8724 (2015).

86. Saidaminov, M. I. *et al.* Perovskite Photodetectors Operating in Both Narrowband and Broadband Regimes. *Adv. Mater.* 8144–8149 (2016). doi:10.1002/adma.201601235

87. Bhooshan Kumar, V., Gouda, L., Porat, Z. & Gedanken, A. Sonochemical synthesis of CH3NH3PbI3 perovskite ultrafine nanocrystal sensitizers for solar energy applications. *Ultrason. Sonochem.* **32,** 54–59 (2016).

88. Zhang, Y. *et al.* A highly photoconductive composite prepared by incorporating polyoxometalate into perovskite for photodetection application. *Chem. Commun.* **52,** 1–6 (2016).

89. Sun, Z., Aigouy, L. & Chen, Z. Plasmonic-enhanced perovskite–graphene hybrid photodetectors. *Nanoscale* **8,** 7377–7383 (2016).

90. Chen, S. *et al.* A Flexible UV Vis NIR Photodetector based on a Perovskite/Conjugated-Polymer Composite. *Adv. Mater.* 5969–5974 (2016). doi:10.1002/adma.201600468

91. Murali, B. *et al.* Halide Perovskites for Photodetector Applications †. *J. Mater. Chem. C* **4,** 2545–2552 (2016).

92. Donati, S. *Photodetectors:Devices, Circuits and Applications: Devices, Circuits, and Applications*.

93. Schulz, P. *et al.* Interface energetics in organo-metal halide perovskite-based photovoltaic cells. *Energy Environ. Sci.* **7,** 1377–1381 (2014).

94. van der Ziel, A. Unified Presentation of 1/F Noise in Electron Devices: Fundamental 1/F Noise Sources. *Proc. IEEE* **76,** 233–258 (1988).

95. Lundberg, K. Noise sources in bulk CMOS. *Unpubl. Pap.* 1–12 (2002). doi:10.1.1.151.7933

96. Acik, M. & Darling, S. B. Graphene in perovskite solar cells: device design, characterization and implementation. *J. Mater. Chem. A* **4,** 6185–6235 (2016).

97. Agresti, A. *et al.* Efficiency and Stability Enhancement in Perovskite Solar Cells by Inserting Lithium-Neutralized Graphene Oxide as Electron Transporting Layer. *Adv. Funct. Mater.* 2686–2694 (2016). doi:10.1002/adfm.201504949

98. Kim, Y. G. *et al.* Atomically thin two-dimensional materials as hole extraction layers in organolead halide perovskite photovoltaic cells. *J. Power Sources* **319,** 1–8 (2016).

99. Schulz, P. *et al.* High-work-function molybdenum oxide hole extraction contacts in hybrid organic-inorganic perovskite solar cells. *ACS Appl. Mater. Interfaces* **8,** 31491–31499 (2016).

100. Wang, F. *et al.* Phenylalkylamine Passivation of Organolead Halide Perovskites Enabling High-Efficiency and Air-Stable Photovoltaic Cells. *Adv. Mater.* **28,** 9986–9992 (2016).

101. Hadadian, M. *et al.* Enhancing Efficiency of Perovskite Solar Cells via N-doped Graphene: Crystal Modification and Surface Passivation. *Adv. Mater.* **28,** 8681–8686 (2016).

102. Stewart, R. J., Grieco, C., Larsen, A. V., Maier, J. J. & Asbury, J. B. Approaching Bulk Carrier Dynamics in Organo-Halide Perovskite Nanocrystalline Films by Surface Passivation. *J. Phys. Chem. Lett.* **7,** 1148–1153 (2016).

103. Tripathi, N., Shirai, Y., Yanagida, M., Karen, A. & Miyano, K. Novel Surface Passivation Technique for Low-Temperature Solution-Processed Perovskite PV Cells.

ACS Appl. Mater. Interfaces **8,** 4644–4650 (2016).

104. Lin, Y. *et al.* π-Conjugated Lewis Base: Efficient Trap-Passivation and Charge-Extraction for Hybrid Perovskite Solar Cells. *Adv. Mater.* 1604545 (2016). doi:10.1002/adma.201604545

105. Lee, Y. H. *et al.* Enhanced Charge Collection with Passivation Layers in Perovskite Solar Cells. *Adv. Mater.* **28,** 3966–3972 (2016).

106. Palazon, F. *et al.* Polymer-Free Films of Inorganic Halide Perovskite Nanocrystals as UV-to-White Color-Conversion Layers in LEDs. *Chem. Mater.* **28,** 2902–2906 (2016).

107. Zhao, T., Chueh, C.-C., Chen, Q., Rajagopal, A. & Jen, A. K.-Y. Defect Passivation of Organic-Inorganic Hybrid Perovskites by Diammonium Iodide towards High-Performance Photovoltaic Devices. *ACS Energy Lett.* **1,** 757–763 (2016).

108. Kollek, T. *et al.* Thiophene Functionalized Hybrid Perovskite Micro-Rods and their Application in Photodetector Devices for Investigating Charge Transport Through Interfaces in Particle-Based Materials. *ACS Appl. Mater. Interfaces* acsami.6b12466 (2016). doi:10.1021/acsami.6b12466

109. Zhang, W. *et al.* Ultrasmooth organic–inorganic perovskite thin-film formation and crystallization for efficient planar heterojunction solar cells. *Nat. Commun.* **6,** 6142 (2015).